HIGH-LEVEL QUANTUM CHEMICAL STUDIES OF SMALL METAL-CONTAINING MOLECULAR SYSTEMS

by

ZHI SUN

(Under the Direction of Henry F. Schaefer III)

ABSTRACT

This dissertation presents the applications of high-level quantum chemistry methods to several small molecular systems containing metal elements. These research projects mainly focus on the prediction and characterization of novel alkaline-earth metallacyclopentadienes, reaction mechanism and potential energy surface of Al + CO_2 reaction, characterization of alkali-metal trihalides MX_3 with heavy halogen (Cl, Br, and I) elements, and vibrational spectra of alkali-metal trifluorides MF_3. Highly accurate coupled cluster and multireference methods have been employed throughout this research. Those accurate results allow us to make useful comparison between experiment and theory, and any identified inconsistencies have been heavily discussed. As a result, new motivations have been provided for future research in relevant fields.

INDEX WORDS: Alkaline-Earth Metallacyclopentadiene, Aluminum Carbon Dioxide Complex, Alkali-Metal Trihalides, Density Functional Theory, Multi-Reference Method, Coupled-Cluster Theory

HIGH-LEVEL QUANTUM CHEMICAL STUDIES OF SMALL METAL-CONTAINING MOLECULAR SYSTEMS

by

ZHI SUN

Ph.D. Beijing University of Technology, China, 2015

A Dissertation Submitted to the Graduate Faculty of The University of Georgia in Partial Fulfillment of the Requirements for the Degree

DOCTOR OF PHILOSOPHY

ATHENS, GEORGIA

2018

HIGH-LEVEL QUANTUM CHEMICAL STUDIES OF SMALL METAL-CONTAINING MOLECULAR SYSTEMS

by

ZHI SUN

Major Professor: Henry F. Schaefer III
Committee: Tina T. Salguero
Gary E. Douberly
Steven E. Wheeler

Electronic Version Approved:

Suzanne Barbour
Dean of the Graduate School
The University of Georgia
December 2018

ACKNOWLEDGEMENTS

Coming to the United States for a PhD degree is probably the craziest thing I have ever done, and it was like a dream or even a “mission impossible” to me. I never regret it because it is also one of the most important and correct decisions I have made in my life, and I did it. I would like to thank many wonderful people here because my dream won’t come true without the love and support from them.

My parents have sacrificed a lot for bringing me up and supporting all my big decisions including coming to the US. I just realized that I have been away from home for almost four years, without going home even once. Thank you, mom and dad, for supporting me without conditions, for looking after me for so many years, for always believing in me and giving me the courage, and for your love. Love you forever.

To Jing, my dear wife, you are the best thing that I’ve ever found. Thank you for encouraging me to apply US graduation school, for being so supportive and understanding, for choosing to stay with me after graduation, and for loving me. My life becomes so wonderful with your company! Will always love you!

I would like to thank my advisor Prof. Schaefer, the man who changed my life. I am honored to be in your research team, and I feel so lucky to have the opportunity of doing research in your lab, CCQC. Thank you for having me here and your kind support. I would also like to thank Dr. Xie, who taught me a lot, gave me advices, and offered me so many food. My life becomes much easier with your help.

To my collaborators, Prof. Roald Hoffmann, Prof. Kirk Peterson, Prof. Grant Hill, Dr. Kevin Moore, Dr. Andrew Launder, Dr. Kevin Murphy, and James Morgan, thanks a lot for providing wonderful suggestions and help during our research. I also want to thank my friends Dr. Wang Xiao, Dr. Chenyang Li, and Dr. Yudong Qiu, and all other CCQC members. I learnt a lot from you guys and had a wonderful time in CCQC! To Prof. Salguero, Prof. Douberly, and Prof. Wheeler, thanks a lot for being my advisory committees. Finally, special thanks to my advisors when I was in Beijing University of Technology, Prof. Yongdong Liu and Prof. Rugang Zhong, for leading me to the world of quantum chemistry.

TABLE OF CONTENTS

CHAPTER 1

Introduction and Literature Review

1.1 Introduction

Over the past few decades, the rapidly expanding role of quantum chemistry have made it a powerful tool in all branches of chemistry. The development of electronic structure theory enables quantum chemistry to handle various chemical problems using rigorous quantum-mechanical treatment, with high level of accuracy and reasonable computational cost. In this chapter, the electronic structure theory involved in present study will be briefly reviewed. These will mainly include Hartree-Fock (HF) theory, configurational interaction theory, coupled-cluster theory, multireference methods, density functional theory (DFT), and vibrational second-order perturbation theory (VPT2). These will be followed by a prospectus introducing the main content and structure of this dissertation.

1.2 *Ab Initio* Methods

1.2.1 Hartree-Fock (HF) Method

The main task of theoretical quantum chemistry is to solve the Schrödinger equation (1.1), where the $\hat{H}$ is the Hamiltonian operator for the molecular system, and Ψ is the wavefunction of the system. Here we focus on solving non-relativistic, time-independent Schrödinger equation.[1]

$$\hat{H}\Psi = E\Psi \tag{1.1}$$

The molecular Hamiltonian in atomic unit can be simply expressed as the equation 1.2. Those terms in equation 1.2 correspond to nuclear kinetic energy, electron kinetic energy, nucleus-electron attraction, nucleus-nucleus repulsion, and electron-electron repulsion, respectively. In shorthand, equation 1.2 can be rewritten as 1.3.

$$\hat{H} = -\frac{1}{2}\sum_{A}^{nuc}\frac{1}{M_A}\nabla_A^2 - \frac{1}{2}\sum_{i}^{elec}\nabla_i^2 - \sum_{A}^{nuc}\sum_{i}^{elec}\frac{Z_A}{r_{Ai}} + \sum_{A>B}^{nuc}\frac{Z_A Z_B}{R_{AB}} + \sum_{i>j}^{elec}\frac{1}{r_{ij}} \tag{1.2}$$

$$\hat{H} = \hat{T}_N + \hat{T}_e + V_{Ne} + V_{NN} + V_{ee} \tag{1.3}$$

To further simplify the Hamiltonian expression (1.3), we introduce the first important approximation, Born-Oppenheimer (B-O) approximation.[2] The B-O approximation assumes that nuclei are frozen compared to electrons, based on two facts: (a) the nuclei are much heavier than electrons (~2,000:1 or more) and (b) the electron motions are much faster than nuclear motions. With this approximation, the nuclear kinetic energy ($\hat{T}_N$ term in equation 1.3) can be ignored, and the nucleus-nucleus repulsion (V_{NN} term) can be treated as a constant. We can rewrite the equation 1.3 as the equation 1.4 which is usually called the electronic Hamiltonian, $\hat{H}_e$:

$$\hat{H}_e = \hat{T}_e + V_{Ne} + V_{ee} + V_{NN} \tag{1.4}$$

Such separation of electron and nucleus results in the electronic Schrödinger equation (1.5, with the r and R being the coordinates of electron and nucleus, respectively) which we solve for the electronic energy and electronic wavefunction. Note that, traditionally, the constant term V_{NN} stays in the electronic Hamiltonian $\hat{H}_e$, and it will only shift the eigenvalues of the same eigenfunctions by a constant. Moreover, the electronic energy $E_e(R)$ now only depends on nuclear coordinates *R* as fixed parameters, which means that potential energy surface (PES) could be obtained if the electronic Schrödinger equations can be solved with numerous sets of nuclear coordinates. This is also a direct result of B-O approximation.

$$\hat{H}_e(r;R)\Psi_e(r;R) = E_e(R)\Psi_e(r;R) \tag{1.5}$$

The first successful way to solve electronic Schrödinger equation was proposed and developed by Hartree, Fock, and Slater.[3, 4] In Hartree-Fock method, the electronic wavefunction is represented by a Slater determinant (see generic equation 1.6) which enforces an antisymmetric *N*-electron wavefunction.

$$\Psi_{HF} = \frac{1}{\sqrt{N!}}\begin{vmatrix} \phi_1(1) & \phi_2(1) & \cdots & \phi_N(1) \\ \phi_1(2) & \phi_2(2) & \cdots & \phi_N(2) \\ \vdots & \vdots & \ddots & \vdots \\ \phi_1(N) & \phi_2(N) & \cdots & \phi_N(N) \end{vmatrix} \tag{1.6}$$

The ϕ in Slater determinant is the spin orbital in spatial (three) and spin (one) coordinates of electrons. The spatial orbitals (that is, the molecular orbital, MO) are expanded as

linear combination of atomic orbitals (AO) which are often represented by contracted Gaussian-type functions (basis sets) to mimic Slater type orbitals. This is known as the LCAO methods, as expressed in equation 1.7.

$$\phi_i = \sum_{\mu} C_{\mu}^{i} \chi_{\mu} \tag{1.7}$$

With the Slater determinant representing the *N*-electron wavefunction, the Hartree-Fock molecular electronic energy is expressed as equation 1.8, with the energy always greater than or equal to the exact (true) energy. In details, the electronic Hamiltonian is the sum (equation 1.9) of one-electron operators ($\hat{f}$) and two-electron operators ($\hat{g}$).

$$E_e(R)_{HF} = \left\langle \Psi_e(r;R) \middle| \hat{H}_e \middle| \Psi_e(r;R) \right\rangle \geq E_{exact} \tag{1.8}$$

$$\hat{H}_e = \sum_i \hat{f}_i + \sum_{i<j} \hat{g}_{ij} \tag{1.9}$$

The Hartree-Fock energy can then be written as equations 1.10, with the last two terms being Coulomb and exchange integrals, respectively. The variational theorem allows us to minimize the Hartree-Fock energy via varying the spin orbitals in Slater determinant, and the resulting optimized orbitals are eigenfunctions of the Fock operator ($\hat{F}$) with the eigenvalues being orbitals energies (ε_i), as shown in equation 1.11.

$$E_{HF} = \langle \Psi_e | \sum_i \hat{f}_i + \sum_{i<j} \hat{g}_{ij} | \Psi_e \rangle$$
$$= \sum_i \langle \phi_i | \hat{f}_i | \phi_i \rangle + \sum_{i<j} \left(\langle \phi_i \phi_j | \hat{g}_{ij} | \phi_i \phi_j \rangle - \langle \phi_i \phi_j | \hat{g}_{ij} | \phi_j \phi_i \rangle \right) \quad (1.10)$$

$$\hat{F} \phi_i = \varepsilon_i \phi_i \quad (1.11)$$

With Roothaan's proposal to expand the spatial orbitals as linear combination of a set of basis functions, the resulting Hartree-Fock-Roothaan equations from equation 1.11 need to be solved via an iterative procedure. The iteration continues until no further improvement in MO coefficients and energies can be achieved. Because of its self-consistency, the Hartree-Fock method is often referred to as self-consistent filed (SCF) method.[5, 6]

1.2.2 Post-Hartree-Fock Method

The Hartree-Fock method usually recovers almost 99% of the total energies. However, lots of important chemistry happen in the remaining 1%. In fact, the Hartree-Fock method is just an approximation based on two assumptions: (a) only one determinant is needed for constructing the wavefunction and (b) each electron interacts with average charge distribution caused by other electrons. Therefore, the Hartree-Fock method is considered "uncorrelated". These assumptions introduce errors in wavefunction and energy, and the energy error is called total correlation energy, which is the difference between the true energy and the Hartree-Fock energy (equation 1.12) with a complete basis.

$$E_{corr} = E_{exact} - E_{HF} \tag{1.12}$$

The Post-Hartree-Fock methods were developed to account for electron correlations. The popular ones include Möller-Plesset (MP) perturbation theory, configuration interaction (CI), and coupled cluster (CC) theory. For the perturbation theory,[7] the exact Hamiltonian (equation 1.13) is divided into a zeroth-order Hamiltonian ($\hat{H}_0$) and a perturbation (fluctuation potential, $\hat{H}'$). The solution is expressed as a Taylor series in perturbation strength (λ).

$$\hat{H} = \hat{H}_0 - \lambda \hat{H}' \tag{1.13}$$

Its energy is expressed as the sum of the unperturbed energy and a given-order correction from perturbation. The perturbation theory is often taken through second order, known as the second-order Möller-Plesset perturbation theory (that is, MP2). The perturbation theory is relatively cheap, but usually less accurate than the CI and CC methods.

As reviewed above, the Hartree-Fock method takes only one determinant to represent the wavefunction which, in many cases, is not a decent approximation. It takes an infinite number of determinants to cover all possible electron configurations which make contributions to the exact wavefunction. The CI and CC methods are developed under this consideration.

For the CI method,[8] the wavefunction is expressed as a linear combination of Slater determinants (equation 1.14), with the expansion coefficients (C_i) evaluated variationally.

$$\left|\Psi\right\rangle = \sum_i C_i \left|\Psi_i\right\rangle \tag{1.14}$$

Theoretically, the arrangement of all electrons in all possible ways (with right symmetries) for a finite orbital basis set will cover all electronic configurations contributing to the total wavefunction, which is ideal but extremely costly. This is known as Full CI which is impractical for most molecular systems. However, a decent approximation can often be done by a truncation of the CI expansion (equation 1.15) according to excitation level. With the $\left|\Phi_0\right\rangle$ being the Hartree-Fock reference determinant (leading term), the importance of the following configurations drops off rapidly. The expansion truncation is usually done at a given excitation level. For instance, the truncations at the double and triple excitation levels give CISD and CISDT, respectively.

$$\left|\Psi\right\rangle = c_0 \left|\Phi_0\right\rangle + \sum c_i^a \left|\Phi_i^a\right\rangle + \sum c_{ij}^{ab} \left|\Phi_{ij}^{ab}\right\rangle + \sum c_{ijk}^{abc} \left|\Phi_{ijk}^{abc}\right\rangle + \cdots \tag{1.15}$$

Different from CI, the CC method[9] define the ground state wavefunction by exponential ansatz (equation 1.16), with $\hat{T}$ as the excitation operator (equations 1.17 – 1.19) which is expressed as a sum of operators that generate singly-excited, doubly-excited, triple-excited, and higher-order excited determinants. With a complete $\hat{T}$, the CC wavefunction will be equivalent to Full CI wavefunction, however, a truncated $\hat{T}$ will be

needed to perform practical computations. For instance, the popular CCSD (coupled cluster with single and double excitations) method truncates the expansion at $\hat{T} = \hat{T}_1 + \hat{T}_2$.

$$\left|\Psi_{CC}\right\rangle = e^{\hat{T}}\left|\Phi_0\right\rangle = \left(1 + \hat{T} + \frac{\hat{T}^2}{2!} + \frac{\hat{T}^3}{3!} + \cdots\right)\left|\Phi_0\right\rangle \tag{1.16}$$

$$\hat{T} = \hat{T}_1 + \hat{T}_2 + \hat{T}_3 + \cdots \tag{1.17}$$

$$\hat{T}_1\left|\Phi_0\right\rangle = \sum_i \sum_a t_i^a \left|\Phi_i^a\right\rangle \tag{1.18}$$

$$\hat{T}_2\left|\Phi_0\right\rangle = \sum_{i<j} \sum_{a<b} t_{ij}^{ab} \left|\Phi_{ij}^{ab}\right\rangle \tag{1.19}$$

The CC energy can be easily obtained from equation 1.20 to 1.25. The $\bar{H}$ is the similarity transformed Hamiltonian which may be expanded by applying Baker-Campbell-Hausdorff (BCH) formula.

$$\hat{H}\left|\Psi_{cc}\right\rangle = E\left|\Psi_{cc}\right\rangle \tag{1.20}$$

$$\hat{H}e^{\hat{T}}\left|\Psi_{HF}\right\rangle = Ee^{\hat{T}}\left|\Psi_{HF}\right\rangle \tag{1.21}$$

$$e^{-\hat{T}}\hat{H}e^{\hat{T}}\left|\Psi_{HF}\right\rangle = Ee^{-\hat{T}}e^{\hat{T}}\left|\Psi_{HF}\right\rangle \tag{1.22}$$

$$e^{-\hat{T}}\hat{H}e^{\hat{T}}\left|\Psi_{HF}\right\rangle = E\left|\Psi_{HF}\right\rangle \tag{1.23}$$

$$\bar{H}\left|\Psi_{HF}\right\rangle = E\left|\Psi_{HF}\right\rangle \tag{1.24}$$

$$\left\langle\Psi_{HF}\right|\bar{H}\left|\Psi_{HF}\right\rangle = E \tag{1.25}$$

Note that, in above CC energy expression (equation 1.25), only single and double excitation terms survive due to Slater rule. However, the single and double cluster amplitudes t_i^a and t_{ij}^{ab} necessary to obtain the CC energy will need to be determined first using equation 1.26 which involves excited wavefunction. The amplitudes t_i^a and t_{ij}^{ab} will be indirectly affected by higher-order terms like $\hat{T}_2^2$ which will approximately account for quadruple excitations.

$$\left\langle \Psi_{ij\cdots}^{ab\cdots} \middle| \bar{H} \middle| \Psi_{HF} \right\rangle = 0 \tag{1.26}$$

Therefore, the inclusion of such products of lower-order terms makes coupled-cluster methods size extensive and accurate.

The most well-known coupled cluster method would be the CCSD(T) method,[10-13] the widely-accepted "gold standard" method in quantum chemistry. In fact, the coupled cluster theory is related to many-body perturbation theory (MBPT). A CCSD energy expression involves all necessary terms for up to the third order energy. However, the fourth order energy is only attainable by inclusion of triple excitation contributions. The resulting method by doing so is called CCSD[T]. Moreover, if an additional fifth-order energy from involving both single and triple terms is added, the popular CCSD(T) method is achieved.

1.3 Multireference Methods

For strongly correlated systems for which single Slater determinant is not adequate to describe the electronic structure, multireference method will be needed. The multiconfigurational self-consistent-field (MCSCF) method is a general approach for treating these molecular systems, such as bond breaking processes, diradicals, and complexes with transition metals, etc.

In MCSCF method, the wavefunction is expressed as the CI form (equation 1.27) as a linear combination of multiple Slater determinants (also called configurational state functions, CSF's). The c_i and Ψ_i are CI coefficients and individual Slater determinants (or individual CSF), respectively. The corresponding energy expression is shown as equation 1.28, with the H_{ij} being the matrix elements of electronic Hamiltonian between two different determinants.

$$\Psi_{MCSCF} = \sum_i c_i \Psi_i \tag{1.27}$$

$$E = \sum_{ij} c_i^* c_j H_{ij} \tag{1.28}$$

The CI coefficients c_i are evaluated variationally. However, unlike the regular Hartree-Fock method which obtains its orbitals by minimizing the energy of the single Slater determinant, in the MCSCF method, the orbitals are variationally obtained by minimizing the CI energy of the MCSCF wavefunction including multiple Slater determinants. The MCSCF energy is differentiated with respect to orbital rotations.

Note that, if the individual Slater determinants Ψ_i to be included are selected manually, it is a general MCSCF wavefunction. For instance, if only two Slater determinants are selected, we call it two-configuration self-consistent-field (TCSCF). A different approach to construct the MCSCF wavefunction is done by selecting an "active space" which includes a set of virtual and occupied orbitals. All possible determinants in the range of the "active space" will be automatically selected by computing program, to construct the MCSCF wavefunction. This is the popular complete-active-space self-consistent-field (CASSCF) method.[14] However, with large active spaces, such automatic selection of all possible determinants could easily lead to an unmanageable wavefunction with a huge number of determinants. Therefore, an intermediate solution is the restricted-active-space self-consistent-field (RASSCF)[15] by splitting orbitals into three groups (RAS I, RAS II, and RAS III). Restrictions are made to allow the maximum number of holes and particles for each group. Only independent pairs of orbitals in different groups contribute to the energy change, which could simplify the computations.

A limitation of the MCSCF methods is no dynamic correlation, which can be improved by working together with perturbation theory, configurational interaction or coupled cluster methods. Here we only introduce the MCSCF + CI (multireference configuration interaction, MRCI)[16, 17] method here because it was employed in present study. The excited configuration state functions (CSFs) for MRCI can be generated from a set of selected configurations based on the MCSCF wavefunction. However, the CSFs obtained in this way can run easily into millions and even billions. To solve this problem, we can choose to apply excitation operators to the MCSCF wavefunction as a whole, instead of applying those operators to the set of configurations selected from the

reference state (MCSCF wavefunction). As a result, the number of the internally contracted states will be more-or-less independent of the number of CSFs of the reference space (MCSCF wavefunction), and much fewer coefficients to be optimized. This strategy is called internal contraction. Currently, the most popular internally contracted MRCI method is MRCISD which only contains the single and double excitations.

1.4 Density Functional Theory

The Hohenberg-Kohn theorems[18] build the modern DFT's foundation: (1) The ground state properties of a many-electron system depend only on the electronic density ρ(x,y,z) and (2) The correct ground state density for a system is the one that minimizes the total energy through the functional E[ρ(x,y,z)]. Together with the B-O approximation, we can write the electronic energy as a functional of the electron density (equation 1.29). Those terms at right is the kinetic energy of electrons, electron-nuclear attraction energy, classical electron repulsion energy, and non-classical electron interaction energy, respectively.

$$E(\rho) = T(\rho) + V_{eN}(\rho) + J(\rho) + V_{non-classic}(\rho) \tag{1.29}$$

Unfortunately, the exact forms of $T(\rho)$ and $V_{non-classic}(\rho)$ in this expression are not known. By reintroducing orbitals, Kohn and Sham (KS)[19] suggested that a single Slater determinant representing a non-interacting electrons that has the same electron density (ρ) as the exact wavefunction should be an accurate approximation. Accordingly, the $T(\rho)$ term can be divided into two terms, $T_s(\rho)$ and $T_c(\rho)$, kinetic energy of non-

interacting electrons and correction (due to interaction of electrons) to the kinetic energy, respectively. The equation 1.29 can be rewritten as the following (1.30):

$$\begin{aligned} E(\rho) &= T_s(\rho) + T_c(\rho) + V_{eN}(\rho) + J(\rho) + V_{non-classic}(\rho) \\ &= T_s(\rho) + V_{eN}(\rho) + J(\rho) + T_c(\rho) + V_{non-classic}(\rho) \end{aligned} \tag{1.30}$$

The exact form of the $T_c(\rho)$ and $V_{non-classic}(\rho)$ are unknown. These two terms together are called exchange-correlation potential, $V_{xc}(\rho)$, which is usually expressed as the sum of exchange $V_x(\rho)$ and correlation $V_c(\rho)$ functional. This is the famous KS-DFT method. Like the Hartree-Fock method, KS-DFT energy can be evaluated variationally.

The main task of KS-DFT is to develop accurate approximation for $E_x(\rho)$ and $E_c(\rho)$. The simplest representation for the exchange-correlation functional would be the local density approximation (LDA). It defines that $V_{xc}(\rho)$ only depends on (local) density at a given point, which is not considered as a good approximation because the density distribution is not the same everywhere. As a big improvement, density gradient $\nabla\rho$ was later introduced in $V_{xc}(\rho,\nabla\rho)$ to account for the inhomogeneous density distribution, known as the generalized gradient approximation (GGA) functional. To capture second derivative information, the exchange-correlation functional can be further improved by including Laplacian of the density or kinetic energy density, which is known as the meta-generalized gradient approximations (meta-GGA). Unfortunately, those developed functionals still have limitations to treat self-interaction error, dispersion, and strongly-correlated systems. The hybrid-GGA was then proposed and developed by

mixing only a global fraction of exact exchange (Hartree-Fock) with the exchange-correlation functional to minimize self-interaction error. The dispersion-corrected functionals, DFT-D, were also developed to account for long-range dynamic correlation, such as Grimme's DFT-D dispersion tails.

1.5 Vibrational Second-Order Perturbation Theory (VPT2)

Part of this research involves the computation of harmonic and anharmonic frequencies of the molecular systems for characterization and comparison with experimental fundamentals. Therefore, it is necessary to briefly review the computational methods for vibrational frequencies here.

The vibrational potential (V) is generally expressed as a power series expansion in terms of normal coordinates (Q), as shown in equation 1.31.

$$V(Q) = V_0 + \frac{1}{2}\sum_{ij} F_{ij} Q_i Q_j + \frac{1}{6}\sum_{ijk} F_{ijk} Q_i Q_j Q_k + \frac{1}{24}\sum_{ijkl} F_{ijkl} Q_i Q_j Q_k Q_l + \cdots \qquad (1.31)$$

The V_0 is the potential energy at the equilibrium geometry. The F_{ij}, F_{ijk}, and F_{ijkl} correspond to the quadratic, cubic, and quartic force constants, respectively. A commonly used approximation is to truncate the expansion in equation 1.31 at the second term with quadratic force constant, and the harmonic frequencies can be simply obtained via diagonalizing the mass-weighted Hessian matrix F_{ij}. This is usually good enough for charactering the molecular systems (for instance, minimum, transition state, or higher-order saddle point). However, anharmonicity needs to be considered to effectively compare with experimental fundamentals.

In present study, the anharmonic frequencies are computed via the vibrational second-order perturbation theory (VPT2)[20] which is a commonly used computational method with a good balance between accuracy and computational cost. In VPT2, the anharmonic frequencies (ν_i) of asymmetric top molecules are obtained by adding a correction to harmonic frequencies (ω_i), as expressed from equations 1.32 to 1.34.

$$\nu_i = \omega_i + 2\chi_{ii} + \frac{1}{2}\sum_{i \neq j} \chi_{ij} \tag{1.32}$$

$$\chi_{ii} = \frac{1}{16}\phi_{iiii} - \frac{1}{16}\sum_{j} \frac{\phi_{iij}^2(8\omega_i^2 - 3\omega_j^2)}{\omega_j(4\omega_i^2 - \omega_j^2)} \tag{1.33}$$

$$\begin{aligned}\chi_{ij} = {} & \frac{1}{4}\phi_{iijj} - \frac{1}{4}\sum_{k} \frac{\phi_{iik}\phi_{kjj}}{\omega_k} - \frac{1}{2}\sum_{k} \frac{\phi_{ijk}^2 \omega_k(\omega_k^2 - \omega_i^2 - \omega_j^2)}{[(\omega_i + \omega_j)^2 - \omega_k^2)][(\omega_i - \omega_j)^2 - \omega_k^2)]} \\ & + \left[A_e(\zeta_{i,j}^{(a)})^2 + B_e(\zeta_{i,j}^{(b)})^2 + C_e(\zeta_{i,j}^{(c)})^2 \right]\left(\frac{\omega_i}{\omega_j} + \frac{\omega_j}{\omega_i} \right)\end{aligned} \tag{1.34}$$

The χ_{ii} and χ_{ij} are diagonal and off-diagonal anharmonic force constants, respectively. The A_e, B_e, and C_e are rotational constants, and $\zeta^{(a)}$, $\zeta^{(b)}$, and $\zeta^{(c)}$ are Coriolis constant. Those corrections involved in above equations introduce the Coriolis and centrifugal distortion.

1.6 Prospectus

This dissertation presents the applications of high-level quantum chemistry methods to several small molecular systems containing metal elements. Highly accurate coupled cluster and multireference methods have been employed throughout this research.

In Chapter 2, the prediction and characterization of alkaline-earth metallacyclopentadienes are discussed. We report systematic theoretical studies of MC_4H_4 (M = Be, Mg, Ca, Sr, Ba) rings and experimentally relevant complexes. Benchmarking against CCSD(T) and experimental results is done to evaluate the performance of the density functionals in predicting the equilibrium geometries, thermochemistry, and vibrational spectra of these species. Aromaticity of the compounds in question is quantitatively determined via NICS indices and extra cyclic resonance energies. Their viability is explained via ring strain, electron densities, natural bond orders, and orbital analyses.

In Chapter 3, reaction mechanism and potential energy surface of the Al + CO_2 reaction are discussed. The direct motivation of this study comes from a recent crossed-beam experimental studies of the Al + CO_2 → AlO + CO reaction by Honma and Hirata who have directly challenged the results of earlier theoretical studies. We report high level theoretical studies of this system. The comparison between their experiment and our new theoretical results are made. Agreement and disagreement between theory and experiment are discussed, and new explanations are provided, for a better understanding of the system.

In Chapter 4, the alkali metal trihalides MX_3 (M = Li, Na, K, Rb, and Cs; X = Cl, Br, and I) are systematically studied using density functional theory and coupled-cluster

methods. Our results suggest that the MX_3 system may be alternatively described as an $MX\text{-}X_2$ complex, rather than the $M^+X_3^-$ ion pair proposed by previous experimental studies. This new conclusion is supported by the structure of global minimum for all MX_3 species, the localized and mutually-perturbed X-X and M-X stretches in normal modes of the MX_3 molecules vibrations, bonding analyses, and thermochemistry of different fragmentation schemes.

In Chapter 5, we systematically study the MF_3 systems using both coupled-cluster and multireference methods. New predictions and explanations are provided for some known experimental and theoretical challenges, including identification of the true MF_3 minima and global minima, the unclear existence of light alkali metal trifluorides MF_3 (M = Li and Na), and assignment of the F-F-F symmetric stretch frequencies for the heavier alkali metal trifluorides MF_3 (M = K, Rb, and Cs). Significant differences between the coupled-cluster and multireference results were found in predicting the F-F-F symmetric stretch frequencies (ν_s) of the C_{2v} MF_3 (M = K, Rb, and Cs) structures.

CHAPTER 2

Alkaline-Earth Metallacyclopentadienes*

*Sun, Z., Launder, A. M., and Schaefer, H. F., *ChemistrySelect* 2017, 2, 1442. Reprinted here with permission of the publisher.

2.1 Abstract

Alkaline-earth metallacyclopentadienes are an active area of research in synthetic chemistry, notable for their roles as precursors of key cyclopentadiene derivatives. However, experimental characterization is limited due to their challenging synthesis and subsequent isolation. Herein, we report systematic theoretical studies of MC_4H_4 (M = Be, Mg, Ca, Sr, Ba) rings and experimentally relevant complexes. Benchmarking against CCSD(T) and experiment shows reasonable performance for the B3LYP, BP86, and M06-2X density functionals in predicting the equilibrium geometries, thermochemistry, and vibrational spectra of these species. NICS indices and extra cyclic resonance energies confirm that the compounds in question possess antiaromatic character. For both the bare MC_4H_4 rings and larger complexes, the Be-containing compounds were found to be the most strongly bound species. Such viability is explained via ring strain, electron densities, natural bond orders, and orbital analyses. Given that the second least viable Mg complex has been reported in recent experiments, synthesis and characterization of the other group IIA analogs are anticipated.

2.2 Introduction

Over the past sixty years, synthetic chemists have done remarkable science with metallacyclopentadienes, and many have been proposed as key intermediates in organometallic reactions.[21-30] The metal centers in these species are chiefly inclusive of *d*-block,[21, 22, 31-33] *p*-block,[24, 25, 27] or *f*-block metals.[34, 35] However, reports of alkaline-earth metallacyclopentadienes are much less common, due to their challenging synthesis and subsequent isolation. Direct reactions between dienes and alkaline-earth metals have

been studied since the 1970s,[36-42] and the resulting metal-diene complexes,[38-40, 42] and even some polymers,[36, 37] are known. However, these complexes are not considered here because dienes interact with exocyclic alkaline-earth metals, mainly through π donation, and therefore do not belong to the five-membered cycles discussed above. We are principally interested in probing the viabilities of the latter class of compounds in the present research.

Magnesiacyclopentadienes have been suggested to be short-lived intermediates in synthetic pathways,[23, 43] and berylliacyclopentadienes have been addressed in theoretical work.[44-47] To our knowledge, metallacyclopentadienes with heavier group IIA elements have not been described in the literature. However, sandwich compounds with group IIA metal dimers have been studied.[48] The first successful synthesis and characterization of magnesiacyclopentadienes, as well as the related spiro-dilithio magnesiacyclopentadienes and dimagnesiabutadiene were reported by Wei et al[49] (see Scheme 2.1). Magnesiacyclopentadienes and spiro-dilithio magnesiacyclopentadienes (**1** and **2** in Scheme 2.1, respectively) were first synthesized using 1,4-dilithio 1,3-butadienes as the starting material; this was then treated with a Mg salt ($MgCl_2$), and the X-ray crystal structures of the resultant tetramethylethylenediamine (TMEDA) complexes were reported. Additionally, Wei and coworkers reported an efficient strategy for the synthesis of amino cyclopentadienes from magnesiacyclopentadiene precursors.

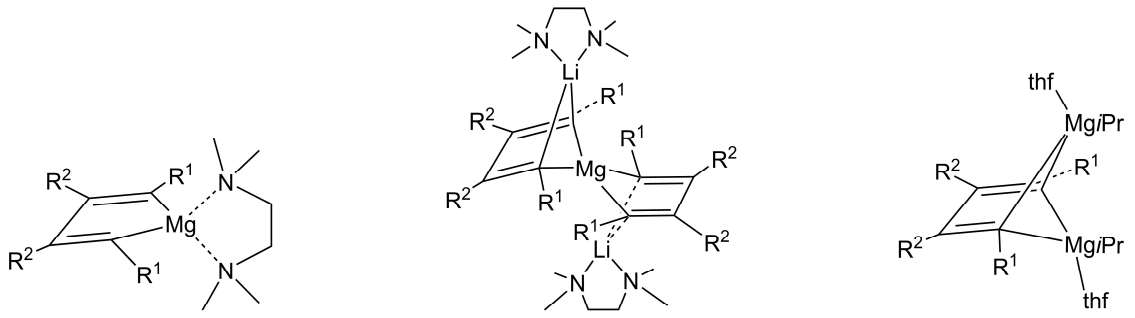

1. *Magnesiacyclopentadienes*
a. $R^1 = SiMe_3$, $R^2 = Me$
b. $R^1 = SiMe_3$, $R^2 = Ph$

2. *Spiro-dilithio magnesiacyclopentadienes*
a. $R^1 = SiMe_3$, $R^2 = Me$
b. $R^1 = R^2 = Et$

3. *Dimagnesiabutadiene*
($R^1 = SiMe_3$, $R^2 = Me$)

Scheme 2.1: Magnesiacyclopentadienes (**1**), spiro-dilithio magnesiacyclopentadienes (**2**), and dimagnesiabutadiene (**3**) compounds synthesized by Wei et al.[49]

Among the three types of compounds synthesized, the unprecedented magnesiacyclopentadienes drew our attention due to their unique five-membered cyclic skeletons and their potential synthetic applications in the production of cyclopentadiene derivatives. Therefore, a more thorough understanding of these complexes, as well as their group IIA analogues, should benefit future endeavors in this field of chemistry. To augment the limited research on this class of compounds, we systemically studied the alkaline-earth metallacyclopentadienes (MC_4H_4, M = Be, Mg, Ca, Sr, and Ba) using density functional and coupled-cluster methods. In view of the stabilizing effect of substituted groups and TMEDA, we extensively investigated and characterized **1a** $MgC_4[Si(CH_3)_3]_2[CH_3]_2$·TMEDA (see Scheme 2.1) and its group IIA congeners as model complexes. The equilibrium geometry, aromaticity, thermochemistry, vibrational frequencies, and other relevant results for each species considered are reported and discussed in detail. Moreover, benchmarking of our DFT results against "gold standard" coupled-cluster theory [i.e., CCSD(T)/cc-pVTZ], as well as the recently reported

experimental results for the synthesized magnesium compound, was performed throughout the paper to help in the selection of reliable theoretical methods for the future study of similar molecular systems.

2.3 Computational Methods

Coupled-cluster (CC) computations of equilibrium geometries and harmonic vibrational frequencies have been performed with single, double, and perturbative triple excitations [CCSD(T)]. For the Sr and Ba atoms, Peterson's pseudopotential-based correlation-consistent polarized valence triple-ζ (cc-pVTZ-pp) basis sets[50] with the Stuttgart/Cologne pseudopotentials [ECP28MDF (Sr): 28 core electrons (1*s*,2*s*,2*p*,3*s*,3*p*,3*d*); and ECP46MDF (Ba): 46 core electrons (1*s*,2*s*,2*p*,3*s*,3*p*,3*d*,4*s*,4*p*,4*d*)][51] were used, and the corresponding cc-pVTZ basis sets of Dunning and coworkers[52-54] were chosen for all other atoms. For the observed $MgC_4[Si(CH_3)_3]_2[CH_3]_2 \cdot$TMEDA molecule, a total 1262 of contracted gaussian basis functions result from this approach. Stringent criteria were set for the SCF densities (10^{-10}), coupled-cluster amplitudes (10^{-9}), and RMS forces (10^{-8} E_h a_0^{-1}). Consistent with the design of the chosen basis sets, core electrons were excluded from the correlation treatment (the "frozen core" approximation). Fundamental vibrational frequencies were obtained by including anharmonic terms computed with second-order vibrational perturbation theory (VPT2).[20] The cubic and semidiagonal quartic force fields were obtained by using numerical differentiations of second derivatives at 29 nuclear displacements of MC_4H_4. Corrections were made to treat problematic Fermi resonances,[55] based on the procedure proposed by Nielsen (see more

details in the Results and Discussion).[56] All CC computations were performed as implemented in the CFOUR 1.0 program package.[57]

We additionally report equilibrium geometries and harmonic vibrational frequencies computed with select density functionals (B3LYP, BP86, and M06-2X) and assess their performance against the CC computations and experimental results. B3LYP includes exact exchange and is calibrated by fitting three parameters to experimental results,[58, 59] while BP86 does not include exact exchange and is deduced by forcing the functional to satisfy certain constraints based on first principles.[60, 61] M06-2X is a hybrid functional which incorporates 54% Hartree-Fock exchange, and was developed more recently by Truhlar's group.[62] It has been suggested to be one of the best functionals for the study of main-group thermochemistry, kinetics, and noncovalent interactions. For the Sr and Ba atoms, the cc-pVTZ-pp and cc-pVQZ-pp basis sets[50] were used with the Stuttgart/Cologne pseudopotentials described above, and the cc-pVTZ and cc-pVQZ basis sets were used for all other atoms. All DFT computations were performed using the ORCA 3.0.3 program package.[63] The SCF densities and the RMS forces were converged using the parameters defined by the "TightSCF" and "TightOpt" keywords in ORCA 3.0.3, respectively. A fine integration grid (i.e., the default parameters implemented in ORCA 3.0.3 for the "Grid6" keyword) was used in all computations to increase the numerical accuracy.

To assess possible multireference character for the molecules in question, CASSCF energy computations of the CC-optimized geometries have been performed using the MOLPRO program package (Version 2010.1).[64, 65] An active space of 14 electrons distributed in 14 orbitals was selected [i.e., CASSCF(14,14)] for all bare MC_4H_4 cycles.

The largest CASSCF reference coefficients C_0 are all >0.94; therefore, >89% of the total wavefunction may be described by a single determinant in every case. Accordingly, we expect single reference methods to properly describe the MC_4H_4 species. The C_0 and C_1 coefficients, along with $\mathcal{T}_1$ diagnostics and the largest t_{ij}^{ab} amplitudes from the CC computations, are provided in the Supporting Information (SI, available online).

We report nucleus-independent chemical shifts (NICS) values, specifically the $NICS(1)_{zz}$ indices, which are the contributions of the out-of-plane *zz* magnetic shielding tensor at points 1 Å above molecular ring centers. These may be obtained computationally and have been reported as promising alternatives to the more involved $NICS(0)_{\pi zz}$ indices (which consider only the π contribution to the out-of-plane *zz* magnetic shielding tensor at the molecular ring centers).[66] The gauge-including atomic orbital[67, 68] method [GIAO-$NICS(1)_{zz}$] was employed to obtain these values. The Stuttgart/Cologne pseudopotentials were used for Sr and Ba atoms in the NICS calculations because a sufficient treatment of relativistic effects was found to be necessary in computing shielding tensors of molecules with heavy atoms.[69, 70] The NICS and Bader's quantum theory of atoms in molecules (QTAIM) computations were performed using the AIMAll (version 16.01.09) program package.[71] Further, the natural bond orbital (NBO) computations were performed using the NBO 6.0 program package.[72]

Pauling-Wheland resonance energies[73-75] have been directly calculated by using the *ab initio* valence-bond-based block-localized wave function (BLW) method developed by Mo and coworkers.[76-79] According to their original definition: the resonance energy is the energy difference between "the actual energy of the molecule in question and that of the most stable contributing structure."[74] We determine the energy of the latter structure

using BLW orbitals constructed by dividing the electrons and basis functions into several subsets, which can "shut down" the intramolecular interactions among those subsets. By carefully selecting and dividing the orbitals responsible for π interactions, certain conjugations may be disabled, allowing us to compute the resonance energy directly without reference molecules or reactions. In the present study, two types of resonance energies have been computed: the vertical resonance energy (VRE) and adiabatic resonance energy (ARE). The VRE has been computed by taking the energy difference between the fully-optimized geometry and the most stable resonance contributor *at the same geometry*.[80, 81] Similarly, the ARE was obtained by taking the energy difference between the fully-optimized geometry and the most stable resonance contributor *optimized using BLW orbitals*.[78, 82]

Following the work of Mo and Schleyer,[78] the extra cyclic resonance energy (ECRE) may be computed by taking the difference between the AREs of a cyclic conjugated molecule and a corresponding acyclic polyene, either with the same number of double bonds[83] or diene conjugations.[84, 85] Therefore, as opposed to the resonance energy (RE), which measures the overall energetic stabilization due to π conjugation (which is always positive, even for nonaromatic and antiaromatic conjugated systems), the ECRE measures the extra stabilization (or destabilization) energy due to the cyclic arrangement of an aromatic (or antiaromatic) molecule. On this basis, the ECRE is constructed to be positive, zero, or negative, indicating aromatic, nonaromatic, or antiaromatic character, respectively.

According to Mo, Hiberty, and Schleyer,[86] the high flexibility of very large basis sets could blur the boundaries of the various BLW resonance structures and thus introduce

"basis set artifacts." Therefore, both the relatively large cc-pVTZ[52] and the smaller 6-31G(d)[87] basis sets are used in all BLW computations for comparison. For consistency with the 6-31G(d) basis set, the SBKJC split valence basis set with its corresponding compact relativistic effective core pseudopotential (ECP)[88] is used for Sr and Ba atoms. Such combination of Pople and SBKJC-ECP basis sets has been successfully applied in recent BLW computations.[89] For the computations with cc-pVTZ, the cc-pVTZ-pp basis set is used with the corresponding Stuttgart/Cologne pseudopotential for the Sr atom, as described above.[90] Specific BLW blocking strategies of RE and ECRE calculations are described in the Results and Discussion. All BLW computations have been performed using the BLW code interfaced with the GAMESS 2013 (R1) program package.[91]

2.4 Results and Discussion

2.4.1 Equilibrium geometries for the prototypical MC_4H_4 molecules

Figure 2.1 compares the optimized equilibrium geometries of bare MC_4H_4 rings from CC and DFT computations. As there are to date very limited experimental reports for related species, the CCSD(T) results are presented as references for comparison. The singlet ground states of all MC_4H_4 species are predicted to be planar with C_{2v} symmetry. Mean absolute deviations (MADs) of the DFT geometric parameters of MC_4H_4 versus the corresponding CCSD(T) results are reported in Table 2.1. The average of the MADs of the bond lengths computed with B3LYP, BP86, and M06-2X (using cc-pVTZ) is 0.018, 0.013, and 0.018 Å, respectively (see Table 2.1). The deviations of the C–M–C angles range from 0.5 to 3.8º (see Figure 2.1). Therefore, all three DFT methods predict MC_4H_4 structures reasonably consistent with the CC results; we find that the BP86 method is

somewhat better than B3LYP and M06-2X. Further, from cc-pVTZ to cc-pVQZ, the DFT bond lengths and angles change only slightly (the largest differences are 0.011 Å and 1.2º, respectively), suggesting that the cc-pVTZ basis set is sufficient to obtain reliable geometries for the MC_4H_4 molecules.

Taking BeC_4H_4 as an example, the bond lengths of Be–C, C–C, and C=C bonds are 1.671, 1.526, and 1.360 Å at the CCSD(T)/cc-pVTZ level, respectively. Accordingly, three single bonds (two Be–C and one C–C) and two C=C double bonds are expected for BeC_4H_4. Similar bond length alternation was found in each of the other optimized MC_4H_4 structures, suggesting the possible antiaromatic nature of these species (as expected from the four π electrons present in the planar molecular ring). This is also supported by positive $NICS(1)_{zz}$ indices (15.6 ppm for BeC_4H_4 and 5.2 ppm for MgC_4H_4; calculated at the B3LYP/aug-cc-pVDZ level by Mazurek and Dobrowolski[47]). The reduced $NICS(1)_{zz}$ values from BeC_4H_4 to MgC_4H_4 coincide with the slightly more balanced C–C and C=C bond lengths in MgC_4H_4 than in BeC_4H_4 [a difference of 0.166 Å for BeC_4H_4 and 0.156 Å for MgC_4H_4 at CCSD(T)/cc-pVTZ]. The Ca, Sr, and Ba species display even more pronounced C–C/C=C bond equalizations. We probe the trends in the aromatic character of the MC_4H_4 rings in the following section.

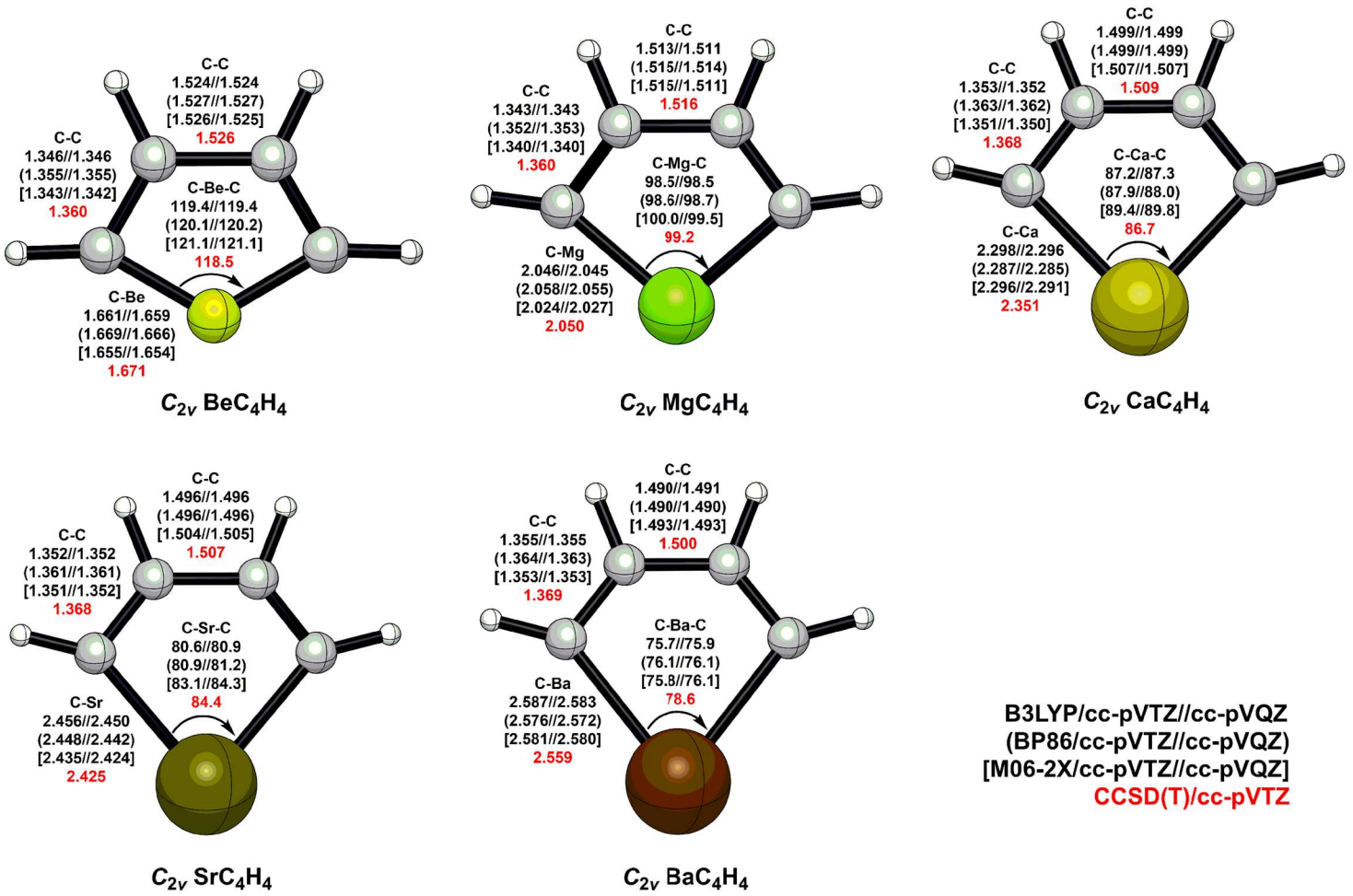

Figure 2.1: Optimized equilibrium geometries of MC_4H_4 (M = Be, Mg, Ca, Sr, and Ba) molecules computed with the DFT (black) and CCSD(T) (red) methods. Distances in Å; angles in degrees. The core electrons of the Sr and Ba atoms have been treated with the pseudopotentials described in the Theoretical Methods section.

Table 2.1: Mean absolute deviations (MADs) of DFT bond lengths (Å) of MC_4H_4 (M = Be, Mg, Ca, Sr, and Ba) against the CCSD(T)/cc-pVTZ results.[a]

Compound	B3LYP/cc-pVTZ	BP86/cc-pVTZ	M06-2X/cc-pVTZ
BeC_4H_4	0.010	0.003	0.013
MgC_4H_4	0.009	0.007	0.019
CaC_4H_4	0.029	0.030	0.029
SrC_4H_4[b]	0.021	0.014	0.011
BaC_4H_4[b]	0.019	0.011	0.017
Average	0.018	0.013	0.018

[a] The M–C, C–C, and C=C bonds are included for the calculation of MADs.
[b] The core electrons of the Sr and Ba atoms have been treated with the pseudopotentials described in the Theoretical Methods section.

2.4.2 Aromatic character of MC_4H_4 molecules

In Table 2.2 we present $NICS(1)_{zz}$ indices computed with the B3LYP/6-31G(d) and B3LYP/cc-pVTZ methods. The selected basis sets give comparable results, although the 6-31G(d) values are consistently higher than those computed with the cc-pVTZ basis set. The $NICS(1)_{zz}$ values for BeC_4H_4 and MgC_4H_4 generally agree with those obtained by Mazurek and Dobrowolski with the B3LYP/aug-cc-pVDZ method.[47] All $NICS(1)_{zz}$ indices are positive, further reflecting the antiaromatic nature of these compounds. In general, $NICS(1)_{zz}$ values decrease from BeC_4H_4 to BaC_4H_4 with both of our basis sets. The only exception occurs for the B3LYP/cc-pVTZ result of CaC_4H_4 (1.89 ppm), which is lower than both SrC_4H_4 (2.75 ppm) and BaC_4H_4 (2.29 ppm); this could conceivably be a result of the use of ECPs for Sr and Ba, which may produce some inconsistency. The decreasing trend in $NICS(1)_{zz}$ values agrees with the slight degree of C–C/C=C bond equalizations from BeC_4H_4 to BaC_4H_4 (see Figure 2.1), corresponding to a concomitant decrease in antiaromaticity. With the exception of BeC_4H_4, the $NICS(1)_{zz}$ values of the

other species are relatively small and close to one another, indicating only slight antiaromaticity.

Based on Mo and Schleyer's approach for five-membered diene ring systems,[78] a BLW blocking scheme for MC_4H_4 species and linear analogues is selected in Scheme 2.2. The structures on the left depict the fully delocalized molecules, and the structures on the right are the corresponding most important contributors under the BLW blocking scheme. By definition (see Theoretical Methods), the energy differences between left and right structures constitute the REs (Table 2.3). We note that there are two possible linear counterparts to MC_4H_4: one with the same number of double bonds[83] or one with the same number of diene conjugations (i.e., the same type and number of single bonds between the π segments).[78, 84, 85] As the latter has been shown to be an improved model over the former,[78, 85] we selected this structure as an acyclic reference for our ECRE computations (see Scheme 2.2).

Table 2.2: Nucleus independent chemical shifts reported are the $NICS(1)_{zz}$ indices (total MO contribution to the zz component of the NICS tensor; in ppm) for the MC_4H_4 (M = Be, Mg, Ca, Sr, and Ba) molecules.

Compound	B3LYP/6-31G(d)	B3LYP/cc-pVTZ
BeC_4H_4	16.31	14.97
MgC_4H_4	5.97	4.59
CaC_4H_4	4.87	1.89
SrC_4H_4[a]	4.39	2.75
BaC_4H_4[a]	3.55	2.29

[a] The core electrons of the Sr and Ba atoms have been treated with the pseudopotentials described in the Theoretical Methods section.

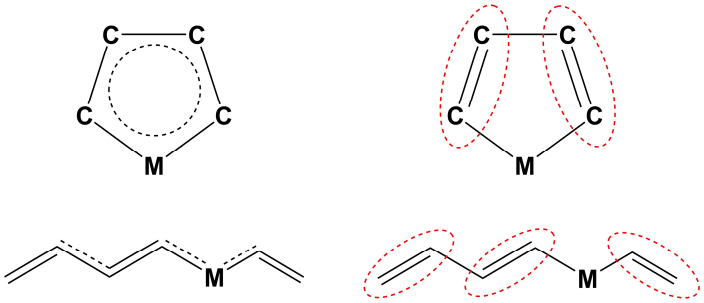

Scheme 2.2: The BLW blocking scheme (red dashed circles) for the alkaline-earth metallacyclopentadienes and their linear counterparts with the same number of diene conjugations (left: delocalized molecules without BLW constraints; right: most favored BLW resonance contributors). H atoms not shown for clarity.

Table 2.3 VREs, AREs, and ECREs of MC_4H_4 (M = Be, Mg, Ca, Sr, and Ba) molecules computed with B3LYP/6-31G(d) and B3LYP/cc-pVTZ (in parentheses).[a]

Compound	VRE	ARE	ECRE
BeC_4H_4	17.5 (14.5)	16.3 (13.5)	-6.7 (-6.3)
MgC_4H_4	15.1 (12.4)	13.8 (11.0)	-5.3 (-4.6)
CaC_4H_4	23.2 (17.5)	20.8 (15.4)	-4.2 (-3.9)
SrC_4H_4[b]	12.3 (16.2)	10.9 (14.3)	-4.7 (-3.3)
BaC_4H_4[b,c]	12.0 (N.A.)	10.6 (N.A.)	-4.4 (N.A.)

[a] All energies are in kcal/mol.
[b] The core electrons of the Sr and Ba atoms have been treated with the pseudopotentials described in the Theoretical Methods section.
[c] The cc-pVTZ data for BaC_4H_4 is not available; see reference 90.

Fully-optimized and BLW-optimized (where the optimization is performed with the BLW blocking shown in Scheme 2.2) structures of MC_4H_4 are shown in Figure 2.2. In the case of either fully-optimized or BLW-optimized (see Block-Localized Methods section above) geometries, the C–C and C=C bond length variations caused by increasing basis set size [from 6-31G(d) to cc-pVTZ] are relatively minor. The MADs observed in

the fully-optimized C–C and C=C bond lengths were 0.008 Å and 0.006 Å, respectively; for the BLW-optimized structures, these values were 0.007 Å and 0.006 Å, respectively. We find larger changes in the M–C bond lengths (MADs of 0.025 Å and 0.022 Å for fully- and BLW-optimized structures, respectively).

With B3LYP/6-31G(d), BLW blocking shortens the C=C bond length by 0.012 Å on average, while it elongates the C–C and M–C single bonds by 0.038 and 0.008 Å on average, respectively. B3LYP/cc-pVTZ gives similar results, with average variations of C=C, C–C, and M–C bond lengths being -0.012, +0.041, and +0.009 Å, respectively. Clearly, "shutting down" the π conjugation via BLW has a greater impact on the C–C and C=C bond lengths than on the M–C bond lengths, indicating that the conjugation mainly occurs among the C atoms. For comparison, the C–C and C=C bond length variations here are, in general, less than those (up to 0.142 Å) in the highly aromatic five-membered diene systems reported in Mo and Schleyer's study.[78]

The results of the BLW analyses indicate that:

(1) the MC_4H_4 geometries are only modestly basis-set dependent;

(2) relative to highly aromatic systems, there is significantly smaller bond equalization present in the MC_4H_4 rings, indicating less π conjugation and non-negligible antiaromatic character;

(3) modest changes from fully- and BLW-optimized geometries imply that the σ framework plays a larger role in dictating molecular structure than does the π system.

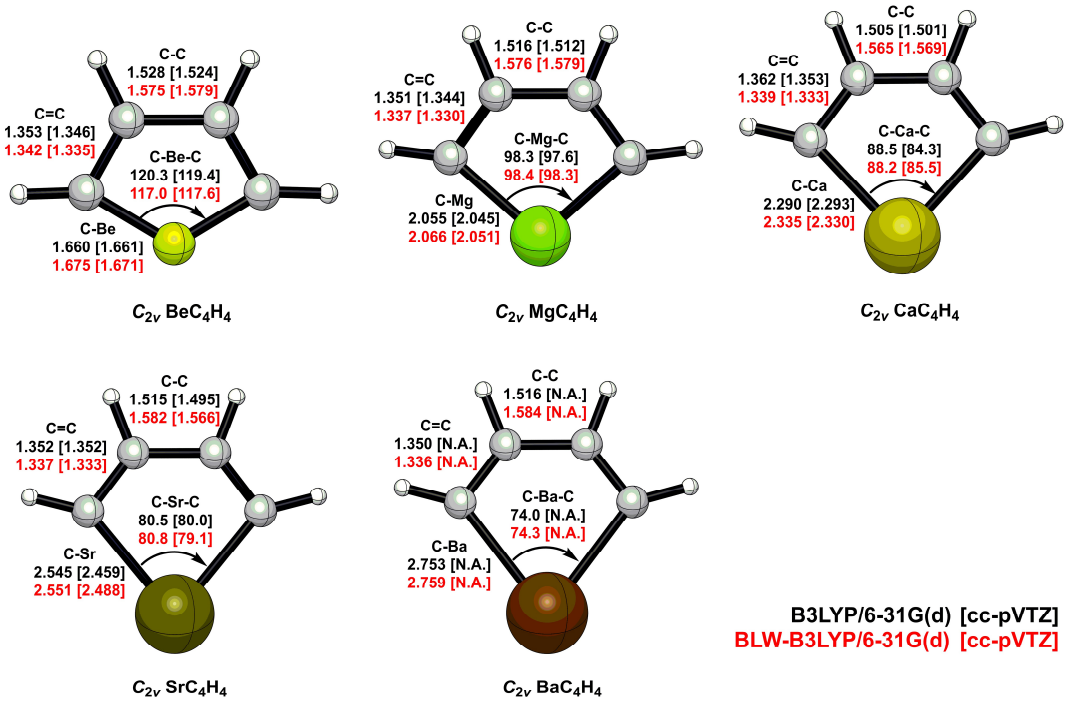

Figure 2.2: Fully-optimized (black) and BLW-optimized (red) structures of MC_4H_4 (M = Be, Mg, Ca, Sr, and Ba) computed with B3LYP/6-31G(d) and B3LYP/cc-pVTZ (cc-pVTZ results for BaC_4H_4 not available; see reference 90). Distances in Å; angles in degrees. The core electrons of the Sr and Ba atoms have been treated with the pseudopotentials described in the Theoretical Methods section.

The VREs, AREs, and ECREs are reported in Table 2.3. The differences between the B3LYP/6-31G(d) and B3LYP/cc-pVTZ VREs and AREs range from 2.7–5.7 kcal/mol. The VREs and AREs are consistent with the geometric changes between the fully- and BLW-optimized structures shown in Figure 2.2; in general, larger geometric changes (especially for the C=C and M–C bond lengths) give higher REs, and vice versa. The computed VREs and AREs are not exceptionally high (B3LYP/cc-pVTZ values range from 11.0–17.5 kcal/mol), indicating relatively weak π conjugation.

Neither the VRE nor ARE is suitable to measure aromaticity directly because they only evaluate the overall π conjugation (see Theoretical Methods). However, the ECREs,

which are derived from the AREs of the cyclic MC_4H_4 structures and their linear counterparts (see Scheme 2.2), serve as better indicators of aromaticity (see Theoretical Methods). The ECREs presented in Table 2.3 are all negative, indicating antiaromatic character [which agrees with the positive $NICS(1)_{zz}$ indices reported in Table 2.2]. From BeC_4H_4 to BaC_4H_4, the B3LYP/cc-pVTZ ECRE values decrease in magnitude, which also correlates with the generally decreasing trend in $NICS(1)_{zz}$ values and the increasing C–C/C=C bond length equalization seen in Figure 2.1. Based on the magnetic and energetic data presented here, we conclude that the alkaline-earth metallacyclopentadienes are antiaromatic.

2.4.3 Thermochemistry of MC_4H_4 species

The dissociation of MC_4H_4 is defined in reaction (2.1). The corresponding dissociation energies D_0 and MADs [of DFT versus CCSD(T) results] are reported in Table 2.4.

$$MC_4H_4 \rightarrow C_4H_4 + M \qquad (2.1)$$

The optimization for isolated cyclobutadiene (C_4H_4) was performed with D_{2h} symmetry, as the $\tilde{X}\ ^1A_g$ global minimum of C_4H_4 has been widely understood to be a planar rectangular molecule.[92-94] The CCSD(T)/cc-pVTZ D_0 values of MC_4H_4 range from 38.5-84.6 kcal/mol. For DFT results, we find the largest deviations of D_0 (7.1-16.9 kcal/mol) for BeC_4H_4 and CaC_4H_4 when compared to the CCSD(T) results. The analogous deviations are smaller (< 6.0 kcal/mol) for MgC_4H_4, SrC_4H_4, and BaC_4H_4. The MADs of D_0 [versus CCSD(T)/cc-pVTZ] for B3LYP, BP86, and M06-2X (also using cc-

pVTZ) are 5.0, 6.9, and 5.2 kcal/mol, respectively; therefore, B3LYP and M06-2X display better performance than BP86 in predicting D_0. As with the determination of equilibrium geometries, the DFT dissociation energies do not change significantly from cc-pVTZ to cc-pVQZ (the differences are < 1.0 kcal/mol). We thus establish that the cc-pVTZ basis set is sufficient for determining reliable D_0 values for the MC_4H_4 molecules.

Both CCSD(T) and DFT methods predict that BeC_4H_4 is the most strongly bound MC_4H_4 compound, while a sharp decrease of D_0 occurs for MgC_4H_4, making it perhaps the least viable species. Recall that both the $NICS(1)_{zz}$ indices (see Table 2.2) and ECREs (see Table 2.3) suggest that BeC_4H_4 is more antiaromatic than MgC_4H_4. BeC_4H_4 might therefore be expected to be *less* viable than MgC_4H_4, which is apparently contradictory to our computed dissociation energies. We thus surmise that the difference in antiaromatic character is not the reason for the significant D_0 difference between BeC_4H_4 and MgC_4H_4.

An evaluation of the MC_4H_4 ring strain (Scheme 2.3) provides further insight. The homodesmotic reaction used here to evaluate the MC_4H_4 ring strain is modified from a similar homodesmotic reaction employed for cyclopentadiene by Wheeler et al.[95] With BLW, we "shut down" the π conjugations on both sides of the reaction, so the resulting energetic imbalance between reactants and products is mainly due to the molecular frameworks of the associated compounds (see Scheme 2.3; note that we also BLW-block the C=C double bonds in propene and ethylene to exclude *σ-p* hyperconjugation, which contributes ~9 kcal/mol total). Because the other molecules (i.e., besides MC_4H_4) in the homodesmotic reaction are "strain-free," the energies reported in Scheme 2.3 reflect the ring strain of MC_4H_4.

Table 2.4: Dissociation energies (D_0, kcal/mol) of MC_4H_4 (M = Be, Mg, Ca, Sr, and Ba) molecules computed with DFT and CCSD(T) using the cc-pVTZ and cc-pVQZ (in parentheses) basis sets.[a]

Compound	B3LYP	BP86	M06-2X	CCSD(T)[b]
BeC_4H_4	94.5 (95.0)	93.6 (94.0)	96.8 (96.6)	84.6
MgC_4H_4	39.4 (39.9)	40.9 (41.2)	41.2 (40.8)	38.5
CaC_4H_4	58.7 (59.1)	63.9 (64.1)	54.4 (54.3)	47.2
SrC_4H_4[c]	49.6 (50.4)	53.1 (54.0)	47.9 (48.6)	51.5
BaC_4H_4[c]	59.1 (59.9)	63.2 (64.1)	57.9 (58.2)	58.3
MADs[d]	5.0	6.9	5.2	-

[a] Bond dissociation reaction is defined in reaction (2.1); ZPVE corrections are included for all species.
[b] Only cc-pVTZ results computed.
[c] The core electrons of the Sr and Ba atoms have been treated with the pseudopotentials described in the Theoretical Methods section.
[d] Versus CCSD(T)/cc-pVTZ values.

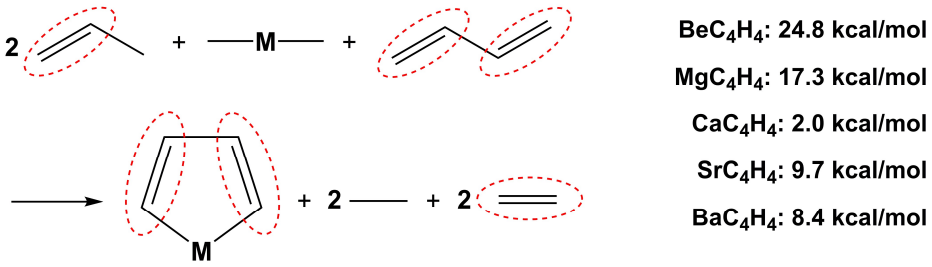

Scheme 2.3: Homodesmic reaction for the B3LYP/6-31G(d) energetic evaluation of the ring strain in MC_4H_4 (M = Be, Mg, Ca, Sr, and Ba) with BLW blocking (red dashed circles).

In Scheme 2.3, the ring strain for BeC_4H_4 is predicted to be 24.8 kcal/mol (the highest reported value!) Once again, this seems contrary to our prediction of BeC_4H_4 possessing the highest dissociation energy, which we would predict to have the lowest D_0 based on the ring strain data alone. The main origin of the high ring strain of BeC_4H_4 is the M–C_1–C_2 angle (only ~90º), which is much smaller than the "strain-free" C_2–C_1–H angle

(~120º). Based on this rationale, the ring strain of MgC_4H_4 is also high (17.3 kcal/mol, with a M–C_1–C_2 angle of 94.8º). The smallest ring strain (2.0 kcal/mol) was found for CaC_4H_4, which may be traced to a further increasing M–C_1–C_2 angle (97.4º). Although this angle keeps increasing for SrC_4H_4 (98.8º) and BaC_4H_4 (101.3º), their ring strains (9.7 and 8.4 kcal/mol for SrC_4H_4 and BaC_4H_4, respectively) are larger than that of CaC_4H_4, which may be attributed to their much smaller C–M–C angles (84.4º for SrC_4H_4 and 78.6º for BaC_4H_4). Although this ring strain analysis cannot explain (and even contradicts) the trends in dissociation energies, they remain important factors in evaluating the viabilities of the MC_4H_4 compounds.

We address this discrepancy by noting that reaction (2.1) needs to break the M–C bonds. Therefore, we would expect the M–C bond strengths to correlate with the dissociation energies. Our NBO and QTAIM analyses characterize the M–C bonds in the MC_4H_4 systems as constituting both shared-shell (covalent) and closed-shell (ionic) interactions (see detailed QTAIM and NBO results in the SI). Several reasons are proposed here to explain the distinct dissociation energies of BeC_4H_4 (84.6 kcal/mol) and MgC_4H_4 (38.5 kcal/mol): (1) recent QTAIM studies have established a strong correlation between the electron density at the bond critical point (BCP) and the bond strength for various types of bonding interactions.[96-98] The electron densities at the BCPs of the Be–C and Mg–C bonds (see Table 2.5) are 0.1013 and 0.0580 a.u., respectively. Accordingly, the Be–C interaction is expected to be stronger than the Mg–C interaction; (2) the NBO analysis shows the natural bond order of the Mg–C bond to be the lowest one (0.49), whereas the bond order of the Be–C bond is higher by 0.23, supporting the results of the QTAIM computations; (3) the HOMO-LUMO gap decreases from BeC_4H_4 to BaC_4H_4.

The value for BeC_4H_4 is 102.4 kcal/mol, higher than that of MgC_4H_4 by 17.0 kcal/mol (see Table 2.5); and (4) since the Be and C atoms are from the same row in the periodic table, the orbitals involved in Be–C bonding are expected to be more balanced in size than the orbitals involved in other M–C interactions. In addition, sp^2 hybridization would be easier in Be due to the small 2s-2p energy gap (as compared to Mg). As a consequence, more favorable orbital overlap, and the corresponding MO splitting, are expected for the case of BeC_4H_4 than for the other congeners. This may also be used as a qualitative explanation for the decreasing trend in HOMO-LUMO gaps (see Table 2.5).

To summarize, the trends in the different dissociation energies of the MC_4H_4 series are mainly caused by two factors: ring strain and M–C bond strength. Although the ring strain of BeC_4H_4 is found to be highest, its strongest M–C bonding makes it the most thermodynamically viable species. Relatively high ring strain, combined with weak Mg–C interaction, make MgC_4H_4 the least viable of the MC_4H_4 series. The dissociation energies of the other three species may be explained similarly.

Table 2.5: QTAIM electron densities (ρ, a.u.) at the bond critical points (BCPs), natural bond orders for M–C bonds (M = Be, Mg, Ca, Sr, and Ba), and HOMO-LUMO gaps (kcal/mol) for MC_4H_4 molecules computed with B3LYP/cc-pVTZ.

Compound	ρ_{BCP} (M-C)	Natural bond order (M–C)[a]	Natural charge (C/M)	HOMO-LUMO gap
BeC_4H_4	0.101	0.72/0.71/0.71	-0.86/1.43	102.4
MgC_4H_4	0.058	0.49/0.49/0.49	-0.77/1.39	85.4
CaC_4H_4	0.063	0.95/0.95/0.95	-0.80/1.50	76.6
SrC_4H_4	0.056	0.94/0.93/0.95	-0.79/1.50	72.3
BaC_4H_4	0.059	0.95/0.95/0.96	-0.82/1.56	72.3

[a] [B3LYP/BP86/M06-2X]/cc-pVTZ.

2.4.4 Vibrational frequencies of MC_4H_4 structures

Due to their elusive nature, the bare MC_4H_4 rings have not been identified by experiments so far (see Introduction). Therefore, we provide the harmonic vibrational frequencies and anharmonic corrections of all 21 normal modes for the two smallest MC_4H_4 species (M = Be and Mg; Tables 2.6 and 2.7) to aid in the characterization of these species in future experimental work. Mean absolute percentage errors (MAPEs) of harmonic frequencies against CCSD(T)/cc-pVTZ harmonic frequencies are also reported to evaluate the performance of different density functionals. Harmonic vibrational frequencies of the other MC_4H_4 compounds (M = Ca, Sr, and Ba) are reported in the supporting information.

For both BeC_4H_4 and MgC_4H_4, all vibrational modes are IR- and Raman-active except for ν_9, ν_{10}, and ν_{11}, which are IR-inactive but Raman-active (a_2 symmetry in the C_{2v} point group). For BeC_4H_4 (Table 2.6), one vibrational mode (ν_2) suffers from a Fermi Type I resonance ($\omega_2 \approx 2\omega_{17}$).[55] Based on the procedure proposed by Nielsen,[56] terms with small denominators in the VPT2 analysis were excluded, and the energetic effect of neglecting such terms was estimated by constructing and diagonalizing the effective vibrational Hamiltonian matrix shown in equation (2.2). The corrected fundamental frequency ν_2 is 3001 cm^{-1}, (a correction of +13.4 cm^{-1}). For MgC_4H_4 (Table 2.7), two vibrational modes (ν_2 and ν_{16}) suffer from Fermi Type I ($\omega_2 \approx 2\omega_{17}$) and Type II ($\omega_{16} \approx \omega_3 + \omega_{17}$) resonances, respectively. Similar effective vibrational Hamiltonian matrices [equations (2.2) and (2.3)] are constructed to correct the two frequencies. The resulting fundamental frequencies ν_2 and ν_{16} are 2944 cm^{-1} (a correction of -10.6 cm^{-1}) and 2953 cm^{-1} (a correction of +20.0 cm^{-1}), respectively.

$$\begin{pmatrix} 2\omega_{17} & \phi_{17,17,2}/4 \\ \phi_{17,17,2}/4 & \omega_2 \end{pmatrix} \tag{2.2}$$

$$\begin{pmatrix} \omega_3 + \omega_{17} & \phi_{3,17,16}/\sqrt{8} \\ \phi_{3,17,16}/\sqrt{8} & \omega_{16} \end{pmatrix} \tag{2.3}$$

Unlike the B3LYP and M06-2X methods, which predict harmonic frequencies to be mostly higher than the corresponding CCSD(T) harmonic frequencies, negative deviations are found for most BP86 harmonic frequencies. The MAPEs of harmonic frequencies of BeC_4H_4 versus the CCSD(T) harmonic frequencies are 1.3%, 2.6%, and 2.7%, for B3LYP, BP86, and M06-2X, respectively. Corresponding MAPEs for MgC_4H_4 are 1.7%, 2.7%, and 2.5%, for B3LYP, BP86, and M06-2X, respectively, consistent with the results for BeC_4H_4. Therefore, B3LYP outperforms the other two density functionals.

For BeC_4H_4, the most intense vibrations are (in descending order): ν_{13} (C–H wagging, 611 cm^{-1}, intensity 141 km/mol), ν_8 (ring deformation, 416 cm^{-1}, intensity 109 km/mol), ν_{14} (ring deformation, 364 cm^{-1}), ν_{20} (ring deformation, 1017 cm^{-1}), ν_{19} (ring deformation, 1117 cm^{-1}) ν_2 (C–H stretching, 3001 cm^{-1}), and ν_5 (C–C stretching, 1056 cm^{-1}). For MgC_4H_4, the most intense vibrations are (in descending order): ν_{13} (C–H wagging, 610 cm^{-1}, intensity 132 km/mol), ν_{20} (ring deformation, 755 cm^{-1}, intensity 101 km/mol), ν_2 (C–H stretching, 2944 cm^{-1}), ν_{14} (ring deformation, 245 cm^{-1}), ν_8 (ring deformation, 301 cm^{-1}), ν_{15} (C–H stretching, 3033 cm^{-1}), and ν_4 (C–H rock and C–C stretching, 1304 cm^{-1}). These vibrations are anticipated to be observable by experiment.

Table 2.6: Fundamental (Fund) and harmonic (Harm) vibrational frequencies (cm^{-1}) for BeC_4H_4 with harmonic IR intensities (km/mol) computed with the DFT/cc-pVTZ and CCSD(T)/cc-pVTZ methods.

Mode	Sym	Harm (B3LYP)	Harm (BP86)	Harm (M06-2X)	Harm [CCSD(T)]	Fund [CCSD(T)]	Intensity [CCSD(T)]	Description
ν_1	a_1	3217	3151	3252	3227	3089	2	sym C-H str
ν_2	a_1	3095	3018	3134	3126	3001[a]	43	asym C-H str
ν_3	a_1	1498	1449	1546	1480	1435	6	asym C=C str
ν_4	a_1	1332	1286	1340	1327	1301	5	C-H rock & C-C str
ν_5	a_1	1074	1036	1075	1069	1056	24	C-H scis & C-C str
ν_6	a_1	881	861	901	890	871	17	sym C-C str
ν_7	a_1	774	752	786	777	766	6	asym C-Be str
ν_8	a_1	425	406	386	431	416	109	sym ring deform
ν_9	a_2	1002	959	1030	972	954	0	C-H twist
ν_{10}	a_2	772	744	778	753	745	0	C-H wag
ν_{11}	a_2	292	271	296	275	279	0	ring deform
ν_{12}	b_1	1004	962	1032	978	958	2	C-H wag
ν_{13}	b_1	634	609	636	625	611	141	C-H wag
ν_{14}	b_1	373	358	369	366	364	57	ring deform
ν_{15}	b_2	3216	3151	3251	3226	3090	8	asym C-H str
ν_{16}	b_2	3078	3001	3119	3111	2982	11	asym C-H str
ν_{17}	b_2	1584	1538	1620	1553	1512	2	asym C=C str
ν_{18}	b_2	1298	1252	1310	1290	1263	0	C-H rock & C-C str & C-Be str
ν_{19}	b_2	1141	1111	1168	1133	1117	28	ring deform
ν_{20}	b_2	1035	1005	1046	1037	1017	50	ring deform
ν_{21}	b_2	648	624	650	646	663	1	ring deform
		1.3%[b]	2.6%[b]	2.7%[b]	2.4%[c]			

[a] Deperturbed frequency for mode ν_2: 2988 cm^{-1} (Fermi Type I resonance: $\omega_2 \approx 2\omega_{17}$).
[b] MAPEs of DFT harmonic frequencies versus CCSD(T)/cc-pVTZ harmonic frequencies.
[c] MAPE of CCSD(T) harmonic frequencies versus CCSD(T)/cc-pVTZ fundamental frequencies.

Table 2.7: Fundamental (Fund) and harmonic (Harm) vibrational frequencies (cm^{-1}) for MgC_4H_4 with harmonic IR intensities (km/mol) computed with the DFT/cc-pVTZ and CCSD(T)/cc-pVTZ methods.

Mode	Sym	Harm (B3LYP)	Harm (BP86)	Harm (M06-2X)	Harm [CCSD(T)]	Fund [CCSD(T)]	Intensity [CCSD(T)]	Description
ν_1	a_1	3164	3100	3202	3173	3035	18	sym C-H str
ν_2	a_1	3063	2987	3109	3090	2944[a]	71	asym C-H str
ν_3	a_1	1495	1446	1547	1480	1422	2	asym C=C str
ν_4	a_1	1339	1292	1348	1330	1304	22	C-H rock & C-C str
ν_5	a_1	1091	1051	1098	1089	1073	0	C-H scis & C-C str
ν_6	a_1	839	820	857	847	828	0	sym C-C str
ν_7	a_1	631	610	659	634	624	0	sym C-Mg str
ν_8	a_1	317	308	304	306	301	58	sym ring deform
ν_9	a_2	990	946	1022	968	950	0	C-H twist
ν_{10}	a_2	783	752	791	772	757	0	C-H wag
ν_{11}	a_2	250	238	249	231	231	0	ring deform
ν_{12}	b_1	1006	960	1033	986	966	4	C-H wag
ν_{13}	b_1	631	608	636	618	610	132	C-H wag
ν_{14}	b_1	257	249	242	245	245	68	ring deform
ν_{15}	b_2	3163	3099	3201	3172	3033	30	asym C-H str
ν_{16}	b_2	3040	2965	3089	3070	2953[b]	8	asym C-H str
ν_{17}	b_2	1597	1550	1630	1560	1525	9	asym C=C str
ν_{18}	b_2	1287	1241	1301	1274	1249	11	C-H rock & C-C str
ν_{19}	b_2	1095	1051	1106	1099	1083	5	ring deform
ν_{20}	b_2	767	739	780	766	755	101	ring deform
ν_{21}	b_2	524	507	551	532	526	4	ring deform
		1.7%[c]	2.7%[c]	2.5%[c]	2.3%[d]			

[a] Deperturbed frequency for mode ν_2: 2954 cm^{-1} (Fermi Type I resonance: $\omega_2 \approx 2\omega_{17}$).
[b] Deperturbed frequency for mode ν_{16}: 2933 cm^{-1} (Fermi Type II resonance: $\omega_{16} \approx \omega_3 + \omega_{17}$).
[c] MAPEs of DFT harmonic frequencies versus CCSD(T)/cc-pVTZ harmonic frequencies.
[d] MAPE of CCSD(T) harmonic frequencies versus CCSD(T)/cc-pVTZ fundamental frequencies.

2.4.5 The experimentally observed magnesiacyclopentadiene complex and its group IIA analogues

The TMEDA-coordinated magnesiacyclopentadiene complex synthesized by Wei et al.[49] (denoted as Mg-complex in Figure 2.3) has been optimized with three density functionals in the present study. In addition, the equilibrium geometries of its analogues with other group IIA metals (Be, Ca, Sr, and Ba) were also predicted. These results are summarized in Figures 2.3 and 2.4, and Table 2.8.

The theoretical and experimental structures of the Mg-complex are reported in Figure 2.3. Compared to the experimental structure, the MADs of the bond lengths (C–C, C=C, and Mg–C) for B3LYP, BP86, and M06-2X are 0.010, 0.008, and 0.022 Å, respectively. The deviations of the C–Mg–C angle for B3LYP, BP86, and M06-2X are 1.3, 1.2, and 2.1º, respectively. Therefore, all three density functionals predict reliable structures for the full Mg-complex. However, B3LYP and BP86 exhibit better performance than M06-2X in predicting structures, similar to the bare MC_4H_4 rings (benchmarking against coupled-cluster results). In addition, from the bare MgC_4H_4 ring (Figure 2.1) to the Mg-complex (Figure 2.3), all bond distances in the five-membered ring are elongated, likely due to the steric effects of the substituted groups (Me and $SiMe_3$) and the coordinated TMEDA in the Mg-complex. Due to the same reason, the dihedral angles detailed in Figure 2.4 indicate that the five-membered MgC_4H_4 ring in the center of Mg-complex deviates slightly from planarity. This is consistent with the experimental report that the MgC_4H_4 ring skeleton is "nearly coplanar."[49]

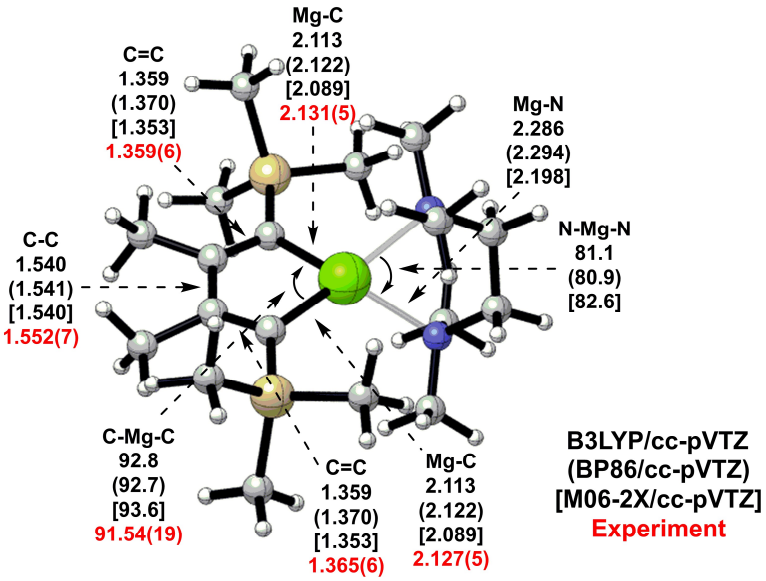

TMEDA-coordinated magnesiacyclopentadiene complex (Mg-Complex)

Figure 2.3: TMEDA-coordinated magnesiacyclopentadiene complex (Mg-Complex) computed with three density functionals and the cc-pVTZ basis set. Distances in Å; angles in degrees. Results in red are from the experimental single-crystal X-ray structural analysis.[49]

Considering the notably improved performance over M06-2X, only B3LYP and BP86 are selected to study the other group IIA analogues of Mg-complex (see Figure 2.4).[49] Similar to the case of the Mg-complex, the bond distances in the five-membered rings are, in general, elongated slightly from the bare MC_4H_4 ring (see Figure 2.1) to the M-complex, whereas the C–M–C angles become smaller, probably caused by the steric effect of the large groups around the MC_4H_4 ring. As with the case of the Mg-Complex, the non-zero dihedral angles [τ(C–C–C–C) and τ(C–C–M–C)] in Figure 2.4 imply that the five-membered MC_4H_4 ring in those complexes deviates from planarity. In particular, such nonplanarity increases from the Be- to the Ba-complex, due to the increasing size of the metal atom and the resulting steric hindrance.

The dissociation reactions of the TMEDA-coordinated metallacyclopentadiene complexes are defined in Scheme 2.4. Dissociation energies are reported in Table 2.8. The D_0 values range from 56.3-113.3 kcal/mol at the B3LYP/cc-pVTZ level. The BP86 D_0 values are reasonably close to the B3LYP results (differences range from 2.3-6.4 kcal/mol). The dissociation energies increase from the bare MC_4H_4 rings to their corresponding M-complexes, as expected from the coordination of TMEDA toward the metal atom, satisfying the octet rule. In addition, the substituted groups (-$SiMe_3$ and -Me) can interact with C=C bonds through *σ-p* hyperconjugation, and these bulky groups also protect the MC_4H_4 ring via steric effects. These effects help to stabilize the molecules, thus making experimental isolation of the Mg-complex practical.[49] As with the bare MC_4H_4 rings, the Mg-complex is also found to have the lowest dissociation energy among all five complexes (see Table 2.8), based on the same reasons proposed for MgC_4H_4. Therefore, since Mg-complex has been isolated by experiment, the isolation of its group IIA analogues should be amenable to future experimental work.

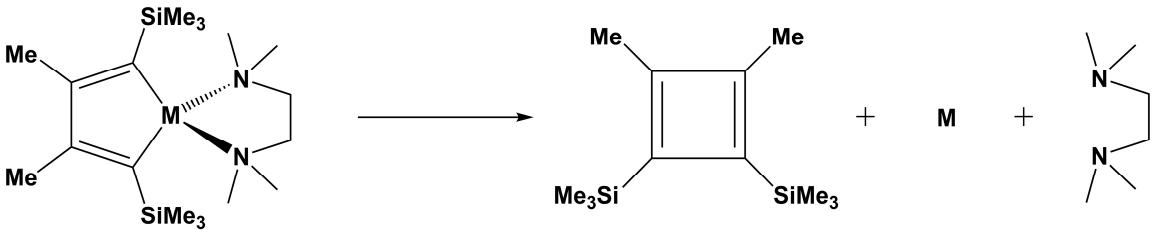

TMEDA-coordinated metallacyclopentadiene complexes (M = Be, Mg, Ca, Sr, and Ba)

Scheme 2.4: Dissociation reactions defined for the TMEDA-coordinated substituted metallacyclopentadiene complexes.

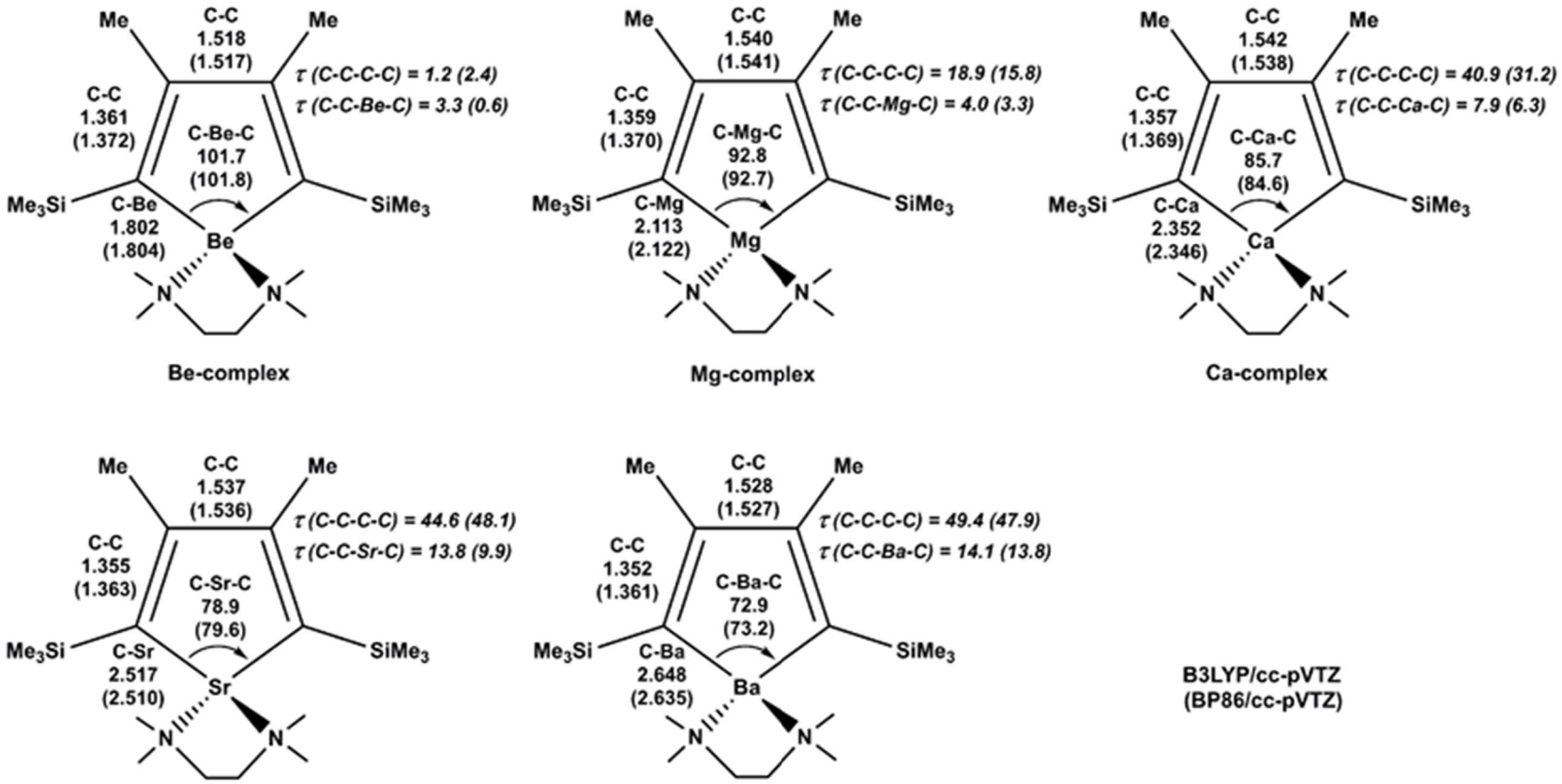

Figure 2.4: TMEDA-coordinated metallacyclopentadiene structures predicted with two density functionals and the cc-pVTZ basis set. Distances in Å; angles in degrees.

Table 2.8: Dissociation energies (D_0, kcal/mol) of TMEDA-coordinated metallacyclopentadiene complexes computed with two density functionals and the cc-pVTZ basis set.[a]

Compound	B3LYP	BP86
Be-complex	113.3	116.5
Mg-complex	58.6	60.9
Ca-complex	70.6	76.2
Sr-complex[b]	56.3	61.4
Ba-complex[b]	61.3	67.7

[a] ZPVE corrections are included for all species.
[b] The core electrons of the Sr and Ba atoms have been treated with the pseudopotentials described in the Theoretical Methods section.

2.5 Conclusions

We have provided an extensive predictive study of alkaline-earth metallacyclopentadienes and the recently synthesized magnesium complex $MgC_4[Si(CH_3)_3]_2[CH_3]_2$·TMEDA using density functional and coupled-cluster methods. The popular B3LYP, BP86, and M06-2X functionals all perform reasonably when benchmarked against both CCSD(T) and experimental (Mg compound only) results for structures, dissociation energies, and vibrational frequencies. We found that the cc-pVTZ basis set is of sufficient size and composition to capture reliable geometric parameters when paired with the selected density functionals. Our results lead to the following conclusions:

(1) The ground-state global minimum of the bare MC_4H_4 rings (M = Be, Mg, Ca, Sr, and Ba) are predicted to possess C_{2v} symmetry. Bond length alternation was found for each of the optimized MC_4H_4 structures, suggesting the antiaromatic nature of these species. This was confirmed by positive nucleus independent chemical shift $NICS(1)_{zz}$

indices and negative extra cyclic resonance energies from block-localized wavefunction computations. We also observed a decreasing trend in antiaromatic character from BeC_4H_4 to BaC_4H_4, supported by a modestly increasing trend in C–C/C=C bond length equalization.

(2) For both the bare MC_4H_4 structures and the experimentally relevant substituted complexes, the Mg- and Be-containing compounds were found to be the second least and most viable species, respectively. Such distinct viability is principally attributed to the large differences in the Be–C and Mg–C bond strengths, which was justified by electron densities at bond critical points, natural bond orders, and MO analyses. Ring strain also proved to be a non-negligible factor in determining the relative viabilities of the MC_4H_4 compounds.

(3) Using second-order vibrational perturbation theory (VPT2), we computed reliable anharmonic corrections to CCSD(T)/cc-pVTZ harmonic vibrational frequencies for the BeC_4H_4 and MgC_4H_4 rings. Additionally, the infrared intensities are reported for all five MC_4H_4 rings. The two most intense vibrations involve C–H wagging and ring deformation for each structure. These vibrations are expected to be observable by experiment.

Given that the second (after Sr) least viable Mg complex is the one recently synthesized and isolated, the other group IIA analogues are expected to be confirmed by future synthetic work. Our investigations into the electronic structure of alkaline-earth metallacyclopentadienes will thus prove beneficial to the continuing experimental and theoretical characterization of these compounds.

CHAPTER 3

The Al + CO_2 Reaction Potential Energy Surface*

*Sun, Z., Moore, K. B., and Schaefer, H. F., *J. Chem. Phys.* 2017, 147, 171101. Reprinted with permission from American Institute of Physics.

3.1 Abstract

Based on their highly sophisticated crossed-beam experimental studies of the Al + CO_2 → AlO + CO reaction, Honma and Hirata have directly challenged the results of earlier theoretical studies of this system. We report high level theoretical studies of this system. It is shown that, consistent with Honma-Hirata experimental conclusions, the previous theoretical prediction of a substantial barrier height for this reaction was incorrect. However, for the structures of the possible intermediates, in agreement with the 1992 theoretical study of Sakai, we find striking disagreement with the experimental conclusion that the O-C-O moiety is nearly linear. The energies of the three entrance channel intermediates lie 14.4, 15.2, and 16.4 kcal mol^{-1} below separated Al + CO_2.

3.2 Introduction

Recently this journal published a special issue, entitled "Developments and Applications of Velocity Mapped Imaging Techniques." The third paper therein, by Honma and Hirata[99] is titled "Reaction Dynamics of Al + CO_2 → AlO + CO Studied by a Crossed-Beam Velocity Map Imaging Technique." In addition to establishing the validity of their advanced experimental method, Honma and Hirata made some bold statements concerning previous theoretical studies[100, 101] of the Al + CO_2 reaction.

There have been several earlier experimental studies[102-105] of the Al + CO_2 reaction, but none with such sophistication and forceful conclusions as that of Honma and Hirata. Further, Manceron and coworkers[106] have observed vibrational features of an $AlCO_2$ adduct in argon matrices. Howard and coworkers[107] have reported an EPR study of Al in a CO_2 matrix at 77 K. Brock and Duncan[108] examined the threshold photodissociation of

$AlCO_2$. Finally, in 2015 Thomas and coworkers[109] reported the infrared spectroscopy of the Al-CO_2 complexes in helium nanodroplets. Previous theoretical studies,[100, 101, 110, 111] have predicted four main structures of $AlCO_2$ intermediates (shown in Figure 3.1).

In their abstract, Honma and Hirata[99] state "these results suggested that the reaction proceeds via a short-lived intermediate in which the O–C–O keeps a nearly linear structure". Approaching the end of their paper, Honma and Hirata note that the previous theoretical research predicted transition states between the $AlCO_2$ intermediates and products AlO + CO with high barriers. Honma and Hirata state that "the presence of such high barriers is not consistent with the (experimental) excitation function in which the threshold value is similar to the endothermicity."[99] Honma and Hirata conclude that "the structures of the transition states proposed by the *ab initio* calculations have bent O–C–O angles. The [theoretical] high exit barrier and bent O–C–O structure likely provide significant excitation of the CO rotation, which is not consistent with the present [experimental] result."

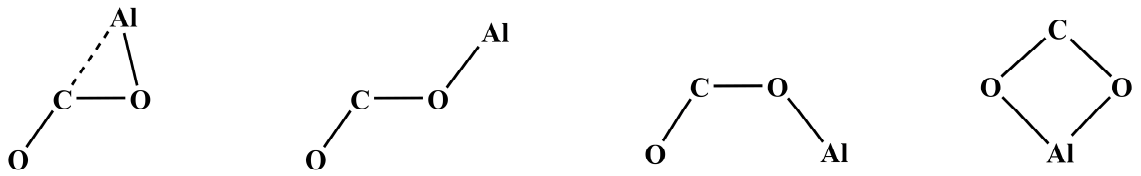

***trans*-$AlCO_2$-1** ***trans*-$AlCO_2$-2** ***cis*-$AlCO_2$** ***sym*-$AlCO_2$**

Figure 3.1: Structures of four main $AlCO_2$ intermediates reported in literatures.

3.3 Computational Methods

In light of such a glaring disagreement between theory and experiment, new theoretical studies are called for. We report here coupled cluster [CCSD(T)] computations[9] with Dunning's correlation consistent basis sets [cc-pV(Q+d)Z].[52, 112, 113] Here the (+d) notation refers to the fact that basis set for aluminum has been augmented with an additional set of tight d basis functions[113]. Intrinsic reaction coordinate (IRC) computations were performed at the B3LYP/cc-pV(T+d)Z level of theory to connect the equilibrium geometries and transition states. Restricted Hartree-Fock reference wave functions (ROHF or RHF) were used for all coupled cluster computations. We affirmed the single-reference character (see SI) of the $AlCO_2$ wavefunctions with a large (13e, 13o) CASSCF space (C and O: all 2*p* orbitals; Al: 3*s* and 3*p* orbitals). Optimizations followed by frequency computations, relaxed scans, and IRC analyses were performed using CFOUR 1.0,[57] MOLPRO 2010.1,[64, 65] and GAMESS 2014 (R1),[91, 114] respectively.

3.4 Results and Discussion

Many of our predictions for the Al + CO_2 → AlO + CO reaction are reported in Figure 3.2. The most important result there is the barrier between the *trans*-$AlCO_2$-1 intermediate and the product AlO ($^2\Sigma^+$) + CO. This corresponds to the lowest energy pathway we found between Al + CO_2 and AlO + CO. The transition state TS-*diss*-1 lies 4.2 kcal mol^{-1} above separated Al + CO_2, and 0.8 kcal mol^{-1} below the products of AlO + CO. TS-*diss*-1 thus lies below the endothermicity of the overall Al + CO_2 → AlO + CO reaction, consistent with the experimental conclusion of Honma and Hirata. The reaction of Al (^{2}P) + CO_2 (X, $^1\Sigma_g^+$) → AlO (X, $^2\Sigma^+$) + CO (X, $^1\Sigma^+$) is found to be endothermic by

5.0 kcal mol^{-1}, which is in good agreement with the best experiment enthalpy (ΔH^0_r = 4.8 kcal mol^{-1}),[115] as well as the threshold collision energy (0.19 eV or 4.4 kcal mol^{-1}) reported by Costes *et al*. for this reaction.[103]

We reluctantly disagree with the previous theoretical study of Sakai,[100] who predicted (see Figure 3.6 in reference 81) this transition state to lie 19 kcal mol^{-1} above Al + CO_2. Such a barrier is insurmountable at the 12.6 ± 2.8 and 6.7 ± 1.6 kcal mol^{-1} collision energies used in the experiments of Honma and Hirata. Our computed TS-*diss*-1 barrier lies only 4.2 kcal mol^{-1} above Al + CO_2 and should thus be readily accessible in the experiment, as this barrier lies below the products AlO + CO. We also assert the feasibility of a second pathway: *trans*-$AlCO_2$-1 can readily convert into *trans*-$AlCO_2$-2, which may then dissociate via the transition state TS-*diss*-2 lying 13.5 kcal mol^{-1} above Al + CO_2. However, this second pathway must not be accessible to the energies of the Honma-Hirata experiments.

The other major issue raised by the experiments of Honma and Hirata[99] concerns the structure of the intermediate and the transition state. They insist that the O-C-O moiety at both the OCOAl intermediate and transition state is nearly linear because of the low CO rotation energies. Our predicted O-C-O angle lowest-lying accessible dissociation transition states (TS-*diss*-1 in Figure 3.2) is 117.5°, far from linear. Here our prediction aligns with the 120° angle predicted by Sakai[100] in 1992. The 116.3° O-C-O angle in TS-*diss*-2 is very similar. It seems clear to us that something is missing in the experimental assignment of the transition state geometries.

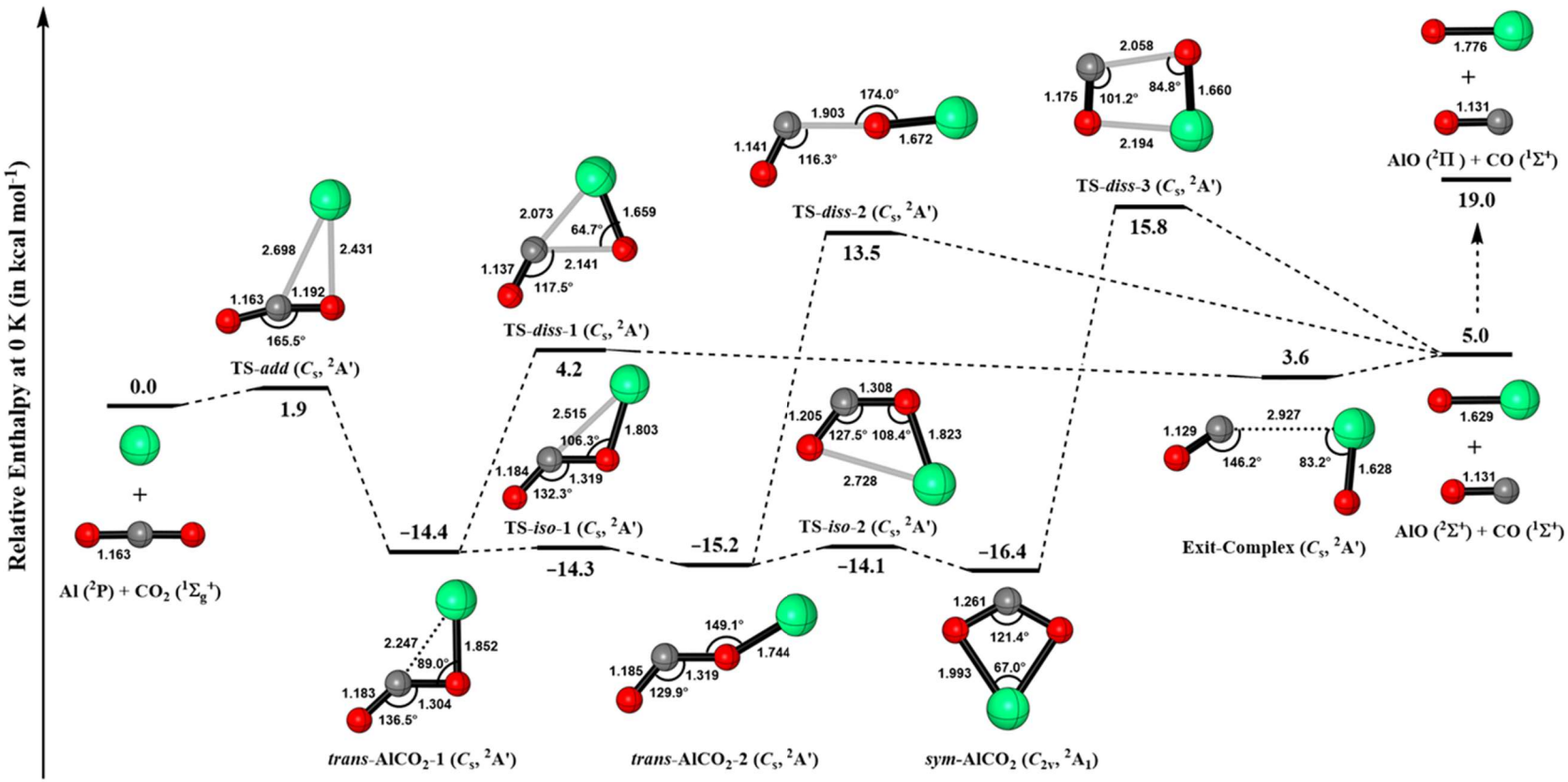

Figure 3.2: Potential energy surface for the Al (^{2}P) + CO_2 ($^1\Sigma_g^+$) → AlO ($^2\Sigma^+$) + CO ($^1\Sigma^+$) reaction at the CCSD(T)/cc-pV(Q+d)Z level of theory.

However, it might be that the OCO bending potential is very flat, making the averaged OCO angle effectively 180°. Pursuing this possibility, Figure 3.3 shows a one-dimensional relaxed scan of the OCO bond angle from its value in *trans*-$AlCO_2$-1 (135°) to linearity. The CCSD(T)/cc-pV(Q+d)Z scan indicates that it takes about 10-15 kcal mol^{-1} to bend the OCO moiety of this $AlCO_2$ intermediate to linearity. This value is much lower than the energy (~35 kcal mol^{-1}, at the same level of theory) required to distort an isolated linear CO_2 molecule to a bent structure (135°).

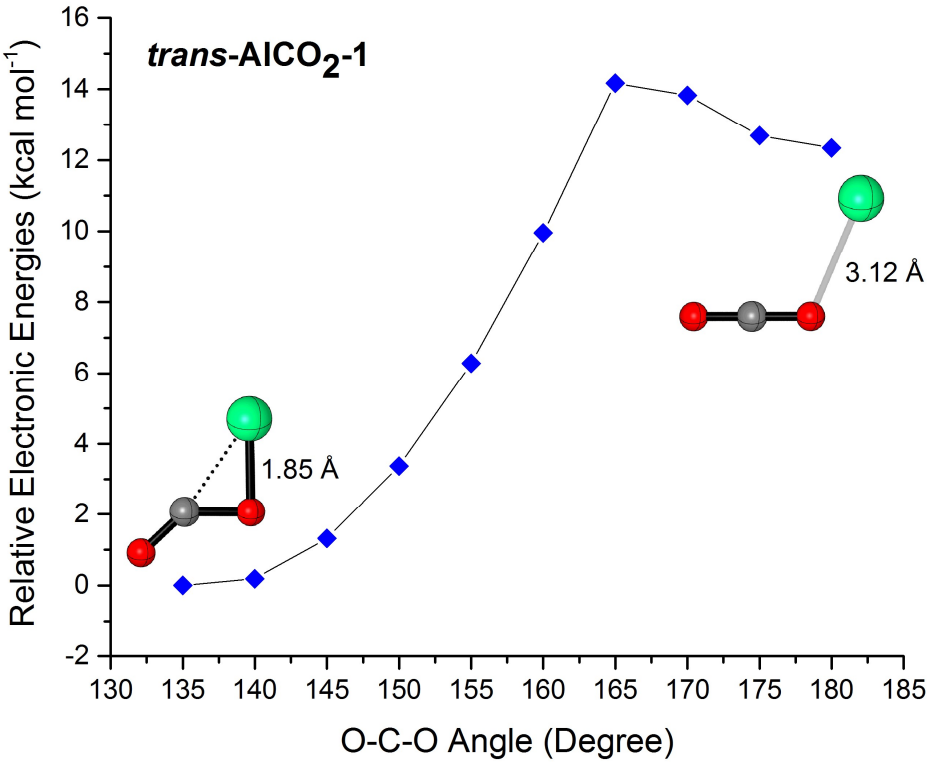

Figure 3.3: Relaxed scan of the O-C-O angle of *trans*-$AlCO_2$-1 at the CCSD(T)/cc-pV(Q+d)Z level of theory (the cusp indicates where the structure start falling apart into relevant fragments).

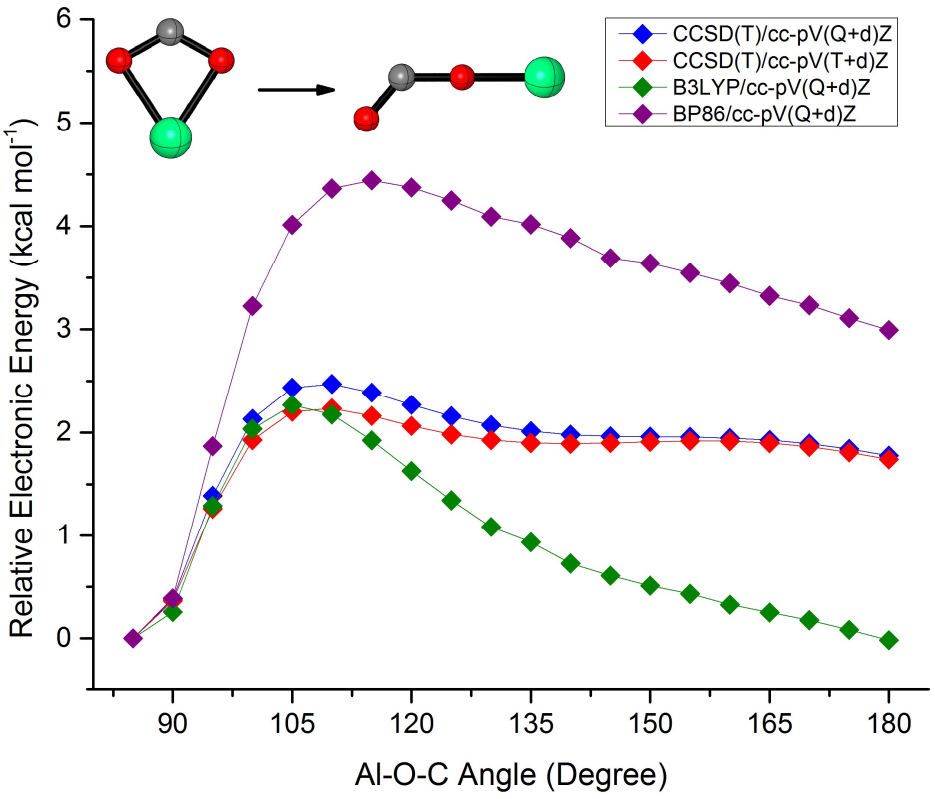

Figure 3.4: Relaxed scan of the Al-O-C angle of *sym*-$AlCO_2$. Note that these potential energy curves do not indicate the presence of a *cis*-$AlCO_2$ minimum along the reaction pathway.

We note that the we have lowered the TS-*diss*-1 barrier such that it now lies only 0.6 kcal mol^{-1} above the Exit-Complex and 0.8 kcal mol^{-1} below AlO + CO. This is another substantial difference with the predictions of Sakai,[100] who placed the TS-*diss*-1 transition state 13 kcal mol^{-1} above AlO + CO. The small difference between TS-*diss*-1 and AlO + CO predicted in this study implies that there will be little energy available to be distributed into rotational states of CO, in alignment with the observations of Honma and Hirata.[99] The transition state for Al + CO_2 addition (TS-*add* in Figure 3.2) does have a nearly linear O-C-O angle of 165.5°. However, the entrance-channel reaction

coordinates of TS-*add* evidently differ from the exit-channel reaction coordinates of TS-*diss*-1 and Exit-Complex.

In addition, although some previous theoretical studies[100, 110] suggested a *cis*-$AlCO_2$ conformer (see Figure 3.1 and SI), this structure was not located with the CCSD(T)/cc-pV(Q+d)Z method. The reasoning for its absence was elucidated using a relaxed scan of the Al-O-C angle of *sym*-$AlCO_2$ provided in Figure 3.4. Figure 3.4 shows a very flat potential surface with almost no energy change in a wide range of about 135-165° with the CCSD(T) method. While the B3LYP and BP86 methods fail to reproduce such a flat surface region, they similarly do not validate the presence of any significantly long-lived *cis*-$AlCO_2$ structure.

CHAPTER 4

Alkali-Metal Trihalides: MX_3 (X = Cl, Br, and I)*

*Sun, Z., Moore, K. B., Hill, J. G., Peterson, K. A., Schaefer, H. F., and Hoffmann, R. J., *J. Phys. Chem. B.* 2018, 122, 3339. Reprinted with permission from the publisher, Copyright (2018) American Chemical Society.

4.1 Abstract

The alkali metal trihalides MX_3 (M = Li, Na, K, Rb, and Cs; X = Cl, Br, and I) are systematically studied using coupled-cluster methods. Benchmarks using CCSD(T) against diatomic experimental results suggest satisfactory performance for the weighted core-valence basis sets (new basis sets for K, Rb, and Cs) selected for predicting reliable structures and harmonic vibrational frequencies. An isomer search using the B3LYP functional yields a planar, yet asymmetric T-shaped C_s structure as the global minimum for all MX_3 species. Much higher level CCSD(T) computations show a moderate to strong distortion of the X_3^- anion by the M^+ cation in the respective equilibrium geometries. Most obviously, for $LiCl_3$ the two Cl-Cl distances are separated by 0.786 Å. Even for CsI_3, the structure least distorted from the $M^+X_3^-$ model, the two I-I distances differ by 0.243 Å. It does not take much energy to distort the parent anions along an antisymmetric stretch, so this is no surprise. The normal modes of vibration of the MX_3 molecules are in better agreement with matrix isolation experiments than previous calculations. And these normal modes are revealing -- instead of the well-established antisymmetric and symmetric stretches of the "free" X_3^- anions, relatively localized and mutually-perturbed X-X and M-X stretches are calculated. The suggestion emerges that the MX_3 system may be alternatively described as an $MX\text{-}X_2$ complex, rather than the $M^+X_3^-$ ion pair. This perspective is supported by bonding analyses showing low electron densities at the bond critical points and natural bond orders between the MX and X_2 moieties. The thermochemistry of fragmentations of MX_3 to $MX + X_2$ vs. $M^+ + X_3^-$ also supports the alternative viewpoint of the bonding in this class of molecules.

4.2 Introduction

There are only limited reports on the fundamental properties of alkali metal trihalides, MX_3 (M = Li, Na, K, Rb, Cs and X = F, Cl, Br, I). Among these, the four experimental papers by Ault, Andrews, and coworkers, of these halides in a noble gas matrix at low temperatures are particularly important.[116-119]

All previous theoretical studies of MX_3 virtually focused on the X_3^- properties and assumed the validity of an $M^+X_3^-$ ion pair model (M = Li, Na, K, Rb, and Cs).[116-119] The X_3^- anions have been considered as more or less "isolated", but perturbed by the M^+ cations. A recent theoretical study of the isolated halogen clusters X_3^- by Dixon and coworkers[120] is relevant to this situation. Early in the course of the present research we realized that Dixon's computed harmonic vibrational frequencies (X-X-X symmetric and antisymmetric stretches) for the "free" Cl_3^- do not show satisfactory agreement with the IR/Raman frequencies of MCl_3 (M = Li, Na, K, Rb, and Cs) from the argon matrix experiments performed by Ault and Andrews.[118] Specifically, we note significant differences (up to 114 cm^{-1}, ~30%) between the theoretical X_3^- and experimental MX_3 vibrational frequencies. It is thus uncertain if quantitative comparisons can be made between MX_3 and X_3^-. This leads to the question: is the perturbation due to an alkali cation strong enough to substantially change the electronic structures of the X_3^- and lead to significant modifications of these anions, in terms of structures, vibrational frequencies, and bonding?

The structures and frequencies of some MX_3 species in the solid state are known,[121, 122] providing indications that the X_3^- moiety could be substantially altered by the presence of M^+. Instead of the well-established symmetric and antisymmetric stretches[118,

[120] for the "free" X_3^- anions, new modes with significant metal displacements may be involved in the MX_3 vibrations. Moreover, large red-shifts (7 – 11%, about 20 – 60 cm^{-1}, see Table S1 in the SI) from gas phase to argon matrices are highlighted by Jacox[123] for the ground state vibrational fundamentals of diatomic alkali metal halides (MX, M = Li, Na, K, Rb, Cs and X = F, Cl, Br, I). Similar red-shifts can be also observed for the small MCl species involved in the experimental Ault and Andrews study of MCl_3 in argon (see Table S1 in SI).[118] If such red-shifts carry over to the MX_3 species, it would impose challenges to achieving good agreement for the vibrational frequencies between gas-phase theoretical computations[120] and the argon matrix experiments.[116-119] And the solid state compounds are bound to differ as well.

The solid state and noble gas matrix perturbations we just mentioned are indicative of a more general truth: Even if we limit ourselves to an MX_3 stoichiometry, with M an alkali metal, the richness of experimental chemistry provides us with a good number of realizations of this formula. These include M^+ and X_3^- noninteracting in the gas phase, MX_3 molecules in a collisionless molecular beam, MX_3 in a noble gas matrix, in solvents of varying polarity, in solids, at surfaces and interfaces. This is hardly an exhaustive list of chemical and physical settings. Each situation will have a different (slightly, significantly) vibrational spectrum for MX_3. And an associated temperature. The studies we present here are, strictly speaking, for isolated MX_3 molecules, at $T \rightarrow 0$ K.

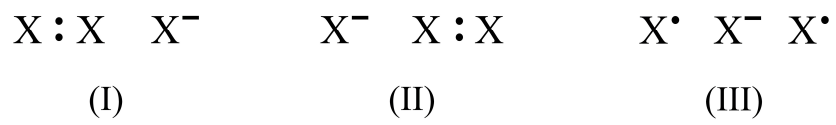

(I) (II) (III)

Scheme 4.1: General bonding types proposed for the 4-electron 3-center hypervalent X_3^- (bonding types I and II for Cl_3^-, Br_3^-, and I_3^-; types I, II, and III for F_3^-) systems.

For the purpose of comparison, let us review the studies of "free" trihalide anions (X_3^-, X = F, Cl, Br, and I). These have been widely explored by both experiment and theory, in the gas phase,[124, 125] solution,[126, 127] and solid state.[128, 129] Those species have been well characterized by IR and Raman spectra,[118, 121, 130-132] and some gas phase thermochemistry of the X_3^- species has been reported.[124, 125, 133, 134] In regard to previous theoretical research, a significant focus has been the interpretation of X_3^- electronic structure and bonding. Basically, all X_3^- species have been described as either (1) a 4-electron 3-center (4e-3c)[135-139] hypervalent bonding system using the Rundle–Pimentel model,[140, 141] or (2) a donor-acceptor interacting system between two closed-shell fragments X_2 and X^-, (bonding types I and II in Scheme 4.1). Insights from molecular orbital (MO) theory are particular relevant in this regard.[135, 136] Hiberty and coworkers[137, 138] employed valence-bond theory to propose another three-electron bonding type (bonding type III in Scheme 4.1) as an important contributor to the electronic structure of F_3^-. This special bonding character of F_3^- has been used to discuss its exceptional multireference[142] and symmetry-breaking[143] challenges, as well as its peculiar preference of the energetically disfavored dissociation channel into F_2^- and F• at high collision energies.[133]

Direct theoretical studies of MX_3 species have been generally limited to the fluoride systems.[144-146] The structures, vibrational frequencies, and dissociation energies of MF_3 (M = Na, K, Rb, and Cs) were systematically studied by Tozer and Sosa[144] as early as 1997 using Hartree-Fock, MP2, QCISD, BLYP, and B3LYP methods. The results were found to be heavily dependent on the identity of the metals, as well as the theoretical methods applied. The method-dependence emerged in locating the true minima and corresponding vibrational frequencies, with only the B3LYP functional predicting the metal-dependent minima (Na: C_s isomer; K, Rb, and Cs: C_{2v} isomer, see Figure 4.1) inferred from the IR/Raman spectra by Andrews and coworkers.[147, 148] The C_{2v} isomers for KF_3 and CsF_3 were more recently (2015) studied using CCSD(T)/def2-TZVPP computations by Riedel and coworkers.[146] The MF_3 (M = Li, Na, and K) species were also studied in 2015 using the CCSD(T)/6-311+G(3df) method by Getmanskii *et al*.[145]

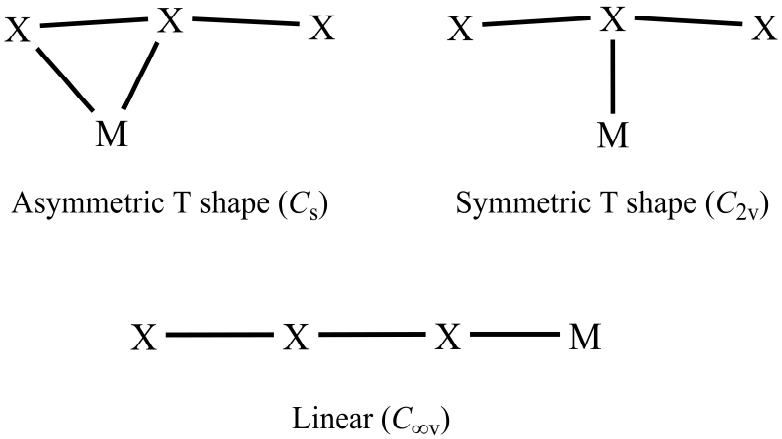

Figure 4.1: Structures of MF_3 (M = Li, Na, K, Rb, and Cs) reported in the literature.[144-146]

Minima for all three isomers sketched in Figure 4.1 were located for all three fluoride species, except that the asymmetric T-shaped minimum was not found for KF_3. The global minima for LiF_3 and NaF_3 were found to be the asymmetric and symmetric T-shaped structures, respectively. However, a tiny 0.16 kcal mol^{-1} (ZPVE corrected) energy difference between the two T-shaped NaF_3 structures introduces additional uncertainties. The general preference of the C_{2v} global minimum for MF_3 could originate from the special electronic structure of F_3^- discussed above (see Scheme 4.1). Since the heavier X_3^- anions do not possess this unique F_3^- electronic structure, it is unclear if such structural preferences also occur for other alkali metal trihalides, MX_3 (X = Cl, Br, and I).

There are limited theoretical and experimental results for the heavier halides MX_3 (X = Cl, Br, and I), and it would be beneficial to probe the latter species with rigorous computations. The present study does this, and aims to offer some answers to the following questions:

(1) Why is the agreement between theoretical[120] X_3^- and experimental[118] MX_3 vibrational frequencies relatively unsatisfactory?

(2) Could the metal-dependent global minima found[144, 145] for MF_3 also occur for MCl_3, MBr_3, and MI_3?

(3) What are the differences between X_3^- and MX_3 in terms of structures, vibrational modes and frequencies, bonding characters, and thermochemistry?

(4) Finally, the title question, not anticipated, but one that arose quite naturally as we progressed: should the alkali metal trihalides be described as ion pairs between M^+ and X_3^- or as complexes between MX and X_2?

4.3 Computational Methods

An isomer search for the MX_3 global minima was conducted by optimizing various prospective structures using the B3LYP3 functional[58, 149, 150] implemented in MOLPRO 2010.1.[64, 65] This particular version of the B3LYP functional utilizes the standard VWN3 local correlation energy parameters.[149] For these computations, the SCF energies and densities were both converged to 10^{-10}, and the RMS force was converged to 10^{-8} Hartree $Bohr^{-1}$. Stationary points obtained from these optimizations were classified by their harmonic vibrational frequencies, obtained via finite differences of analytic energy gradients. The following standard correlation consistent valence basis sets (AVTZ for simplicity) were used in the DFT computations:

Li, Na: cc-pVTZ[151]

K, Rb, Cs: cc-pVTZ-PP[152]

Cl: aug-cc-pVTZ[112]

Br, I: aug-cc-pVTZ-PP[153]

The equilibrium geometries, harmonic vibrational frequencies, and dissociation energies (D_0) of MX_3 global minima were subsequently obtained (with new and different core-correlated basis sets) using coupled cluster theory with single, double, and perturbative triple excitations [CCSD(T)],[10-13] as implemented in CFOUR 2.0.[57] The restricted Hartree-Fock (RHF) method was used throughout, as all the species of interest are closed-shell. For all CCSD(T) computations, the SCF densities, CC amplitudes, and Lambda coefficients are converged to 10^{-10}. The RMS force of the geometries was converged to 10^{-8} Hartree $Bohr^{-1}$. The gradients were obtained via analytic first derivatives of the CCSD(T) energy, and the frequencies were obtained by finite

differences of these gradients. Listed below is a new group of weighted core-valence basis sets (AWCVTZ for simplicity) that was used for the CCSD(T) computations:

Li, Na: cc-pwCVTZ[151]

K, Rb, Cs: cc-pwCVTZ-PP[152]

Cl: aug-cc-pwCVTZ[112, 154]

Br, I: aug-cc-pwCVTZ-PP[155, 156]

These are correlation consistent (cc), polarized (p), weighted core-valence (wCV), triple-zeta (TZ) basis sets. Each halogen atom (Cl, Br, I) basis set is augmented with additional diffuse basis functions to describe potential anionic character. All electrons of the Li, Na, and Cl atoms were correlated in the CCSD(T) computations. For K, Rb, Cs, Br, and I, deep inner electrons were treated by effective core potentials (described below). This method was chosen because the traditional frozen-core approximation yielded several errors in the optimized structures and harmonic vibrational frequencies for certain species (e.g. KCl_3). These issues appear to stem from systems having correlated and uncorrelated molecular orbitals with nearly degenerate energies. Further wavefunction diagnostics provided in the SI demonstrate that our chosen single-reference CCSD(T) methods should be reliable. All energy and property computations were performed using the CCSD(T)/AWCVTZ structures.

For both the B3LYP and CCSD(T) computations, we employ the multi-electron fit, fully relativistic Köln/Stuttgart effective core-potentials (ECPs) to model the inner core electrons of the atoms below the 3rd-row [ECP10MDF (K and Br): 10 electrons ($1s^2 2s^2 2p^6$); ECP28MDF (Rb and I): 28 electrons ($1s^2 2s^2 2p^6 3s^2 3p^6 3d^{10}$); and ECP46MDF (Cs): 46 electrons ($1s^2 2s^2 2p^6 3s^2 3p^6 4s^2 3d^{10} 4p^6 4d^{10}$)].[157] For the atoms treated by an ECP,

the corresponding -PP basis sets are used. Since the cc-pVTZ-PP and cc-pwCVTZ-PP basis sets for K, Rb, and Cs are not yet available in the literature, we have provided them in the Supporting Information (SI). These basis sets are specifically matched to the ECPs mentioned above and have the following number of primitives and contracted functions at the cc-pVTZ-PP level: K, (11s10p6d1f)/[5s4p3d1f]; Rb, (11s9p5d1f)/[5s4p3d1f]; Cs, (11s9p6d4f)/[5s4p3d2f]. In all cases linear dependency issues were avoided by constraining the optimizations such that the ratio between successive functions in a given angular symmetry was greater than or equal to 1.6. The problem of correlating functions in ECP-based calculations recovering less correlation energy than in all-electron calculations[158, 159] was circumvented by uncontracting an extra s-type correlating function, as in previous work.[159, 160] The cc-pwCVTZ-PP basis sets for these elements add 2s2p2d1f sets of functions that have been optimized using the well-established strategy for weighted core-valence basis sets.[154] To keep discussions throughout the main text succinct, we will refer to the mixture of these basis sets for the B3LYP and CCSD(T) simply as AVTZ and AWCVTZ, respectively.

A bonding analysis of the optimized MX_3 species was performed using Weinhold natural bond orbital (NBO) theory[161] and the Bader quantum theory of atoms-in-molecules (QTAIM).[162] Intermolecular hyperconjugation was quantified with the second-order energy for delocalizing electrons from a donor orbital (L) to an acceptor orbital (NL):[72]

$$E(2) = q_L \frac{F(L,NL)^2}{\varepsilon_{NL} - \varepsilon_L} \tag{4.1}$$

where $F(L, NL)$ is the NBO Fock matrix element, and q_L and ε_L are the occupancy and energy of orbital L, respectively. Resonance structures from natural resonance theory (NRT)[163-165] were obtained to characterize the overall electronic structure, and types of bonding types in MX_3. We expand this picture by discussing the covalent and ionic contributions to the natural bond order. QTAIM was used to locate the bond critical points to assess the electron density occurring between each atom. The above described NBO (HF/AWCVTZ) and QTAIM (B3LYP/AVTZ) analyses were performed using NBO 6.0[72] and AIMAll 16.01.09.[71]

4.4 Results and Discussion

A systematic study of MX_3 (M = Li, Na, K, Rb, and Cs; X = Cl, Br, and I) was performed using density functional and coupled-cluster methods. In view of possible metal-dependence indicated by theoretical studies of MF_3 (M = Li, Na, K, Rb, and Cs),[144-146] several structures were considered (Figure 4.2) using the B3LYP functional to locate possible local minima. This was then followed by high-level coupled-cluster computations [CCSD(T) with the weighted core-valence basis sets, see Methods]. The equilibrium geometries (Table 4.2 and Figure 4.3), vibrational modes and frequencies (Tables 4.3-4.6 and Figure 4.5), bond analysis (Tables 4.7-4.8), thermochemistry (Table 4.9), and other relevant results for each species considered are reported and discussed.

4.4.1 Performance of the new weighted core-valence basis sets

We wish to assess the uncertainty of the computed geometries and vibrational frequencies for the MX_3 species. In addition, the weighted core-valence basis sets for the alkali

metals (K, Rb, and Cs, see Methods and SI) are newly developed, and no assessment of their accuracy is currently available. Since there is little experimental information on the MX_3 species, the relevant diatomic species MX and X_2 (M = Li, Na, K, Rb, Cs and X = Cl, Br, I) are selected as a test set. Within the NIST database,[166] there are well-established gas phase experimental values for the equilibrium bond distances and harmonic vibrational frequencies of MX and X_2. Within this test set, 15 ionic and 3 covalent bonds are included, and we benchmark our chosen theoretical methods against the experimental values of these species in Table 4.1.

For the equilibrium bond length, the overall mean absolute error (MAE) and mean absolute percent error (MAPE) was found to be 0.018 Å and 0.7%, respectively. For each of the three metal halides series (MCl, MBr, and MI), the theoretical bond lengths are all slightly longer than the experimental values, with an increasing trend from LiX to CsX. The largest differences between theory and experiment occur for CsX, with percent errors being 1.1%, 1.0%, and 1.0% for CsCl, CsBr, and CsI, respectively. For the X_2 (X = Cl, Br, and I), a decreasing trend in positive deviations (Cl_2: 0.8%, Br_2: 0.6%, and I_2: 0.3%) can be noticed.

For the harmonic vibrational frequencies, the overall MAPE was found to be 1.7%. From Table 4.1, most deviations are negative and within 2.0%. However, RbCl, KBr, and I_2 are exceptions with positive deviations, and NaBr is the species with the highest deviation beyond 2.0% (-3.0%). No obvious trend in percent errors can be found for the MCl and MBr series, however, the MI series shows an increasing trend from LiI to RbI, with an exception that the percent error for CsI drops below RbI. Consistent with the

situation for bond lengths, the percent errors of the X_2 species decrease from Cl_2 to I_2 (Cl_2: -2.1%, Br_2: -1.8%, and I_2: 0.9%).

Table 4.1: Benchmark of the CCSD(T)/AWCVTZ equilibrium bond lengths (in Å) and harmonic vibrational frequencies (in cm^{-1}) of MX and X_2 (M = Li, Na, K, Rb, and Cs; X = Cl, Br, and I) molecules against experimental values from the NIST tables.

	Equilibrium Bond Lengths				Harmonic Vibrational Frequencies		
Species	Computed	NIST	Deviation	Percent Error	Computed	NIST	Percent Error
LiCl	2.029	2.021	0.008	0.4%	635	643	-1.2%
NaCl	2.373	2.361	0.013	0.6%	359	366	-1.9%
KCl	2.683	2.667	0.017	0.6%	276	281	-1.8%
RbCl	2.805	2.787	0.019	0.7%	231	228	1.3%
CsCl	2.939	2.906	0.033	1.1%	210	214	-1.9%
LiBr	2.180	2.170	0.009	0.4%	553	563	-1.8%
NaBr	2.517	2.502	0.015	0.6%	293	302	-3.0%
KBr	2.838	2.821	0.018	0.6%	216	213	1.4%
RbBr	2.964	2.945	0.020	0.7%	167	169	-1.2%
CsBr	3.104	3.072	0.032	1.0%	147	150	-2.0%
LiI	2.400	2.392	0.008	0.3%	493	498	-1.0%
NaI	2.729	2.711	0.018	0.7%	254	258	-1.6%
KI	3.066	3.048	0.019	0.6%	184	187	-1.6%
RbI	3.199	3.177	0.023	0.7%	136	139	-2.2%
CsI	3.348	3.315	0.033	1.0%	117	119	-1.7%
Cl_2	2.003	1.987	0.016	0.8%	548	560	-2.1%
Br_2	2.295	2.281	0.014	0.6%	319	325	-1.8%
I_2	2.673	2.666	0.007	0.3%	217	215	0.9%
		Mean:	0.018	0.7%		Mean:	1.7%

In summary, the CCSD(T) method with the selected weighted core-valence basis sets predicts reliable structures and harmonic frequencies for the relevant diatomic species MX and X_2 (M = Li, Na, K, Rb, Cs and X = Cl, Br, I). Accordingly, the accuracy of our computed equilibrium bond lengths and harmonic vibrational frequencies of alkali metal trihalides MX_3 should be satisfactory for assessing the experimental conclusions of Ault, Andrews, and coworkers.[118]

4.4.2 Possible MX_3 structures

Previous theoretical [144-146] and experimental studies[147, 148] have noticed that the identity of the metal (M) in the metal fluoride systems MF_3 (M = Li, Na, K, Rb, and Cs) dictates the structure of the global minimum. To investigate whether a similar metal-dependence exists for MX_3 (M = Li, Na, K, Rb, Cs and X = Cl, Br, I) species, several structures were first considered using the B3LYP/AVTZ method. The B3LYP functional was selected due to its reliable performance in the theoretical fluoride study of Tozer and Sosa[144] in reproducing Ault and Andrews's MF_3 experimental results.[147, 148] The isomers explored for the MX_3 (M = Li, Na, K and X = Cl, Br, I) are shown in Figure 4.2. The first three structures (also shown in Figure 4.1) were chosen because they have been previously identified as minimum-energy structures on the MF_3 potential energy surface.[144-146] Five additional structures (4 – 8 in Figure 4.2) were selected as they represent alternate symmetries, which are constrained during optimization. Also the coplanarity of all four atoms implicit in structure **1** and **2** was relaxed, effectively allowing **1** to be C_1 and **2** C_s in symmetry.

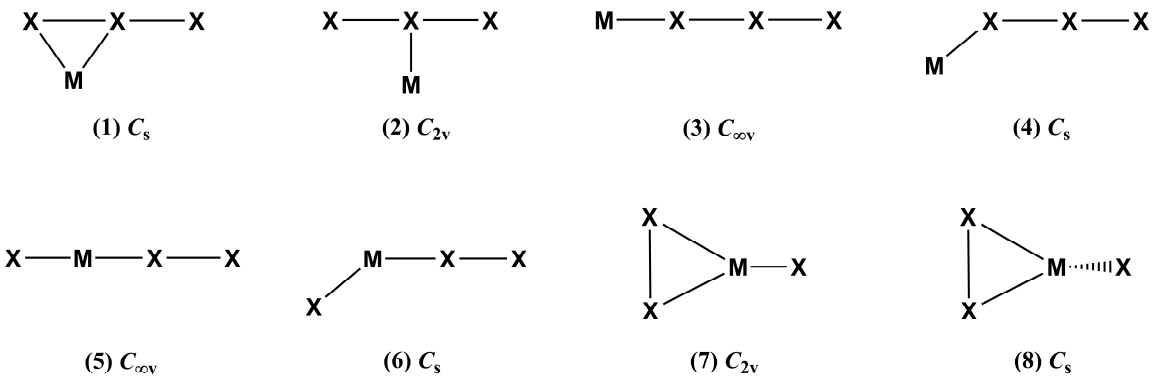

Figure 4.2: Possible stationary point structures explored for the MX_3 (M = Li, Na, K and X = Cl, Br, I) systems using B3LYP/AVTZ method.

In contrast to the structural variations noticed in the case of the fluoride species MF_3,[144, 145] results for the other halides, the subject of this paper, are generally consistent for Li, Na, and K. For all MX_3 species, structures **1**, **2**, and **3** correspond to minima, transition states, and second-order saddle points, respectively. The only other possible minimum was found to be the structure **7**, although it shows some metal-dependence. The LiX_3 structures **7** were all found to be first-order saddle points with small imaginary frequencies of 43*i*, 34*i*, and 22*i* cm^{-1}, for $LiCl_3$, $LiBr_3$, and LiI_3, respectively. Most NaX_3 and KX_3 structures of type **7** were predicted to be minima. However, a tiny imaginary frequency (5*i*) and two small imaginary frequencies (20*i* and 12*i*) were predicted for $NaCl_3$ and KBr_3, respectively. Finer integration grids might predict all real frequencies for these species, but the long inter-fragment distance (2.5 – 3.5 Å) and the small first few frequencies (below 50 cm^{-1}) indicate that the structure **7** is not a strongly bound minimum. Moreover, for all MX_3 species investigated, structure **7** lies 5.9 – 15.2 kcal mol^{-1} above structure **1** at the ZPVE-corrected B3LYP level. Optimizations of structures

4, **6**, and **8** lead to either structure **1** or **7** (see SI). Optimizations of structure **5** separated the MX and X_2 moieties beyond 4.0 Å.

Could structures **1** and **2** be nonplanar (as one sees in the trifluorides)? Optimizations begun in nonplanar geometries returned uniformly to C_s and C_{2v} minima. There were two exceptions: 1. For MCl_3 (M=Na, K, Rb, Cs) a noncoplanar structure derived from **2** was a stationary point that turned out to be a transition state; the large imaginary frequency characterizing this geometry led to a structure **1** geometry. 2. For $CsBr_3$ a nearly planar structure close to C_{2v} (near **2**) was a minimum, with a low frequency ($23cm^{-1}$) mode leading back to structure **1**.

Although the C_s structures are definitely preferred, the question could be asked "By how much?" Some representative numbers for the energy difference between optimized C_s and C_{2v} structures are -11.0 kcal/mol for $LiCl_3$, 1.1 kcal/mol for $CsCl_3$, 10.0 kcal/mol for LiI_3, 1.2 kcal/mol for CsI_3. For Li species, the C_s and C_{2v} structures are clearly separated by ~10 kcal/mol. However, the CsX_3 (X = Cl or I) have C_s and C_{2v} structures nearly degenerate in energy, consistent with their small imaginary frequencies (55*i* and 16*i* for $CsCl_3$ and CsI_3, respectively) in their C_{2v} shape. This is an indication that large alkali metals (such as Cs) tend to have less impact on the X_3^- than the small ones (Li, for instance). We will explore this point further in the following sections.

In summary, the strong metal-dependence reported for the MF_3 (M = Li, Na, K, Rb, and Cs)[144, 145] species does not appear to carry over to the MX_3 (X = Cl, Br, and I) systems. In contrast to the general preference for a C_{2v} global minimum for MF_3, our DFT computations suggest that the asymmetric T-shaped C_s structure (structure **1** in Figure 4.2) is a global minimum for all MX_3 species. This is consistent with the Ault and

Andrews's experimental finding for MCl_3 (M = Li, Na, K, Rb, and Cs).[118] We only focus on the asymmetric T-shaped global minimum for the rest of the discussion.

4.4.3 Equilibrium geometries for MX_3

The labels of atoms and bonds in MX_3 (M = Li, Na, K, Rb, and Cs; X = Cl, Br, and I) are shown in Figure 4.3, and the parameters of all equilibrium geometries are listed in Table 4.2. For comparison, the "free" X_3^- (X = Cl, Br, and I) geometries are also reported.

For the trihalide series seen in Table 4.2, the Cl-Cl bond distance in the "free" Cl_3^- ($D_{\infty h}$) is predicted to be 2.313 Å at the CCSD(T)/aug-cc-pwCVTZ level. This value agrees well with the CCSD(T)/aug-cc-pV(T+d)Z result (2.314 Å) by Dixon and coworkers[120] and the CCSD(T)/aug-cc-pVQZ result (2.313 Å) by Riedel *et al*.[167] The Br-Br bond distance in Br_3^- is predicted to be 2.571 Å at the CCSD(T)/aug-cc-pwCVTZ-PP level. This value is slightly shorter than the Br-Br distance (2.585 Å) computed at the CCSD(T)/aug-cc-pVTZ-PP level by Dixon and coworkers.[120] Both Cl-Cl and Br-Br bond distances are also close to DFT results obtained at the MPWB1K/6-31+G(d) level of theory by Pichierri.[168] The I-I bond distance in "free" I_3^- is predicted to be 2.944 Å at the CCSD(T)/aug-cc-pwCVTZ-PP level. This value is shorter than the I-I distance (2.973 Å) computed with the CCSD(T)/aug-cc-pVTZ-PP method by Dixon and coworkers.[120] However, our distance agrees well with the result (2.945 Å) at the CCSD(T)/aug-cc-pVTZ-PP level (all orbitals are correlated) by Braïda and Hiberty.[138] The difference in bond lengths calculated with ostensibly the same methodology, not to speak of what would be obtained with different levels of calculation, serves in a way to set the theoretical equivalent of an error bar on a calculation.

There are to date limited reports of any type for the MX_3 (X = Cl, Br, and I) structures in the gas phase or in matrices. Hence we are drawn to some solid state results. And here we need to insert an anticipation of what Table 4.2 holds, which can be summarized as a variable asymmetrization of the trihalide moiety of MX_3, in the asymmetric environment the trihalide faces in a C_s geometry.

Such asymmetrization is a sign of the relatively small energy involved in changing the B1 and B2 bond lengths from equality in X_3^- itself, no cation present, along an antisymmetric stretching coordinate. Experimentally, the evidence for this is the beautiful Bürgi and Dunitz diagram (a plot of B1 vs B2) for all the triiodide structures in the Cambridge Structural Database (CSD[169]) in 2003, by Svensson and Kloo.[170] We have regenerated this plot in Figure 4.4, The impetus for a structure to move from the 45˚ line (B1=B2) is, of course, the asymmetry of the counter-cation in the structure, or the crystal packing. Whichever it is, the hyperbola we see is *prima facie* evidence of an energetically easy excursion along a very specific potential energy surface in which B1≠B2. A similar diagram for tribromide structures may be found in Robertson et al.[129]

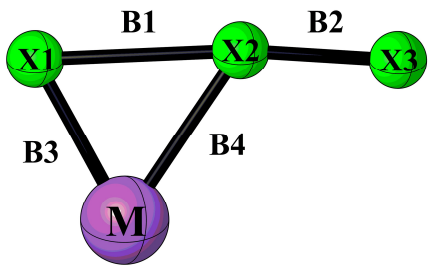

Figure 4.3: Labels of atoms and bonds in MX_3 (M = Li, Na, K, Rb, and Cs; X = Cl, Br, and I) used in Table 4.2.

Table 4.2: Equilibrium geometries (bond lengths in Å and angles in degrees) of MX_3 (M = Li, Na, K, Rb, and Cs; X = Cl, Br and I) minima (see Figure 4.3) optimized using the CCSD(T)/AWCVTZ method. Previously reported values are given in parentheses.

Species	B1 (X1-X2)	B2 (X2-X3)	B3 (M-X1)	B4 (M-X2)	A (X1-X2-X3)	A (X1-M-X2)
Cl_3^-	2.313 (2.314[a], 2.313[b])	2.313 (2.314[a], 2.313[b])	-	-	180.0	-
$LiCl_3$	2.836	2.050	2.079	2.382	169.1	78.6
$NaCl_3$	2.719	2.078	2.440	2.733	174.1	63.1
KCl_3	2.598	2.116	2.786	2.982	174.3	53.4
$RbCl_3$	2.569	2.127	2.925	3.096	174.1	50.4
$CsCl_3$	2.553	2.132	3.084	3.253	174.1	47.4
Br_3^-	2.571 (2.585[a])	2.571 (2.585[a])	-	-	180.0	-
$LiBr_3$	2.879	2.385	2.269	2.463	171.0	74.8
$NaBr_3$	2.817	2.410	2.629	2.809	174.0	62.3
KBr_3	2.741 (2.64[c])	2.441 (2.49[c])	2.989	3.083	173.2	53.6
$RbBr_3$	2.721	2.450	3.137	3.199	172.7	50.9
$CsBr_3$	2.702 (2.698[d])	2.458 (2.440[d])	3.312	3.344	172.0	47.9
I_3^-	2.944 (2.972[a], 2.945[e])	2.944 (2.972[a], 2.945[e])	-	-	180.0	-
LiI_3	3.229	2.769	2.504	2.664	170.2	77.3
NaI_3	3.182	2.790	2.855	3.017	173.4	65.6
KI_3	3.113	2.816	3.226	3.321	172.9	56.8
RbI_3	3.095 (3.051[f])	2.824 (2.833[f])	3.376	3.444	172.4	54.0
CsI_3	3.075 (3.03[g])	2.832 (2.83[g])	3.552	3.589	171.7	51.0

[a] The CCSD(T)/aug-cc-pV(T+d)Z values from ref 120.
[b] The CCSD(T)/aug-cc-pVQZ values from ref 167.
[c] X-ray values of *Pnma* KBr_3 crystal from ref 171.
[d] X-ray values of *Pmnb* $CsBr_3$ crystal from ref 172.
[e] The CCSD(T)/aug-cc-pVTZ-PP values from ref 138.
[f] X-ray values of *Pnma* RbI_3 crystal from ref 173.
[g] X-ray values of CsI_3 crystal from refs 174 and 175.

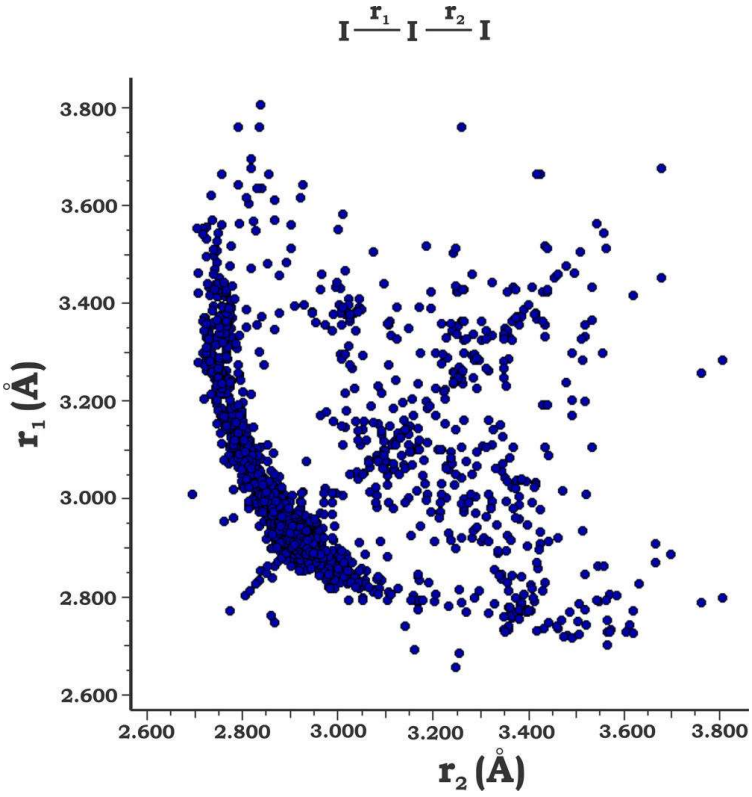

Figure 4.4: A plot of the two distances, r1 and r2 (corresponding to our *B*1 and *B*2) in the triiodide structures in the Cambridge Structural Database. Reprinted from ref 176. Copyright 2013 American Chemical Society.

We can simulate the energetics involved theoretically by fixing 2.67 Å < B1 < 2.94 Å (the limits are its values in I_2 and I_3^-), and allowing B2 to vary. The resulting plot (in the SI) reproduces the hyperbola pretty well, and shows that it takes 4.8 kcal/mol for I_3^- to move from B1 = 2.67 Å, B2 = 3.07 Å to B1 = B2 = 2.94 Å.

Returning to specifically MX_3 structures, with the M of this study, we do find some in the literature. In these, even if the stoichiometry is MX_3, one does not have a molecular crystal of MX_3 entities well-separated from other such molecules; instead there are arrangements of varying complexity of X_3 anions of varying asymmetry, and the M

cations. The structures resolved in previous experimental studies at least in part to give an idea of their complexity.

The structures observed fall into three groups: (1) MX_3 solid state structures; (2) $MX_3 \cdot Z$, where one or more Z molecules accompany the metal halide in the solid state structure; (3) extended structures associated with high pressure environments, often theoretical.

In group 1 we have structures of $CsBr_3$, RbI_3 and CsI_3 (the latter done independently by two groups, and also at -160˚C).[172, 173, 175, 177] In each case, the coordination environment of the trihalide is far from simple – for instance in $CsBr_3$ the tribromide group has no less than 8 different Cs^+ ions coordinated to it, at 3.52-4.02 Å. And that coordination environment is very, very different from that we calculate for our isolated MX_3 molecules. Nevertheless, the observed asymmetries of the trihalides in these structures quite remarkably resemble those calculated by us for isolated molecules. In the crystal structure of $CsBr_3$ in *Pmnb* space group,[172] the experimental Br-Br bond length pair was reported to be 2.698/2.440 Å, which agrees well with the values 2.702/2.458 Å reported in the present research. The I-I bond length pairs in the RbI_3[173] and CsI_3[174, 175] crystal structures were reported to be 3.051/2.833 and 3.04/2.84 Å (some variation among the crystal structures), respectively, and the two sets of values are close to the corresponding 3.095/2.824 and 3.075/2.832 Å obtained at the CCSD(T)/AWCVTZ level in this work. A theoretical study of the CsI_3 crystal finds 3.01/2.90 Å.[178]

The second group – MX_3 associated with other molecules – is a rich one. Here are three examples of many: $KI_3 \cdot H_2O$, $KI \cdot KI_3 \cdot 6$(N-methyacetamide), $Cs_2I_8 = Cs_2 \cdot (I_3)_2 \cdot I_2$.[179-181] Naturally, the triiodide environments are still more complex in these compounds.

Remarkably the triodide in $KI_3 \cdot H_2O$ is nearly symmetrical, I-I 2.925/2.935 Å, the asymmetry calculated by us is 2.816/3.182 Å. The trihalides in Cs_2I_8 are closer to our molecular asymmetry, at 2.84/3.00 Å. One has to draw an imaginary line somewhere in listing compounds in this class, as the structures quickly shade over to the multitudinous class of polyiodides, in which trihalides interact weakly or strongly with iodide ions and I_2 molecules.[170]

The high pressure structures, the third group, are a relatively new phenomenon, one with which one of us (RH) is much involved. Under extreme conditions of elevated pressure new stoichiometries emerge, simply not there at 1 atm. Calculations often precede syntheses in this playground; actual observation of predicted phases is relatively rare. In the two cases we mention, $NaCl_3$ and KCl_3, one actually has seen the compositions in experiment. In the $NaCl_3$ crystal structure (*Pm*3*n* space group) at high pressure (200 GPa),[182] the shortest Cl-Cl and Na-Cl bond distances were recently reported to be 2.06 and 2.30 Å. These two distances are not far from to 2.078 and 2.440 Å (B2 and B3 in Figure 4.3 and Table 4.2) at the CCSD(T)/AWCVTZ level in this work, respectively. The Br-Br bond length pair in KBr_3 was reported in 2017 to be 2.64/2.49 and 2.90/2.51 Å in *Pnma* (4 GPa) and $P\bar{3}c1$ (15 GPa) space groups, respectively.[171] These distances may be compared to our theoretical values 2.741/2.441 Å (Table 4.2) at the CCSD(T)/AWCVTZ level. In general, it may not be fair to compare distances in a calculated compressed crystal with our isolated molecule values a P = 1 atm.

Returning to our computational results, summarized in Table 4.2, in all MX_3 structures, a clear decreasing and increasing trend can be observed in the change of B1 (X1-X2) and B2 (X2-X3) bond lengths from Li to Cs, respectively. In other words, the

bonds B1 and B2 tend to converge at CsX_3 with a distorted structure compared to the "free" X_3^- (Cl-Cl: 2.313 Å; Br-Br: 2.571 Å; I-I: 2.944 Å, Table 4.2), implying a decreasing interaction of M^+ with X_3^-, probably due to the increasing metal-halogen distance from Li^+ to Cs^+. Moreover, the Br_3^- and I_3^- are less distorted than Cl_3^- by the same alkali metal, in terms of the imbalance of bond pair B1/B2 in Table 4.2. Both B3 (X1-M) and B4 (X2-M) keep increasing because of the enlarged atomic size from Li to Cs, and the bond pair B3/B4 distances become more similar from LiX_3 to CsX_3. Particularly, the B3 and B4 distances in $CsBr_3$ and CsI_3 are almost equal with a Δ(B3-B4) of only about 0.03-0.04 Å, whereas it is relatively large for $CsCl_3$ (~ 0.17 Å).

We already mentioned the $MX{\cdot}X_2$ perspective, which emerges in the next section; the similarity of B2 and B3 distances brings to mind still another viewpoint, an organometallic one: it suggests an M^+ ion π-bonding to just one pair of atoms in a trihalide anion.

Most importantly, the internuclear distance between M and atom X3 (Figure 4.3) is always long (mostly beyond 4.0 Å, with the exception of Li-Cl3 being 3.901 Å). Hence no strong interaction between the alkali metal and this particular halogen atom X3 is seen. This is consistent with the observation that the MX_3 (M = Li, Na, K, Rb, Cs and X = Cl, Br, I) species all possess an asymmetric T-shaped C_s equilibrium structure, instead of a symmetric C_{2v} structure (Figure 4.1), such that is seen for most MF_3 species.[144-146] Such a different preference of symmetry between MF_3 and MX_3 is largely dictated by the different electronic structures of the two, which has been discussed in the Introduction (see also Scheme 4.1).

For the angle A(X1-X2-X3) in Table 4.2, a ~6–10º deviation from linear X_3^- is noticed for all MX_3 series. The LiX_3 always possess the most bent A(X1-X2-X3) angle, which is about 10º from linearity and distinct from those of NaX_3 by 3º–5º. The A(X1-X2-X3) angles from NaX_3 to CsX_3 are more consistent, especially for the MCl_3. However, a slightly decreasing trend from Na to Cs can be found for the MBr_3 and MI_3 series. In the Svensson and Kloo review of triiodide structures, their Fig. 10 shows small departures from triiodide linearity in hundreds of such structures. Departures from linearity of ~6–10º are rare; indicating in still another way the strong M-X_3 bonding. In discrete molecules, in addition, the angle A(X1-M-X2) becomes increasingly acute due to the enlarged atomic size from Li to Cs.

In summary, our geometrical parameters show reasonable agreement with available experiments. For all three MX_3 series, the trend in geometrical change indicates a generally decreasing distortion of the X_3^- structure by M^+ from Li^+ to Cs^+. C_s (and not C_{2v}) symmetry is established for all MX_3 (X = Cl, Br, and I). Such preference for C_s symmetry is also reflected in the MX_3 harmonic vibrational modes and frequencies, which are discussed in the following section.

4.4.4 Vibrational modes and frequencies of MX_3

Generally, for the "free" $D_{\infty h}$ X_3^- (X = Cl, Br, and I) anions, the antisymmetric stretch (σ_u) and bend mode (π_u) are both IR-active, while the symmetric stretch (σ_g) is Raman-active, as shown at the top of Figure 4.5. Since the MX_3 experiments necessarily contain countercations, which distort the X_3^- into a lower symmetry, both stretches are expected to have substantial intensity in the IR and Raman spectra.

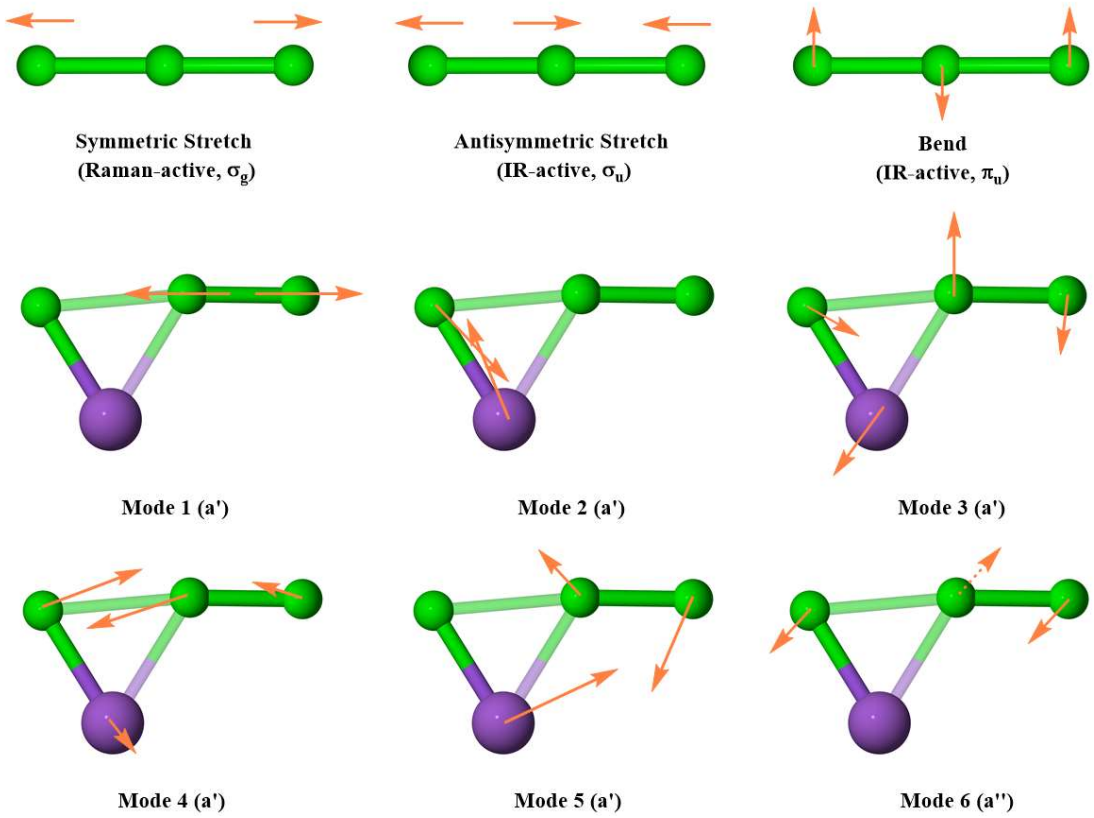

Figure 4.5: Vibrational modes for the $D_{\infty h}$ "free" X_3^- (illustrated for Cl_3^-) and C_s MX_3 (illustrated for KCl_3).

Table 4.3: Harmonic vibrational frequencies (cm^{-1}) and infrared intensities (in parentheses, km mol^{-1}) for the isolated X_3^- (X = Cl, Br, and I) anions computed using the CCSD(T)/AWCVTZ method.

Mode	Cl_3^-		Br_3^-		I_3^-	
	ω^a	ω^b	ω^a	ω^b	ω^a	ω^b
ω_1 (asym stretch, σ_u)	253 (623)[c]	254	187 (250)	186	138 (151)	139
ω_2 (sym stretch, σ_g)	264 (0)[c]	261	164 (0)	161	114 (0)	112
ω_3 (bend, π_u)	161 (1)	159	89 (0)	88	57 (0)	57

[a] Harmonic vibrational frequencies in this work.
[b] Harmonic vibrational frequencies reported by Dixon and coworkers (ref. 120).
[c] Vibrational modes for ω_1 and ω_2 switch for Cl_3^-.

Table 4.4: Harmonic vibrational frequencies (cm^{-1}) and infrared intensities (in parentheses, km mol^{-1}) of the chlorides MCl_3 (M = Li, Na, K, Rb, and Cs) molecules predicted using the CCSD(T)/AWCVTZ method.

	$LiCl_3$		$NaCl_3$		KCl_3		$RbCl_3$		$CsCl_3$	
	ω	*expt*[a]	ω	*expt*[a]	ω	*expt*[a]	ω	*expt*[a]	ω	*expt*[a]
$\nu_1(a')$[b]	453(93)	410	414(188)	375	370(242)	345	360(245)	340	354(239)	327
$\nu_2(a')$[b]	576(107)	-	322(41)	276	248(57)	258	222(80)	223	216(89)	225
$\nu_3(a')$[b]	281(84)	-	183(25)	-	190(16)	-	179(10)	-	174(27)	-
$\nu_4(a')$[b]	92(77)	-	117(113)	-	138(158)	-	134(140)	-	127(116)	-
$\nu_5(a')$[b]	124(5)	-	85(8)	-	66(2)	-	52(1)	-	44(1)	-
$\nu_6(a'')$[b]	108(7)	-	123(1)	-	138(1)	-	141(1)	-	143(1)	-

[a] Raman and IR fundamentals reported in the Ault and Andrews argon matrix study (ref. 118).
[b] The $\nu_{1\text{-}6}$ correspond to the modes 1-6 in Figure 4.5, respectively.

In Table 4.3, the harmonic vibrational frequencies of the isolated X_3^- computed in this work agree to within 3 cm^{-1} of those reported by Dixon and coworkers.[120] However, with respect to the experimental MCl_3 frequencies (see Table 4.4) of Ault and Andrews,[118] we only observed reasonable agreement with the 258 cm^{-1} band for KCl_3. In fact, the experimental frequencies of the two prospective MCl_3 bands range from 327 - 410 cm^{-1} and 225 - 276 cm^{-1}, respectively.[118] A similar range is also noticed for our computed MCl_3 frequencies. It is unclear why the two stretch frequencies of Cl_3^- vary so greatly over the range of alkali metal countercations. The extended ranges for the computed MBr_3 and MI_3 frequencies (Table 4.5-4.6) imply a similar ambiguity. This calls into question whether the two observed MX_3 bands truly correspond to the symmetric and antisymmetric stretches of X_3^-. Rather, the bonding in MX_3 establishes alternate normal modes of vibration that include substantial displacement of both the

halide and metal. Therefore, a direct comparison of the frequencies of X_3^- and MX_3 is not straightforward, and explicit inclusion of the alkali metal cation is necessary.

4.4.5 A complex of MX with X_2?

The idea that the alkali metal trihalides might be viewed (that's all, just a suggestion of an alternative perspective) as strongly bound complexes of MX and X_2 came from examining the detailed nature of the fundamental vibrations of these molecules.

As depicted in Figure 4.5, the antisymmetric and symmetric stretches of X_3^- proposed in the previous experimental study[118] of MX_3 are not found among our computed vibrational modes of MX_3. Note that the modes illustrated in Figure 4.5 are similar in all MX_3 (M = Li, Na, K, Rb, Cs and X = Cl, Br, I) molecules. However, for the species with heavy metals (Rb and Cs) which show relatively mild perturbation to X_3^- (judging from its distance asymmetry in Table 4.2), mode 2 (M-X1 stretch) is coupled with the adjacent X1-X2 stretch. Still, no sign of any well-preserved symmetric or antisymmetric stretches of the "free" X_3^- anion can be found from the modes of MX_3.

Figure 4.5 illustrates the vibrational modes for KCl_3. The fundamental vibrations of other MX_3 molecules are remarkably similar, despite the difference in internal asymmetry of the X_3 unit, and distance of M from X_3. There are differences, which may be seen by comparing KCl_3 and MX_3, illustrated in SI. We also found useful a Total Energy Distribution (TED) analysis of the vibrations. which allows one to see the internal coordinates entering a given vibration. These are tabulated in the SI (Table S1). A file allowing animation of all vibrations is available from the authors.

Only modes 1 and 6 involve displacement of the halides alone, whereas modes 2, 3, 4,

and 5 involve significant displacements of the metal as well. Note that mode 1 is almost a pure X-X bond stretch; however, the stretch appears localized to a single X-X bond (X2-X3, B2 in Figure 4.3), unlike the stretches of X_3^- which displace two X-X bonds. This is not unexpected; the equilibrium geometries of the X_3^- unit in MX_3 are unsymmetrical in just this direction. Mode 2 appears to be a localized M-X (M and X1, B3 in Figure 4.3) bond stretch. This localization of two fundamental modes of vibration, conserved across the series studied, suggests that the MX_3 system may be alternatively described as an $MX\text{-}X_2$ complex, rather than a $M^+X_3^-$ ion pair. On this basis, modes 1 and 2 should be distorted X-X and M-X stretches. Specifically, compared to the "free" X_2 and MX frequencies (Table 4.1), the localized X-X and M-X stretch frequencies of the MX_3 species (Tables 4.4-4.6) are mostly found to be lowered, and a consistently decreasing trend may be found moving from Li to Cs.

We note in passing that the optimized bond distances also show a sign of $MX\cdots X_2$ bonding – the X1-X2 distance is always longer than X2-X3, and M-X1 is shorter than M-X2. Agreed, the differences are not large, but the trend is consistent.

While we question the previous description of the MX_3 normal modes, the corresponding frequencies computed here should still align with the experimental vibrational bands. This is because all the modes belong to irreducible representations of the C_s point group, and are thus both IR/Raman-active. So a detailed comparison with matrix isolation experiment is in order.

As shown in Tables 4.3 and 4.4, a direct comparison of the MCl_3 harmonic vibrational frequencies with the experimental values of Ault and Andrews[118] yields generally better agreement than the previous comparison using Cl_3^-, isolated,

noninteracting vibrational modes. To facilitate the assignment of the experimental bands, we notice that only a few modes have the intensity necessary for detection. In addition, the noted IR spectrophotometer limit (200 cm^{-1}) of the experiment[118] precludes the observation of $\nu_4 - \nu_6$ for $LiCl_3$ and $\nu_3 - \nu_6$ for MCl_3 (M = Na, K, Rb, and Cs). Therefore, only ν_1 and ν_2 are candidates for assignment to the experimental IR/Raman bands.

The harmonic vibrational frequencies corresponding to ν_1 and ν_2 of the MCl_3 molecules are relatively close to the experimental values. However, there remain significant discrepancies. Deviations above 40 cm^{-1} from fundamentals are noticed for ν_1 and ν_2 of $LiCl_3$ and $NaCl_3$. The ν_2 harmonic vibrational frequencies for KCl_3, $RbCl_3$, and $CsCl_3$ deviate by 20-27 cm^{-1}, which is more reasonable, but still larger than expected. For the frequencies of this magnitude, we do not expect substantially large enough anharmonic contributions to correct these deviations. A plausible reason for such deviations is that the large red-shift (about 20 – 60 cm^{-1}, see Table S1 in the SI) noted for MX vibrational fundamentals in argon matrices[123] carries over to the MX_3 species. Recall that in Ault and Andrews's experiment,[118] MCl_3 was generated through the reaction of MCl and Cl_2 in an argon matrix at 15 K. As such, the MCl stretch was measured prior to MCl_3 formation. This stretch frequency aligns with the value reported by Jacox (see Table S1 in the SI),[123, 183] confirming a similar argon-induced shift for the Ault and Andrews MCl band. By extension, their reported MCl_3 bands may be significantly shifted as well. Accordingly, assessing the agreement between gas-phase theoretical frequencies and argon matrix experimental frequencies[118] is challenging. Depending on the metal involved, ν_1 and ν_2 can be tentatively assigned to the Cl-Cl and M-Cl stretches, which are probably the actual vibrational bands observed in the Ault and Andrews experiment.[118]

In comparison, there are fewer experimental results for the MBr_3 (Table 4.5) and MI_3 (Table 4.6) species. The 214 cm^{-1} KBr_3 band reported by Ault and Andrews[118] is close to our computed frequency for the localized Br-Br stretch mode (ν_1 = 225 cm^{-1}). Since the largest vibrational frequency of the "free" Br_3^- is predicted to be 187 cm^{-1} (Table 4.3), it is not reasonable to assign this 214 cm^{-1} band to Br_3^- in KBr_3. A good agreement between theory and experiments[121, 122, 131, 184] is achieved for the $CsBr_3$ vibrational frequencies. The ν_1, ν_2, and ν_4 frequencies are computed to be 217, 152, and 96 cm^{-1}, respectively, each of which matches the observed vibrational bands within 10 cm^{-1}. Comparison of the computed frequencies of $CsBr_3$ (Table 4.5) and the "free" Br_3^- (Table 4.3) indicate that the 152 and 96 cm^{-1} experimental bands seemingly match those of Br_3^-, whereas the 217 cm^{-1} band does not.

Table 4.5: Harmonic vibrational frequencies (cm^{-1}) and infrared intensities (in parentheses, km mol^{-1}) of the bromides MBr_3 (M = Li, Na, K, Rb, and Cs) molecules predicted using the CCSD(T)/AWCVTZ method. The KBr_3 and $CsBr_3$ frequencies in italics are from experiments.

	$LiBr_3$	$NaBr_3$	KBr_3	$RbBr_3$	$CsBr_3$
ν_1 (a')[a]	244 (72)	227 (81)	225 (134), *214*[b]	220 (137)	217 (138), *206*[c]/*210*[d]/*213*[e]
ν_2 (a')[a]	475 (88)	258 (67)	183 (23)	155 (32)	152 (40), *140*[c]/*136*[d]/*138*[e]
ν_3 (a')[a]	283 (79)	150 (26)	141 (38)	128 (14)	122 (4)
ν_4 (a')[a]	104 (38)	108 (47)	113 (31)	106 (30)	96 (27), *82*[e]
ν_5 (a')[a]	76 (17)	66 (6)	50 (3)	37 (2)	29 (1)
ν_6 (a'')[a]	77 (6)	79 (1)	82 (0)	83 (0)	84 (0)

[a] The $\nu_{1\text{-}6}$ correspond to the modes 1-6 in Figure 4.5, respectively. [b] Raman and IR frequencies reported in ref. 118. [c] Raman and IR frequencies reported in refs. 121 and 122. [d] IR frequencies reported in ref. 184. [e] Raman frequencies reported in ref. 131.

Table 4.6: Harmonic vibrational frequencies (cm^{-1}) and infrared intensities (in parentheses, km mol^{-1}) of the iodides MI_3 (M = Li, Na, K, Rb, and Cs) molecules predicted using the CCSD(T)/AWCVTZ method. The CsI_3 frequencies in italics are from experiments.

	LiI_3	NaI_3	KI_3	RbI_3	CsI_3
ν_1 (*a'*)[a]	171 (56)	164 (69)	168 (67)	160 (87)	157 (88), *145*[b]/*145*[c]/*149*[d]
ν_2 (*a'*)[a]	417 (79)	222 (37)	149 (40)	118 (12)	110 (17), *101*[b]/*100*[c]/*103*[d]/113[e]
ν_3 (*a'*)[a]	273 (58)	130 (16)	106 (23)	96 (22)	90 (11)
ν_4 (*a'*)[a]	80 (26)	83 (27)	86 (16)	79 (10)	74 (12), *66*[c]/*69*[d]
ν_5 (*a'*)[a]	51 (7)	47 (4)	39 (4)	30 (2)	24 (1)
ν_6 (*a''*)[a]	53 (8)	51 (1)	53 (0)	53 (0)	54 (0)

[a] The $\nu_{1\text{-}6}$ correspond to the modes 1-6 in Figure 4.5, respectively. [b] Raman and IR frequencies reported in refs. 121 and 122. [c] IR frequencies reported in ref. 184. [d] IR frequencies reported in ref. 185. [e] Raman fundamental (in solid argon) reported in ref. 119.

For CsI_3, we find that the three vibrational frequencies from experiments[121, 122, 184, 185] align well with our predicted harmonic values for ν_1, ν_2, and ν_4. It should be noted that each of the three computed frequencies of "free" I_3^- (Table 4.3) are in relatively good agreement with the corresponding experimental values for ν_1, ν_2, and ν_4 of CsI_3 (Table 4.6). This is the only case where X_3^- completely corresponds with MX_3. However, CsI_3 is an extreme case, for which the frequencies (and the geometry) tend to suggest a $Cs^+I_3^-$ ion pair, in spite of its underlying electronic structure (see next section). More generally, the experimental frequencies of $CsBr_3$ and CsI_3 were obtained from the solid state,[121, 122, 131, 184, 185] which might involve alternate electronic structures that make a direct comparison between theory and experiment ambiguous. The seemingly aligned I_3^- and CsI_3 frequencies are outliers. They by no means guarantee overall agreement across all MBr_3 and MI_3 (M = Li, Na, K, Rb, and Cs) species.

To summarize: with limited experimental data, no solid conclusion can be drawn here from the experimentally observed vibrations about whether the MBr_3 and MI_3 should be viewed more as an $M^+X_3^-$ ion pair or the $MX\text{-}X_2$ complex. These concerns notwithstanding, explicit consideration of the metal is instrumental in understanding the vibrational frequencies of the MX_3 species. And an $MX\text{-}X_2$ complex viewpoint of the bonding in the molecule, a perspective that has hitherto not received much attention, is naturally suggested by the vibrational modes. Key factors driving the vibrational frequencies are clearly evinced by an intimate examination of the electronic structure through bonding analyses.

4.4.6 Bonding analyses of MX_3

Bond strength has been described theoretically in the literature by a plethora of bonding indices. Just the fact that there are so many is evidence that bond indices, even as they carefully defined, are to some degree arbitrary. We chose to follow here the insight obtained from a natural bond orbital bond order, as defined by Weinhold and Landis.[186] The natural bond orbital (NBO) results in Table 4.7 show that the bond order of B1 (X1-X2) is consistently lower than that of B2 (X2-X3) for each MX_3 species. No surprise, as this follows the calculated equilibrium distances. A considerable increase of X1-X2 bond order indicates the X1-X2 and X2-X3 become more balanced for KBr_3, $RbBr_3$, $CsBr_3$, KI_3, RbI_3, and CsI_3. For the MCl_3 species, the X2-X3 bond orders are large, approaching those of a single bond. But as the distances in Table 4.2 show, the corresponding bond length remains substantially longer than in Cl_2.

In the NBO formalism, it is possible to assign covalent and ionic character to

bonds.[163-165] The covalency of the X2-X3 bond is also supported by its natural bond order, comprised primarily of covalent contributions (Table 4.7), although an increasing ionic character of the X2-X3 bond can be found on moving from $LiCl_3$ to $CsCl_3$. The preference of covalent over ionic character is switched for KBr_3, $RbBr_3$, $CsBr_3$, KI_3, RbI_3, and CsI_3, in which the X2-X3 bonds possess slightly more ionic features than covalency. This is in accordance with the increased negative charges on atom X3, as shown in Table 4.7.

The calculated charge distribution shows almost complete electron transfer from the metal ion to the trihalide. And in the trihalide, no matter how asymmetric it is, the net charge on the central atom, X1 is close to zero. The electron transferred is distributed, in an asymmetric fashion consistent with the asymmetry of the bonding, among X1 and X3. The pileup of electron density at the termini of a three-center electron-rich system is what one would expect; it is connected, in another context, to the presence of strongly electronegative fluorides at the termini and not the middle of such bonds (e.g. FXeF).

The presence of the metal cation engenders localization of electron density mostly onto X1, as shown by the natural charges in Table 4.7. Orbital interactions based on the NBO perturbation theory analysis (see Methods) shows that the leading interaction between the X1 and X2-X3 units is always the donation of an X1 lone-pair n(X1) into the X2-X3 antibonding orbital σ^*(X2-X3) for all MX_3 species. Thus, strengthened X1-X2 and weakened X2-X3 bonds are expected. The energies for this n(X1) $\rightarrow$ σ^*(X2-X3) interaction (see SI) gradually increase from LiX_3 to CsX_3 (X = Cl, Br, or I). Therefore, the bond orders of X1-X2 and X2-X3 are expected to increase and decrease, respectively. This finding aligns with the trends for the natural bond orders of X1-X2 and X2-X3 given

in Table 4.7. Also, this is in consistent with the decreasing X1-X2 and increasing X2-X3 bond lengths in Table 4.2.

Table 4.7: Natural bond orders and natural charges for MX_3.[a]

	Natural bond order: total (covalent/ionic)				Natural charge			
	X1-X2 (B1)	X2-X3 (B2)	X1-M (B3)	X2-M (B4)	X1	X2	X3	M
Cl_3^-	0.50 (0.25/0.25)	0.50 (0.25/0.25)	-	-	-0.48	-0.03	-0.48	-
$LiCl_3$	0.06 (0.00/0.06)	0.90 (0.82/0.08)	0.50 (0.02/0.48)	0.43 (0.01/0.42)	-0.88	0.00	-0.05	0.93
$NaCl_3$	0.08 (0.01/0.07)	0.86 (0.73/0.13)	0.89 (0.02/0.87)	0.01 (0.00/0.01)	-0.86	0.01	-0.11	0.96
KCl_3	0.13 (0.03/0.10)	0.79 (0.61/0.18)	0.75 (0.01/0.74)	0.06 (0.00/0.06)	-0.81	0.01	-0.18	0.97
$RbCl_3$	0.15 (0.04/0.11)	0.77 (0.57/0.20)	0.72 (0.01/0.71)	0.06 (0.00/0.06)	-0.79	0.01	-0.20	0.98
$CsCl_3$	0.16 (0.04/0.12)	0.75 (0.54/0.21)	0.69 (0.01/0.68)	0.07 (0.00/0.07)	-0.79	0.01	-0.21	0.98
Br_3^-	0.50 (0.25/0.25)	0.50 (0.25/0.25)	-	-	-0.48	-0.03	-0.48	-
$LiBr_3$	0.13 (0.03/0.10)	0.76 (0.62/0.14)	0.47 (0.02/0.45)	0.43 (0.01/0.42)	-0.77	-0.01	-0.14	0.92
$NaBr_3$	0.15 (0.04/0.11)	0.75 (0.56/0.19)	0.74 (0.02/0.72)	0.06 (0.00/0.09)	-0.76	0.00	-0.20	0.96
KBr_3	0.30 (0.11/0.18)	0.56 (0.25/0.31)	0.25 (0.00/0.25)	0.19 (0.00/0.19)	-0.71	0.00	-0.26	0.97
$RbBr_3$	0.31 (0.12/0.19)	0.55 (0.24/0.31)	0.23 (0.00/0.23)	0.20 (0.00/0.20)	-0.70	0.01	-0.28	0.97
$CsBr_3$	0.32 (0.13/0.19)	0.54 (0.23/0.31)	0.23 (0.00/0.23)	0.20 (0.00/0.20)	-0.68	0.01	-0.30	0.98
I_3^-	0.50 (0.25/0.25)	0.50 (0.25/0.25)	-	-	-0.49	-0.03	-0.49	-
LiI_3	0.15 (0.03/0.12)	0.77 (0.60/0.17)	0.53 (0.03/0.50)	0.32 (0.01/0.31)	-0.73	-0.01	-0.16	0.89
NaI_3	0.17 (0.05/0.12)	0.74 (0.54/0.20)	0.58 (0.02/0.56)	0.26 (0.00/0.26)	-0.72	-0.01	-0.21	0.94
KI_3	0.31 (0.12/0.19)	0.55 (0.25/0.30)	0.44 (0.01/0.43)	0.10 (0.00/0.10)	-0.69	0.00	-0.27	0.96
RbI_3	0.32 (0.13/0.19)	0.54 (0.24/0.30)	0.24 (0.00/0.24)	0.21 (0.00/0.24)	-0.68	0.00	-0.29	0.97
CsI_3	0.33 (0.14/0.19)	0.53 (0.23/0.30)	0.24 (0.00/0.24)	0.21 (0.00/0.21)	-0.67	0.00	-0.31	0.97

[a] The CCSD(T)/AWCVTZ geometries are used. See Figure 4.2 for atomic label and bond definition for MX_3.

The general picture that emerges is consistent with the donor-acceptor picture of bonding in the trihalide anions, at one end of a bonding spectrum, at the other end being symmetrical electron-rich bonding.[135-139]

Both B3 (X1-M) and B4 (X2-M) bonds possess some "purely" ionic character, supported by the natural charges and their predominant ionic bond orders reported in Table 4.7. For the MCl_3 series, except for the similar X1-M and X2-M bond orders for $LiCl_3$, the X1-M bond orders for the other species are much higher than the X2-M bond orders, but comparable to the corresponding X2-X3 (B2) covalent bonds. This observation supports a view of MCl_3 as formed from MX and X_2 interacting through weaker X1-X2 and X2-M bonds. For the bromides and iodides, however, a considerably decreased X1-M bond order for KBr_3, $RbBr_3$, $CsBr_3$, KI_3, RbI_3, and CsI_3 can be noticed, coupled to the generally increased X1-X2 and X2-M bond orders. This is another indication that the X_3^- is less impacted by the larger metal atoms than the smaller ones, which also leaves these species standing at a borderline between the MX-X_2 complex and $M^+X_3^-$ ion pair. However, the featured antisymmetric and symmetric stretches of X_3^- are not clearly exhibited in their vibrational modes discussed previously.

To further correlate the NBO results with the vibrational frequencies, the gradually increasing interaction energies (see SI) for the donor-acceptor interaction [n(X1) → σ^*(X2-X3)] from LiX_3 to CsX_3 rationalize the increasingly shifted X-X stretch frequencies (Tables 4.4-4.6) in MX_3, relative to the frequencies of corresponding "free" diatomic X_2 species (Table 4.1). The increasing dative interaction from Li to Cs leads to a greater σ^*(X2-X3) orbital occupation, which weakens the X2-X3 bond (B2) and therefore lowers the X-X stretch frequencies. On the other hand, a comparison of the M-X stretch

frequencies of MX_3 and the "free" MX shows that the X1-M (B3) stretch in MX_3 becomes decreasingly impacted from Li to Cs. The physical origins of this trend seem ambiguous. One possible explanation is that its displacement of the metal in the M-X1 stretch decreases as it becomes heavier, making any perturbation from the X_2 moiety have less impact.

4.4.7 QTAIM

All of the molecules studied feature bond critical points for every short contact. This is shown in Fig. 6 for a typical molecule, KCl_3.

Our results from Bader's quantum theory of atoms-in-molecules (QTAIM) are reported in detail in the SI. Consistent with above NBO results (Table 4.7), the electron density at the bond critical points (BCPs) of B1 (X1-X2) is lower than that of B2 (X2-X3) for each MX_3 species, suggesting a consistently stronger X2-X3 bond than the X1-X2 bond. Similar to the NBO results from LiX_3 to CsX_3, the trends in BCP densities of the X1-X2 bonds (increasing) and X2-X3 bonds (decreasing) indicate that the two bonds become more balanced. In Bader's characterization of atomic interactions,[187] the Laplacian of the electron densities $\nabla^2\rho$(BCP) in Table S2 (in the SI) should provide general bonding features of the MX_3 systems. The consistently smaller $\nabla^2\rho$(BCP) of the bond X2-X3 compared to that of the X1-X2 bond implies that the former possesses more covalency than the later. In addition, the X2-X3 $\nabla^2\rho$(BCP) increases from LiX_3 to CsX_3, suggesting an increasing ionic and decreasing covalent character.

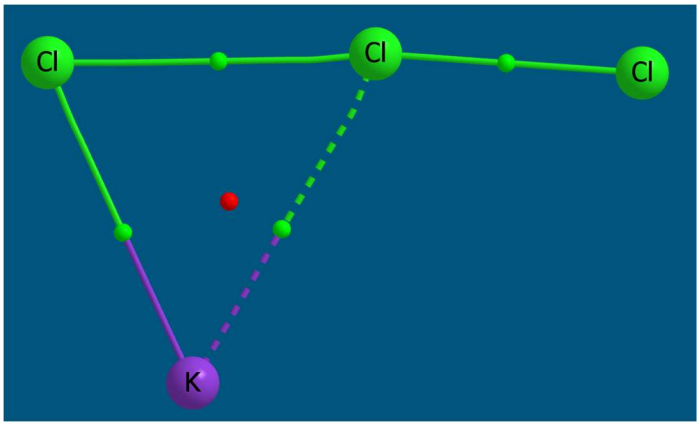

Figure 4.6: Bader analysis for the C_s MX_3 (illustrated for KCl_3), including bond critical points (BCPs, green) and ring critical point (RCP, red). The dashed line for the central KCl bond indicates a CP density below the "weak CP threshold" of 0.025 a.u.

In summary, the bonding trends explored with NBO and QTAIM approaches clearly show that X1-X2 and X2-X3 become more balanced from LiX_3 to CsX_3, although they are never as "truly" balanced as in the "free" $D_{\infty h}$ symmetric X_3^-. We are led to the same conclusion drawn from the structures (Table 4.2) of MX_3: a decreasing effect of the M^+ cation on the X_3^- anions from LiX_3 to CsX_3. A comparison of the bonding types of X_3^- (Scheme 4.1) and MX_3 (Table 4.7) shows that the two equal contributors (bonding types I and II) to the bonding in X_3^- anions collapse into mostly just one of the two for MX_3, mainly depending on the position of the metal cations.

4.4.8 Thermochemistry of MX_3

The reaction energies (D_0, corrected by ZPVE) of three different dissociation pathways:

$$MX_3 \rightarrow MX + X_2 \quad (4.2)$$

$$MX_3 \rightarrow M^+ + X_3^- \quad (4.3)$$

$$MX_3 \rightarrow M + X_3 \quad (4.4)$$

are summarized in Table 4.8. The reason for studying the neutral version of the $MX_3 \rightarrow M^+ + X_3^-$ fragmentation is that ionic fragmentation is naturally more endothermic than neutral ones. In all cases, the dissociation energy for the $MX_3 \rightarrow MX + X_2$ reaction is much lower than that of the $MX_3 \rightarrow M^+ + X_3^-$ (or $MX_3 \rightarrow M + X_3$) dissociation. This result supports our previous conclusion indicating that the MX_3 system is also well-described as an $MX\text{-}X_2$ complex, rather than an $M^+X_3^-$ ion pair.

Table 4.8: Endothermicities (D_0, kcal mol^{-1}) of the three different dissociation processes for MX_3 (M = Li, Na, K, Rb, and Cs; X = Cl, Br, and I) molecules predicted using the B3LYP3/AVTZ method.

Species	D_0 ($MX_3 \rightarrow MX + X_2$)	D_0 ($MX_3 \rightarrow M^+ + X_3^-$)	D_0 ($MX_3 \rightarrow M + X_3$)
$LiCl_3$	10.0	134.8	115.1
$NaCl_3$	11.2	114.1	99.0
KCl_3	12.9	100.3	105.6
$RbCl_3$	13.3	95.8	105.8
$CsCl_3$	13.1	91.6	108.9
$LiBr_3$	14.3	127.6	101.8
$NaBr_3$	15.3	109.1	87.9
KBr_3	17.5	95.7	95.0
$RbBr_3$	17.9	91.3	95.3
$CsBr_3$	18.0	87.3	98.6
LiI_3	15.0	120.7	88.4
NaI_3	15.2	104.0	76.3
KI_3	17.3	90.5	83.2
RbI_3	17.5	86.0	83.4
CsI_3	18.1	82.2	87.0

A note on the numbers in the last two columns: the energetics is a reflection of the differences in the ionization potentials of the metal atoms (falling from 5.5 eV for Li to 3.9 eV for Cs), and the vertical electron affinities of the neutral X_3 species. The latter are remarkably high, 4-5 eV. For the $MX_3 \rightarrow MX + X_2$ dissociation, an increasing trend for D_0 can be noticed from LiX_3 to CsX_3 (X = Cl, Br, or I). This is consistent with the increasing trend for D_0 in the fluoride $MF_3 \rightarrow MF + F_2$ (M = Na, K, Rb, and Cs) series reported by Tozer and Sosa[144]. In addition, previous experiments determined the bond strengths ($X_3^- \rightarrow X_2 + X^-$) of the isolated Cl_3^-, Br_3^-, and I_3^- to be about 24, 30, and 30 kcal mol^{-1} in the gas phase, respectively.[124, 125] Those values are about the twice the D_0 values computed here for the $MX_3 \rightarrow MX + X_2$ dissociations. This is additional evidence that presence of an alkali metal cation weakens the X-X covalent band of X_3^-, favoring localization of more electron density on a terminal X atom. For the $MX_3 \rightarrow M^+ + X_3^-$ dissociation, a decreasing trend in D_0 can be found from LiX_3 to CsX_3 (X = Cl, Br, or I). This indicates that the distortion of X_3^- by M^+ decreases with increasing cation size, caused by the increasing distance between M^+ and X^- as well as the decreasing M-X orbital overlap from LiX_3 to CsX_3. This agrees well with the structural trend for increasingly balanced X1-X2 and X2-X3 bond lengths (Figure 4.3 and Table 4.2) moving from LiX_3 to CsX_3.

4.5 Conclusions

The alkali metal trihalides MX_3 (M = Li, Na, K, Rb, Cs; and X = Cl, Br, I) are systematically studied here using coupled-cluster methods with the weighted core-valence correlation consistent basis sets (new basis sets for K, Rb, and Cs). Benchmarks

comparing the CCSD(T) method against experimental results show satisfactory performance for the new basis sets in predicting reliable structures and harmonic vibrational frequencies for the relevant diatomic species MX and X_2. An isomer search using the B3LYP functional confirms a planar asymmetric T-shaped structure as the global minimum for all MX_3 species.

The CCSD(T) computations suggest a strong distortion of the X_3^- anions by the alkali metal countercations M^+, in the equilibrium geometries, vibrational spectra, bonding, and thermochemistry. For the vibrational modes, the well-established antisymmetric and symmetric stretches of the "free" X_3^- anions are not retained in any MX_3 species. Instead, localized and mutually-perturbed X-X and M-X stretches are involved. For the vibrational frequencies, a comparison of our theoretical MX_3 harmonic vibrational frequencies with the experimental fundamentals yields generally better agreement than the previous comparison using the "free" X_3^- anions. In a bonding analysis, the NBO and QTAIM results show low natural bond orders and electron densities at the bond critical points between MX and X_2, respectively. In the thermochemistry, the $MX_3 \rightarrow MX + X_2$ dissociation pathway has a much smaller endothermicity than the $MX_3 \rightarrow M^+ + X_3^-$ (or $MX_3 \rightarrow M + X_3$) pathway. All above results lead us to suggest that the MX_3 system might alternatively be described as an MX-X_2 complex, rather than the $M^+X_3^-$ ion pair proposed in previous studies.[116-119]

Our conclusions are likely applicable only to the MX_3 systems in the gas phase, in inert matrices (argon and neon), or in non-polar solvents if possible, as no strong solvation would be expected. Strong solvation of M^+ and X_3^- ions in polar solvents (H_2O, for instance) could make the $M^+X_3^-$ ion pair an appropriate description for the MX_3

systems. Such solvation phenomena on the molecular and electronic structure of X_3^- are known as a crucial part of understanding their electrochemistry in electrolytic media,[188, 189] a subject beyond present study.

The two perspectives on MX_3 molecules – strong complexation of trihalide anions by metal cations, and strong interaction of polar MX molecules with dihalogens -- are complementary to each other, each with its own advantages and consequences. We think the chemistry of these remarkable molecules will benefit from keeping both pictures of the bonding in them in view.

CHAPTER 5

Alkali Metal Trifluorides: MF_3[*]

[*]Sun, Z. and Schaefer, H. F., *Phys. Chem. Chem. Phys.* 2018, 20, 18986. Reprinted here with permission of the PCCP Owner Societies.

5.1 Abstract

Many experimental studies have been reported on the alkali metal trifluorides MF_3 (M = Li, Na, K, Rb, and Cs), and several controversies remain. In the present research, we systematically study the MF_3 systems using both coupled-cluster and multireference methods. New predictions and explanations are provided for some known experimental and theoretical challenges, including identification of the true MF_3 minima and global minima, the unclear existence of light alkali metal trifluorides MF_3 (M = Li and Na), and assignment of the F-F-F symmetric stretch frequencies for the heavier alkali metal trifluorides MF_3 (M = K, Rb, and Cs). With several new structures located, we predict a preference of C_s minima for MF_3 (M = Li and Na) and C_{2v} minima for MF_3 (M = K, Rb, and Cs). For the species where multiple minima were located, near degeneracies of those minima can be found in most cases. The endothermicities (~3 - 4 kcal/mol) for the favored $MF_3 \rightarrow MF + F_2$ fragmentations suggest that MF_3 (M = Li and Na) are weakly bonded complexes. The existence of those species at low temperatures cannot be ruled out, and vibrational frequencies are reported to guide future experiments. Most importantly, significant differences between the coupled-cluster and multireference results were found in predicting the F-F-F symmetric stretch frequencies (ν_s) of the C_{2v} MF_3 (M = K, Rb, and Cs) structures, although both methods show good performance in predicting most structures and antisymmetric stretch frequencies (ν_{as}). The coupled-cluster [CCSD(T), CCSDT, and CCSDT(Q)] results agree with the recent experimental assignment of Redeker, Beckers, and Riedel [389 cm^{-1}, *RSC Adv.* **2015**, *5*, 106568] to the ν_s fundamental of CsF_3. In contrast, the multireference (CASPT2, CASPT3, and MRCISD+Q) results support the original experimental assignment of Ault and Andrews

[461 cm^{-1}, *J. Am. Chem. Soc.* **1976**, *98*, 1591; *Inorg. Chem.* **1977**, *16*, 2024]. The F-F-F symmetric stretch frequencies for the MF_3 molecules (M = K, Rb, and Cs) continue to provide a great challenge to theory and experiment.

5.2 Introduction

The trifluoride anion F_3^- is a highly challenging system for theoretical studies. Single-reference methods including DFT,[134, 190-192] MP*n* (*n* = 2, 3, or 4),[134, 142, 191] configuration interaction (CI),[134, 142] and coupled-cluster (CC)[142, 191] produce largely inconsistent results for the structure, binding energy, and vibrational frequencies of F_3^-. Only the CI and CC methods including triple excitations [CCSD(T) and QCISD(T)] exhibit some reliability in achieving agreement with the experiments. Artificial symmetry-breaking issues ($D_{\infty h} \rightarrow C_{\infty v}$) appear in multireference treatments (MCSCF, for instance) with certain active spaces [(3o,4e) and (9o,14e)].[143] Theoretical results are also sensitive to the selection of active space, basis sets, and dynamic correlation.[143, 190]

The challenges associated with F_3^- stem from its special bonding character. In addition to the two main Lewis structure contributors (Types I and II in Figure 5.1), another three-electron bonding type (Type III) contributes significantly to the F_3^- electronic structure, according to the 2004 valence bond (VB) study of Braïda and Hiberty.[137] This special bonding character provides an explanation for its multireference and symmetry-breaking challenges in the theoretical studies mentioned above, as well as the peculiar preference of its energetically unfavorable dissociation channel into $F_2^- + F\bullet$ at high collision energies, instead of $F_2 + F^-$.[133]

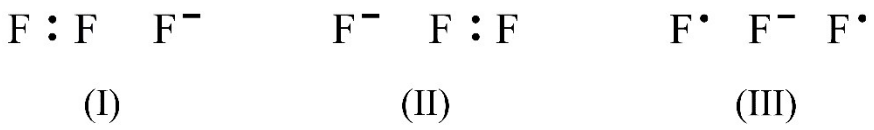

Figure 5.1: Valence-bond structures most often proposed for F_3^-.

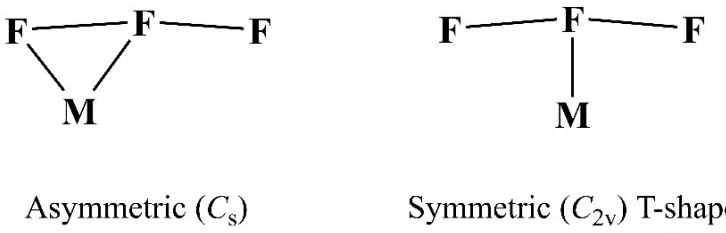

Figure 5.2: Two isomers of MF_3 (M = Li, Na, K, Rb, and Cs) reported in the literature.

Significant challenges remain for theoretical studies of the interactions between F_3^- and the alkali metal cations (M^+, M = Li, Na, K, Rb, and Cs). One major difficulty is to identify the true minima of the MF_3 species. Specifically, inconsistent results were reported in previous attempts to determine which structure [asymmetric (C_s) or symmetric (C_{2v}) T-shape] in Figure 5.2 is the true minimum. The existing theoretical results exhibit strong method-dependence.[144-146, 193] This is very different from the MX_3 case when the halide X is chlorine, bromine, or iodine. The MX_3 structures of the higher halides consistently favor the asymmetric (C_s) structure to be minimum, as suggested by the experiments of Ault and Andrews[118] and our recent theoretical study.[194]

An early systematic study by Tozer and Sosa[144] found that Hartree-Fock, MP2, QCISD, BLYP, and B3LYP give inconsistent results in their predictions of the MF_3

structures. Only the B3LYP functional reasonably predicts the metal-dependent minima (C_s NaF_3; C_{2v} KF_3, RbF_3, and CsF_3, see Figure 5.2) align with the results inferred from the IR/Raman spectra by Ault and Andrews.[147, 148] The C_{2v} minima for KF_3 and CsF_3 were recently (2015) predicted at the CCSD(T)/def2-QZVPP level of theory by Andrews, Riedel and coworkers.[146] The C_s symmetry KF_3 and CsF_3 structures were not reported there because the C_s structures (see Figure 5.2) were selected as the initial geometries for optimization which lead to the C_{2v} minima. In contrast, in the same year (2015), Hoffmann and coworkers located the C_s CsF_3 structure as a minimum with the PBE0/TZVP/ZORA method, whereas the C_{2v} CsF_3 structure was found to be a transition state connecting the two equivalent C_s CsF_3 structures with a small barrier of ~1 kcal/mol.[195] Another paper, published in 2015 by Getmanskii and coworkers, mainly focuses on MF_3 with light alkali metals (M = Li, Na, and K).[145] Apparently Getmanskii disagrees with the B3LYP results from Tozer and Sosa,[144] because both C_s and C_{2v} NaF_3 isomers were predicted by Getmanskii and coworkers to be minima at the CCSD(T)/6-311+G(3df) level of theory, with the C_{2v} NaF_3 structure lying slightly higher (~0.2 kcal/mol, ZPVE corrected).

Another challenge for theoretical studies is to examine the experimental vibrational spectra of the MF_3 systems. The four papers concerning the MF_3 vibrational frequencies in inert matrices by the groups of Andrews, Beckers, Riedel, and coworkers are particularly important.[146-148, 193] According to the early experiments by Andrews and coworkers,[147, 148] only large alkali metals cations (K^+, Rb^+, and Cs^+) can effectively form stable $M^+F_3^-$ "ion pairs" via the reaction $MF + F_2$. Vibrational frequency analyses exhibit two mutually exclusive IR and Raman bands which were proposed to be the

antisymmetric and symmetric stretches of the F_3^- moiety in MF_3, respectively. These vibrational frequencies are remarkably insensitive (different by ~1 cm^{-1}) to the metal identity (K, Rb, and Cs), indicating nearly pure fluorine vibrations not involving the metal very much. The structures of MF_3 (M = K, Rb, and Cs) were therefore proposed to be "T-shaped" with nearly linear and centrosymmetric ($D_{\infty h}$) F_3^- units centered over the M^+ cation (see C_{2v} structure in Figure 5.2).

For the vibrational frequencies, the IR bands (~550 cm^{-1} in argon,[147, 148, 193] krypton,[193] and nitrogen,[193] or ~561 cm^{-1} in neon,[193] metal-insensitive) have been assigned to the antisymmetric stretch (ν_{as}) of the F_3^- unit in MF_3 (M = K, Rb, and Cs), from the experiments of Andrews, Riedel, and coworkers.[146-148, 193] This assignment has been recently supported by the computations of Andrews, Beckers, and coworkers using the CCSD(T) method (def2-TZVPP: 552 cm^{-1}; def2-QZVPP: 568 cm^{-1}, with anharmonic correction).[146] However, the symmetric stretch frequency (ν_s) of F_3^- in CsF_3 is somewhat puzzling. A large deviation [theoretical: 388 cm^{-1} at the CCSD(T)/def2-QZVPP level of theory with anharmonic correction;[146] experimental: 461 cm^{-1} in argon[147, 148]] was found. In the early experiments of Andrews and coworkers,[147, 148] two Raman bands (389 and 461 cm^{-1}) were reported. Upon diffusion (15 K → 40 K → 15 K), the 389 cm^{-1} Raman band decreased in intensity markedly, while the 461 cm^{-1} band remains intense. The former was then assigned to a short-lived unstable species, while the latter was connected to the 550 cm^{-1} IR band which also survives the diffusion procedure. As a result, the 461 and 550 cm^{-1} bands were assigned together to the symmetric and antisymmetric stretches of the F_3^- moiety in CsF_3, respectively.

However, a 2015 paper by Riedel and coworkers[193] provided a different interpretation and suggested that the 389 cm^{-1} band in Andrews's experiment[147, 148] should be assigned to the symmetric stretch ν_s. Therein Riedel's logic is that, except for the 550 cm^{-1} ν_{as} band, a new IR band was located at ~920 cm^{-1} (argon: 923 cm^{-1}; krypton: 919 cm^{-1}) and assigned to a possible combination band of ν_{as} and ν_s ($\nu_{as} + \nu_s = 550 + 389 = 939$ cm^{-1}) in the CsF_3 IR spectra. This new combination band vanished simultaneously with the 550 cm^{-1} ν_{as} band upon irradiation ($\lambda = 266$ nm), suggesting the two might belong to the same species. If this is true, the previously computed ν_s at the 388 cm^{-1} at the CCSD(T)/def2-QZVPP level of theory[146] agrees well with these experiments.[147, 148, 193] However, the sustained and relatively intense 461 cm^{-1} Raman band[147, 148] becomes puzzling if the 389 cm^{-1} is the final answer for the fundamental ν_s.

Last but not least, previous experiments suggest that the $M^+F_3^-$ "ion pair" with the light alkali metals (Li and Na) cannot be effectively produced through the MF + F_2 reaction.[146-148, 193] However, the 2015 theoretical paper by Getmanskii and coworkers located both the C_s and C_{2v} minima (see Figure 5.2) for LiF_3 and NaF_3 at the CCSD(T)/6-311+G(3df) level of theory.[145] The IR studies of the MF + F_2 experiments clearly do not support the formation of LiF_3 and NaF_3 in C_{2v} symmetry, under the stated experimental conditions.[148, 193] However, consistent with the B3LYP results by Tozer and Sosa,[144] the CCSD(T)/6-311+G(3df) results suggest possible C_s minima. This might be theoretical evidence for the $Na^+F^-\cdots F_2$ complex proposed by Ault and Andrews.[148]

In light of the challenges mentioned above, new theoretical research with rigorous computations are called for. The present study systematically investigates the MF_3 (M =

Li, Na, K, Rb, and Cs) molecular systems and makes comparison with previous theoretical and experimental research to help characterize those species.

5.3 Computational Methods

Our initial coupled-cluster[9, 13] [CCSD(T), with restricted (RHF) and unrestricted (UHF) Hartree-Fock references for involved closed-shell and open-shell species, respectively] computations were performed using CFOUR 2.0,[57] with the set of weighted core-valence basis sets noted below:

Li, Na: cc-pwCVTZ[152]

K, Rb, Cs: cc-pwCVTZ-PP[152]

F: aug-cc-pwCVTZ[154]

All electrons are correlated in our CCSD(T) computations except when the Köln/Stuttgart effective core potentials (ECPs, K: ECP10MDF; Rb: ECP28MDF; Cs: ECP46MDF)[157] are used to describe the inner cores of K ($1s^2 2s^2 2p^6$), Rb ($1s^2 2s^2 2p^6 3s^2 3p^6 3d^{10}$), and Cs ($1s^2 2s^2 2p^6 3s^2 3p^6 4s^2 3d^{10} 4p^6 4d^{10}$) elements. To make this discussion succinct, we will refer to the coupled-cluster method with the mixture of these basis sets simply as CCSD(T)/AWCVTZ. For the CCSD(T) computations, stringent criteria were set for the SCF densities (10^{-10}), CC amplitudes (10^{-9}), and RMS forces (10^{-8} Hartree/Bohr). The anharmonic frequencies are obtained using second-order vibrational perturbation theory (VPT2).[20]

As this investigation unfolded, far more sophisticated coupled cluster methods were adopted. Specifically, structures and vibrational frequencies were predicted with the full triples (CCSDT) and perturbative quadruples [CCSDT(Q)] methods.

Multireference (MR) computations were performed using MOLPRO 2010.1,[64, 65] with the CCSD(T)/AWCVTZ-optimized geometries as starting points. A relatively large (16e,10o) active space (including F: 2*p*, Li: 2*s*, Na: 3*s*, K: 4*s*, Rb: 5*s*, and Cs: 6*s*) was first selected for the complete active space self-consistent field (CASSCF) single-point computations. Only the species with leading configuration lower than 90% (all C_{2v} structures, see supporting information, SI) were further treated with multireference configuration interaction method[16, 196] with the Davidson correction,[197] abbreviated as MRCISD+Q. Only the orbitals with occupation number (from CASSCF) in the range of 0.02-1.98 were selected to construct a new active space for the MRCISD+Q optimization and frequency computations. Such an orbital selection strategy generates a consistent active space (4e,3o) and orbital set (one σ bonding, one nonbonding, and one σ* antibonding, Figure 5.3) for all five C_{2v} structures for MF_3 (M = Li, Na, K, Rb, and Cs).

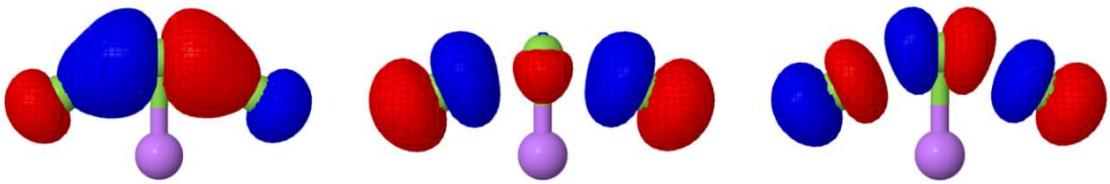

bonding orbital (σ)	nonbonding orbital (n)	antibonding orbital (σ*)
LiF_3: *1.96*	LiF_3: *1.57*	LiF_3: *0.46*
NaF_3: *1.96*	NaF_3: *1.72*	NaF_3: *0.32*
KF_3: *1.96*	KF_3: *1.72*	KF_3: *0.32*
RbF_3: *1.95*	RbF_3: *1.76*	RbF_3: *0.29*
CsF_3: *1.95*	CsF_3: *1.77*	CsF_3: *0.28*

Figure 5.3: Orbitals (illustrated for LiF_3) included in the MRCISD+Q(4e,3o)/AVTZ computations for C_{2v} MF_3 (M = Li, Na, K, Rb, and Cs) with natural orbital occupation numbers (in brackets) obtained at the CASSCF(16e,10o)/AVTZ level of theory.

The MRCISD+Q(4e,3o) computations were performed following the CASSCF(4e,3o) computations. For all MR computations, the SCF energies and densities were both converged to 10^{-10}, and the RMS forces were converged to 10^{-6} Hartree/Bohr. The valence basis sets for the MR computations are listed below.

Li, Na: cc-pVTZ[151]

K, Rb, Cs: cc-pVTZ-PP[152]

F: aug-cc-pVTZ[52]

We will refer to this multireference method with these mixed basis sets as MRCISD+Q(4e,3o)/AVTZ for simplicity. For comparison purposes, additional MR computations were performed using second-order multireference perturbation theory (CASPT2)[198, 199] based on the same active space used for the MRCISD+Q computations, and abbreviated as CASPT2(4e,3o)/AVTZ. The CASPT2 results generally align with the MRCISD+Q results and therefore are only provided in the SI. Moreover, additional coupled-cluster [CCSDT and CCSDT(Q)] and third-order multireference perturbation theory (CASPT3) optimization and frequency were computed for CsF_3, which will be discussed later.

5.4 Results and Discussion

5.4.1 Performance of the selected theoretical methods

The accuracy of the selected coupled-cluster method [CCSD(T)/AWCVTZ] will be assessed first. Relevant diatomic species MF (M = Li, Na, K, Rb, and Cs) and F_2 are chosen as a test set because the experimental information on the tetra-atomic MF_3 species is limited, especially for their structures. Gas phase experimental equilibrium bond

distances and harmonic vibrational frequencies are obtained from the compilation of Huber and Herzberg.[200] The benchmark results are listed in Table 5.1.

For the equilibrium bond lengths, mean absolute errors (MAE) and mean absolute percent errors (MAPE) were computed to be 0.012 Å and 0.6%, respectively. Small positive deviations from the experimental distances can be found for each species, with an increasing trend from LiF to CsF (0.3% to 1.1%). The deviation for F_2 is small, 0.005 Å and 0.4%. For the harmonic vibrational frequencies, the MAPE was computed to be 1.0%. In contrast to the bond lengths, negative deviations from the experimental harmonic vibrational frequencies can be noticed for all diatomics MF, with an increasing trend from LiF to CsF (0.5% to 2.3%). Again, the deviation for F_2 is small, 1 cm^{-1} and 0.1%.

Table 5.1: Benchmark of the CCSD(T)/AWCVTZ equilibrium bond lengths (in Å) and harmonic vibrational frequencies (in cm^{-1}) of MF and F_2 (M = Li, Na, K, Rb, and Cs) molecules, against experimental values compiled by Huber and Herzberg (Ref. 200).

	Equilibrium Bond Lengths				Harmonic Vibrational Frequencies		
Species	Computed	Experiment	Deviation	Percent Error	Computed	Experiment	Percent Error
LiF	1.569	1.564	0.005	0.3%	905	910	0.5%
NaF	1.934	1.926	0.008	0.4%	531	536	0.9%
KF	2.183	2.172	0.011	0.5%	424	428	0.9%
RbF	2.286	2.270	0.016	0.7%	372	376	1.1%
CsF	2.371	2.345	0.026	1.1%	345	353	2.3%
F_2	1.417	1.412	0.005	0.4%	918	917	0.1%
		Mean:	0.012	0.6%		Mean:	1.0%

Table 5.2: Endothermicities (D_0) of two F_3^- dissociation channels at the CCSD(T)/AWCVTZ level of theory.

	Theory (present work)	Experiment (ref. [134])
D_0 ($F_3^- \rightarrow F_2 + F^-$)	22.7 kcal/mol	1.02 ± 0.11 eV (~23.5 kcal/mol)
D_0 ($F_3^- \rightarrow F + F_2^-$)	31.3 kcal/mol	1.30 ± 0.13 eV (~30.0 kcal/mol)

The dissociation energies (D_0) of the two F_3^- dissociation channels are reported in Table 5.2, with the experimental values obtained from the Wenthold collision-induced dissociation experiments for comparison.[134] The D_0 values for the $F_3^- \rightarrow F_2 + F^-$ and $F_3^- \rightarrow F + F_2^-$ dissociation channels are predicted to be 22.7 and 31.3 kcal/mol, respectively. These values deviate from experiment by ~1 kcal/mol.

The initially chosen coupled-cluster method [CCSD(T)/AWCVTZ] predicts reliable structures, harmonic frequencies, and endothermicities for the selected test set. It is then expected to achieve satisfactory accuracy for the MF_3 systems and reasonably assess previous theoretical and experimental research. For those structures with strong multireference issues, MR methods (MRCISD+Q, CASPT2, CASPT3) will be applied and compared with the CCSD(T) results.

5.4.2 Light alkali metal trifluorides: LiF_3 and NaF_3

The results for light alkali metal trifluorides (LiF_3 and NaF_3) at the CCSD(T)/AWCVTZ and MRCISD+Q(4e,3o)/AVTZ levels of theory are shown in Figures 5.4. As discussed in the Introduction, one major challenge for previous theoretical studies of MF_3 is to determine which structure (C_s or C_{2v}) in Figure 5.2 is the true minimum (or global minimum). This will be the focus of the following discussion.

As shown in Figure 5.4, C_s structures are found to be minima for both LiF_3 and NaF_3, while the C_{2v} structures correspond to transition states connecting two equivalent C_s structures. Interestingly, we located two different C_s NaF_3 minima (loose- and tight-type). Like the case of C_s LiF_3, distinct F-F bond distances are noticed in the loose-type C_s NaF_3 corresponding to a NaF-F_2 complex. This has not been reported before, and particularly, it is almost degenerate (see relative energies in Figure 5.4) with the tight-type C_s NaF_3 possessing closely balanced F-F bond distances. The tight-type C_s NaF_3 has been previously reported using B3LYP[144] or CCSD(T)[145] methods. Although the NaF_3 structures are similar to those reported by Getmanskii and coworkers,[145] our CCSD(T)/AWCVTZ results are different from their CCSD(T)/6-311+G(3df) results, predicting both C_s and C_{2v} structures of LiF_3 and NaF_3 to be minima. This substantial inconsistency suggests that coupled-cluster results might be sensitive to the basis sets and/or dynamic correlation (frozen core) strategies selected for this specific system. The present CCSD(T)/AWCVTZ results for NaF_3 agree with Tozer and Sosa's results, which predict the C_s (both loose- and tight-type, Figure 5.4) and C_{2v} NaF_3 to be two minima and a transition state, respectively, with an energy gap being 1 kcal/mol (our value: 0.6 kcal/mol) between the two.[144] Unfortunately, no B3LYP results for LiF_3 were reported in the study by Tozer and Sosa. The splitting between the C_s and C_{2v} LiF_3 structures is 8.3 kcal/mol at the CCSD(T)/AWCVTZ level of theory in the present work. In addition, our attempt to locate a tight-type C_s LiF_3 structure simply leads to the C_{2v} structure.

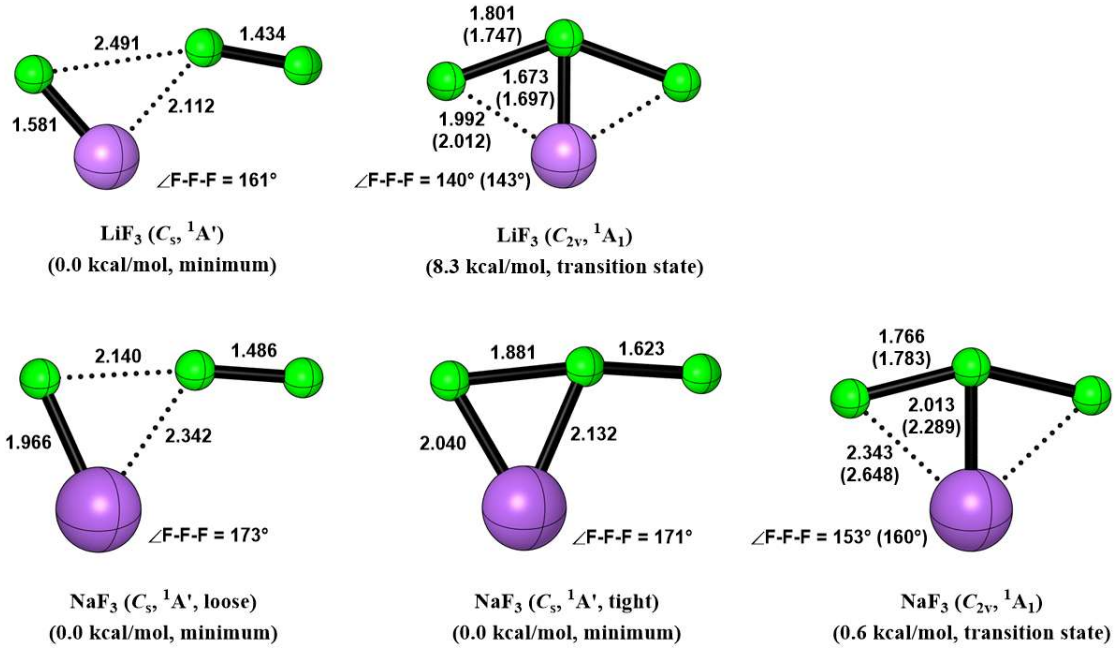

Figure 5.4: Optimized structures and relative energies (ZPVE corrected) of the LiF_3 and NaF_3 stationary points at the CCSD(T)/AWCVTZ and MRCISD+Q(4e,3o)/AVTZ (in parentheses) levels of theory.

Unlike the C_s structures in Figure 5.4, the C_{2v} LiF_3 and NaF_3 are not "well-behaved" electronically with leading configurations falling below 90% (LiF_3: 76% and NaF_3: 83%, see SI for details) at the CASSCF(16e,10o)/AVTZ level of theory. The MRCISD+Q(4e,3o)/AVTZ optimization and frequency computations confirm the transition state nature of the C_{2v} LiF_3 and NaF_3 geometries. Structural changes from the CCSD(T) to the MRCISD+Q method are not significant, as shown in Figure 5.4. The imaginary vibrational frequencies for C_{2v} LiF_3 and NaF_3 are 146*i* and 13*i* (32*i* cm^{-1} using the AWCVQZ basis set) cm^{-1} at the CCSD(T)/AWCVTZ level of theory, respectively. The corresponding MRCISD+Q(4e,3o)/AVTZ imaginary frequencies are 355*i* and 88*i* cm^{-1}, respectively, and the imaginary vibrational modes align with the CCSD(T) results.

Consistent with the IR/Raman experiments by Andrews, Riedel, and coworkers,[146-148, 193] our theoretical results do not support the formation of the symmetric T-shaped (C_{2v}) minima LiF_3 and NaF_3, which are actually transition states shown in Figure 5.4, through the MF + F_2 reactions. That is, no well-defined F_3^- and its characteristic vibrations (ν_{as} and ν_s) can be identified. However, are the three C_s minima in Figure 5.4 stable enough to be detected by experiments? The endothermicities in Table 5.3 show that neutral dissociation of MF_3 into MF and F_2 is apparently favored over the ionic fragmentation ($M^+ + F_3^-$) due to the strong electrostatics between ions. The D_0 values (~3-6 kcal/mol) for $MF_3 \rightarrow MF + F_2$ dissociation suggest that the MF_3 species are weakly bonded complexes. However, this does not entirely rule out their possible existence under low temperature (~15 K) experimental conditions by Andrews, Riedel, and coworkers.[146-148, 193] Unfortunately, no well-characterized LiF_3 (LiF + F_2) experimental vibrational spectra have been reported so far. Our harmonic vibrational frequencies for the C_s LiF_3 complex (Figure 5.4) are thus reported in Table 5.4 as genuine predictions, with the two highest frequencies (882 and 839 cm^{-1}) being perturbed Li-F and F-F bond stretches. The NaF_3 vibrational spectra have been reported by Ault and Andrews.[148] New infrared bands 455 and 460 cm^{-1} (a splitting) after the NaF + F_2 reaction were assigned to a NaF-F_2 complex, in which no F_3^- was formed. This seems to be consistent with our theoretical predictions. The harmonic frequencies 481 (tight-type NaF_3) and 497 (loose-type NaF_3) cm^{-1} in Table 5.4 are possible candidates, both of which correspond to Na-F bond stretches perturbed by the F_2 moiety (experimental harmonic frequency[200] for free NaF: 536 cm^{-1}). Because the two types of C_s NaF_3 structure are nearly degenerate (Figure 5.4), this might be an explanation for the small splitting of the infrared bands (455 and 460 cm^{-1}).[148]

Table 5.3: Endothermicities (D_0, kcal/mol) of the dissociation processes for MF_3 (M = Li, Na, K, Rb, and Cs) minima at the AE-CCSD(T)/AWCVTZ level of theory.

	D_0 ($MF_3 \rightarrow MF + F_2$)	D_0 ($MF_3 \rightarrow M^+ + F_3^-$)
LiF_3 (C_s)	2.7	162.9
NaF_3 (C_s, loose-type)	4.2	134.5
NaF_3 (C_s, tight-type)	4.1	134.5
KF_3 (C_{2v})	5.9	121.4
RbF_3 (C_{2v})	5.9	117.4
CsF_3 (C_{2v})	4.0	113.1
CsF_3 (C_s)	3.8	112.9

Table 5.4: Harmonic vibrational frequencies (cm^{-1}) and infrared intensities (km/mol, in parentheses) for the LiF_3 and NaF_3 minima at the CCSD(T)/AWCVTZ level of theory.

	LiF_3 (C_s)	NaF_3 (C_s, tight-type)	NaF_3 (C_s, loose-type)
ω_1 (a')	882 (136)	481 (329)	617 (246)
ω_2 (a')	839 (13)	424 (101)	497 (54)
ω_3 (a')	224 (78)	350 (19)	238 (17)
ω_4 (a')	126 (7)	268 (327)	118 (170)
ω_5 (a')	70 (80)	78 (14)	56 (49)
ω_6 (a'')	110 (23)	233 (2)	186 (4)

5.4.3 Heavy alkali metal trifluorides: KF_3, RbF_3, and CsF_3

Unlike LiF_3 and NaF_3, the heavier alkali metal trifluorides (KF_3, RbF_3, and CsF_3) "$M^+F_3^-$ ion pairs" can be effectively generated, and their vibrational spectra have been studied in detail,[146-148, 193] as mentioned above. The results for the KF_3, RbF_3, and CsF_3 minima at

the CCSD(T)/AWCVTZ and MRCISD+Q(4e,3o)/AVTZ level of theory are shown in Figure 5.5.

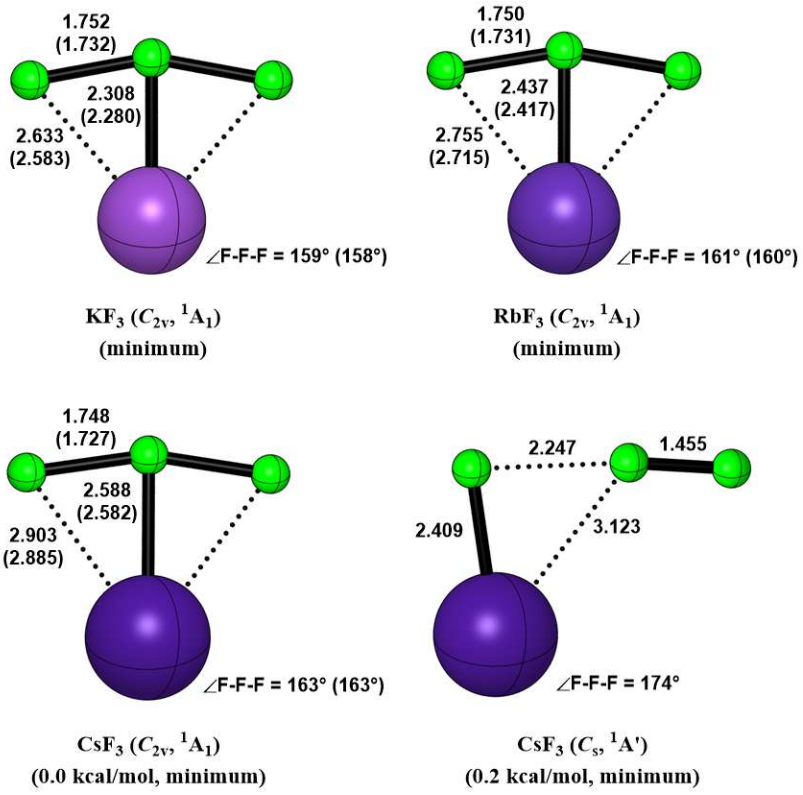

Figure 5.5: Optimized structures and relative energies (ZPVE corrected) of the KF_3, RbF_3, and CsF_3 minima at the CCSD(T)/AWCVTZ and MRCISD+Q(4e,3o)/AVTZ (in parentheses) level of theory.

Consistent with previous experiments and computations,[144-148, 193] the symmetric T-shaped (C_{2v}) KF_3, RbF_3, and CsF_3 minima are located. The F_3^- moiety is slightly bent by ~20 degrees, and the bond distances are close to those reported in earlier studies using CCSD(T) methods.[145, 146] Attempts to locate the C_s structures lead to the C_{2v} structures, consistent with previous computations by Andrews, Riedel, and coworkers.[146] A major

difference, however, is a second C_s minimum (nearly degenerate with the C_{2v} structure, ΔE = 0.2 kcal/mol, Figure 5.5) was found for CsF_3. Similar to the loose-type LiF_3 and NaF_3 (Figure 5.4), this new CsF_3 C_s minimum corresponds to a $CsF\text{-}F_2$ complex with two distinct F-F bond distances (2.247 vs. 1.455 Å, Figure 5.5), but it is different from the C_s CsF_3 minimum located with the PBE0/TZVP/ZORA method by Hoffmann and coworkers.[195] The latter possesses more nearly equal F-F bond distances (1.95 vs. 1.52 Å)[195] than the former. This inconsistency shows a sensitivity to the selected theoretical methods, although no significant multireference issues were found for either C_s CsF_3 structure.

Similar to the C_{2v} symmetry LiF_3 and NaF_3 structures, all heavy alkali metal trifluorides in C_{2v} symmetry are not "well-behaved" electronically. The C_{2v} KF_3, RbF_3, and CsF_3 molecules have leading configurations with weights of 83%, 85%, and 85%, respectively, at the CASSCF(16e,10o)/AVTZ level of theory. The MRCISD+Q(4e,3o)/AVTZ optimizations and frequency computations confirm the minimum nature of the three C_{2v} species. As shown in Figure 5.5, the MRCISD+Q results basically align with the CCSD(T) geometries. Only small decreases in bond distances and angles can be found in going from the CCSD(T) to the MRCISD+Q method.

For the vibrational frequencies, typical F-F-F antisymmetric and symmetric stretch frequencies of free F_3^- and MF_3 (M = K, Rb, and Cs) are reported, together with the available experimental IR/Raman bands for comparison. The CCSD(T) and MRCISD+Q results are reported in Tables 5.5 and 5.6, respectively. For F_3^-, both antisymmetric and symmetric stretch frequencies using CCSD(T)/AWCVTZ are close to the experimental results from Riedel, Andrews, and coworkers.[146, 191, 193]

Table 5.5: Theoretical and experimental vibrational frequencies (cm^{-1}) of F_3^- and MF_3 (M = K, Rb, and Cs) molecules at the CCSD(T)/AWCVTZ level of theory.[a]

	F-F-F antisymmetric stretch (ν_{as})				F-F-F symmetric stretch (ν_s)			
	theory (harm)	theory (anharm)	expt (Ar)	expt (Ne)	theory (harm)	theory (anharm)	expt (Ar)	expt (Kr)
F_3^- ($D_{\infty h}$)	545	520	511[b]	525[b]	399	388	396 ± 5[c]	394 ± 5[c]
KF_3 (C_{2v})	581	562	550[d]	561[e]	405	397	–	–
RbF_3 (C_{2v})	583	569	550[f]	561[c]	398	390	(460/390)[g]	–
CsF_3 (C_{2v})	587	565	550[h]	561[e]	396	384	(461/389)[g]	388 ± 5[c]

[a] Anharmonic vibrational frequencies are obtained from the VPT2 computations. [b] Ref. 146, 191, 193. [c] Ref. 193. [d] Ref. 146-148. [e] Ref. 146, 193. [f] Ref. 147, 148, 193. [g] Both 461 and 390 cm^{-1} Raman bands were observed in Ref. 147, 148. [h] Ref. 146-148, 193.

Table 5.6: Theoretical and experimental vibrational frequencies (cm^{-1}) of F_3^- and MF_3 (M = K, Rb, and Cs) molecules at the MRCISD+Q(4e,3o)/AVTZ level of theory.[a]

	F-F-F antisymmetric stretch (ν_{as})			F-F-F symmetric stretch (ν_s)		
	theory (harm)	expt (Ar)	expt (Ne)	theory (harm)	expt (Ar)	expt (Kr)
F_3^- ($D_{\infty h}$)	528	511[b]	525[b]	417	396 ± 5[c]	394 ± 5[c]
KF_3 (C_{2v})	602	550[d]	561[e]	488	–	–
RbF_3 (C_{2v})	590	550[f]	561[c]	481	(460/390)[g]	–
CsF_3 (C_{2v})	588	550[h]	561[e]	478	(461/389)[g]	388 ± 5[c]

[a] Anharmonic vibrational frequencies are obtained from the VPT2 computations. [b] Ref. 146, 191, 193. [c] Ref. 193. [d] Ref. 146-148. [e] Ref. 146, 193. [f] Ref. 147, 148, 193. [g] Both 461 and 390 cm^{-1} Raman bands were observed in Ref. 147, 148. [h] Ref. 146-148, 193.

For the antisymmetric stretch frequencies (ν_{as}) of MF_3 (M = K, Rb, and Cs), CCSD(T) and MRCISD+Q, the harmonic frequencies basically align with each other, with the MRCISD+Q frequencies (Table 5.6) slightly higher than the former (Table 5.5). After the VPT2 anharmonic corrections, the CCSD(T) fundamental frequencies (ν_{as}) are close to the experimental frequencies obtained in argon and neon matrices. Like the case

of F_3^-, the CCSD(T) fundamental frequencies (ν_{as}) are somewhat closer to the experimental frequencies in neon than to those measured in argon matrices.

For the symmetric stretch frequencies (ν_s) of MF_3 (M = K, Rb, and Cs), however, some substantial differences can be found between CCSD(T) and MRCISD+Q results. The CCSD(T) harmonic frequencies (Table 5.5) are ~400 cm^{-1} and decrease to ~390 cm^{-1} with VPT2 anharmonic corrections. Significantly, the MRCISD+Q harmonic frequencies (~480 cm^{-1}, Table 5.6) are much higher than the CCSD(T) values (by ~80 cm^{-1}) for all three C_{2v} MF_3 (M = K, Rb, and Cs) species. Such large deviations of CCSD(T) from MRCISD+Q might be attributed to the lack of multireference treatment of the former, even though CCSD(T) shows a good performance in predicting the structures and antisymmetric stretch frequencies (ν_{as}). According to previous experiments[147, 148] and present theoretical results (Tables 5.5 and 5.6), RbF_3 and CsF_3 exhibit similar vibrational bands, so we will focus on the discussion of CsF_3 here. The frequencies 461/389 cm^{-1} in Tables 5.5 and 5.6 correspond to the two Raman bands in the Ault and Andrews CsF + F_2 → CsF_3 experiments.[147, 148]

As discussed in the introduction, the 461 cm^{-1} band was suggested to be the true symmetric stretch frequencies (ν_s) because of the disappearance of the 389 cm^{-1} band upon diffusion (15 K → 40 K → 15 K). In contrast, the 2015 paper by Riedel and coworkers[193] assigned the 389 cm^{-1} band as ν_s due to the identification of a possible ν_{as} + ν_s combination band (923 cm^{-1} in argon and 919 cm^{-1} in krypton) and its simultaneous disappearance with the 550 cm^{-1} ν_{as} band upon irradiation (λ = 266 nm). Which one, 461 or 389 cm^{-1}, is the true symmetric F-F-F stretch frequency in the CsF_3 vibrational spectra? Our CCSD(T)/AWCVTZ results for ν_s (harmonic: 396 cm^{-1} & anharmonic: 384

cm^{-1}, Table 5.5) agree well with the 389 cm^{-1} Raman band,[147, 148] consistent with the CCSD(T)/def2-QZVPP value (ν_s = 388 cm^{-1}, anharmonic) in the 2015 paper by Andrews, Riedel, and coworkers.[146] However, our MRCISD+Q(4e,3o)/AVTZ result for ν_s is 478 cm^{-1} (harmonic, Table 5.6). This harmonic frequency is expected to be further lowered and getting close to the 461 cm^{-1} Raman band, if the anharmonic correction can be included. Thus, the MRCISD+Q(4e,3o)/AVTZ result supports the 461 cm^{-1} band as the F-F-F symmetric stretch frequencies, rather than the 389 cm^{-1} band which appears simultaneously with the former in the Ault and Andrews Raman spectra.[147, 148]

To further examine the symmetric stretch frequency (ν_s), several additional coupled-cluster and multireference computations were performed for CsF_3, and the results are listed in Table 5.7. Although with small deviations, all coupled-cluster [CCSD(T), CCSDT, and CCSDT(Q)] results support Riedel's recent assignment (389 cm^{-1})[193] for the ν_s of CsF_3. On the contrary, the multireference (CASPT2, CASPT3, and MRCISD+Q) results predict higher ν_s frequencies which support the original assignment of ν_s (461 cm^{-1}) by Ault and Andrews.[147, 148] In general, the multireference methods tend to predict slightly smaller F-F (but longer Cs-F bond distances) than those from coupled-cluster methods. However, the difference is not substantial. Specifically, the differences in bond distances between CCSDT(Q) and MRCISD+Q(4e,3o) are ~0.03 and ~0.01 Å for the F-F and Cs-F distances, respectively, while the difference in the F-F-F angle is only 1 degree.

Table 5.7: The structures and harmonic F-F-F symmetric stretch frequencies (ω_s, cm^{-1}) of the C_{2v} CsF_3 at higher levels of theory.

Theoretical level[a]	D(F-F)[b]	D(Cs-F)[b]	∠(F-F-F)[c]	ω_s (F-F-F)
CCSD(T)/AVTZ	1.747	2.572	162	398
CCSDT/AVTZ	1.741	2.574	162	415
CCSDT(Q)/AVTZ	1.759	2.573	162	385
CASPT2(4e,3o)/AVTZ	1.746	2.574	162	526
CASPT3(4e,3o)/AVTZ	1.713	2.586	163	515
MRCISD+Q(4e,3o)/AVTZ	1.727	2.581	163	478

[a] Both optimization and frequencies were performed at each level of theory. [b] Distance (D) in Angstroms. [c] Angles (∠) in degrees.

Table 5.8: Vibrational frequencies (cm^{-1}) of the C_{2v} and C_s CsF_3 minima.

	CsF_3 (C_{2v})[a]	description[c]		CsF_3 (C_s)[b]	description[c]
ω_1 (a_1)	478	$\nu_s(F_3)$	ν_1 (a')	748	$\nu(F_2)$
ω_2 (a_1)	347	$\delta(F_3)/\nu(CsF)$	ν_2 (a')	330	$\nu(CsF)$
ω_3 (a_1)	173	$\delta(F_3)$	ν_3 (a')	178	$\delta(F_3)$
ω_4 (b_1)	240	$\gamma(F_3)$	ν_4 (a')	127	$\nu(F_2)$
ω_5 (b_2)	588	$\nu_{as}(F_3)$	ν_5 (a')	44	$\delta(CsF_2)$
ω_6 (b_2)	104	$\rho(F_3)$	ν_6 (a'')	160	$\gamma(F_3)$

[a] MRCISD+Q(4e,3o)/AVTZ harmonic frequencies. [b] CCSD(T)/AWCVTZ harmonic frequencies. [c] *ν*: stretch; *δ*: bend; *ρ*: rock; γ: out-of-plane bend; *as*: antisymmetric; *s*: symmetric.

The combination band (923 cm^{-1} in Ar and 919 cm^{-1} in Kr) has been assigned to the combination of ν_{as} and ν_s (550 + 389 = 939 cm^{-1}) by Riedel and coworkers.[193] However, if the true ν_s of CsF_3 is 461 cm^{-1} (as supported by the multireference computations), what could be the alternative origin of this combination band? The vibrational frequencies of the two CsF_3 minima (C_{2v} and C_s, Figure 5.5) are reported in Table 5.8. It is possible to obtain this combination band from the 588 and 347 cm^{-1} bands (harmonic: 588 + 347 =

935 cm^{-1}) of C_{2v} CsF_3. It might also come from the 748 and 178 cm^{-1} bands (harmonic: 748 + 178 = 926 cm^{-1}) of the newly located C_s CsF_3. The actual frequency should be lower than those values because of anharmonicity. Moreover, due to the near degeneracy (0.2 kcal/mol, Figure 5.5) of the C_{2v} and C_s CsF_3 minima, the simultaneous disappearance of the two different species upon irradiation (λ = 266 nm)[193] could occur. Therefore, treating the simultaneous disappearance of the 550 and 923 cm^{-1} bands as solid evidence to verify the F-F-F symmetric stretch frequency ν_s might need to be reconsidered, because they could come from different species. Those additional possibilities certainly complicate the band assignment, and future studies should revisit this problem.

5.5 Conclusions

The alkali metal trifluorides MF_3 (M = Li, Na, K, Rb, and Cs) are challenging molecular systems for both experimental and theoretical studies. The most important challenges include determination of the genuine MF_3 minima and the global minima, the problematic existence of the light alkali metal trifluorides MF_3 (M = Li and Na), and the assignment of the F-F-F symmetric stretch frequencies for the heavy alkali metal trifluorides MF_3 (M = K, Rb, and Cs).

In the present study, we provide new explanations and solutions to the above problems using very high level coupled-cluster [CCSD(T), CCSDT, and CCSDT(Q)] and multireference (CASPT2, CASPT3, and MRCISD+Q) methods. Benchmarks show good performance of the coupled-cluster method [CCSD(T)/AWCVTZ, see Methods] in predicting reliable structures, harmonic frequencies, and endothermicities for the selected test set. The CASPT2 and MRCISD+Q methods were applied for those structures with

multireference issues (all C_{2v} structures), and the corresponding results mostly align with the CCSD(T) results.

For locating the true MF_3 minima and global minima, the results support a preference of C_s minima for MF_3 (M = Li and Na) and C_{2v} minima for MF_3 (M = K, Rb, and Cs). Comparison with earlier theoretical studies exhibit a strong method-dependence in determining the nature of the species (transition states or minima) and the energy difference between isomers (locating global minima). The CCSD(T) results were found to be sensitive to different basis sets, frozen core options, and dynamic correlation types. For the species where multiple minima were located, the near degeneracies of those minima can be found in most cases, according to the CCSD(T) results.

Concerning the existence of MF_3 (M = Li and Na), the endothermicities (~3-4 kcal/mol) for the favored $MF_3 \rightarrow MF + F_2$ neutral fragmentation suggest that the MF_3 (M = Li and Na) structures are weakly bonded complexes. Their existence at low temperatures cannot be ruled out. Vibrational frequency analysis suggests possible candidates to match the previously assigned NaF_3 IR bands. Because no well-characterized LiF_3 vibrational spectra have been reported so far, its computed vibrational frequencies are a challenge to future experiments.

For the F-F-F symmetric stretch frequencies (ν_s) of MF_3 (M = K, Rb, and Cs), striking differences were found between the CCSD(T) and MRCISD+Q results, even though the former shows a good performance in predicting most structures and antisymmetric stretch frequencies (ν_{as}). The very high coupled-cluster [CCSDT and CCSDT(Q)] results agree with the recent reassignment [389 cm^{-1}, *RSC Adv.* **2015**, *5*, 106568] of ν_s for CsF_3, while the multireference (CASPT2, CASPT3, and MRCISD+Q) results support the original

assignment of ν_s [461 cm^{-1}, *J. Am. Chem. Soc.* **1976**, *98*, 1591; *Inorg. Chem.* **1977**, *16*, 2024]. The F-F-F symmetric stretch frequencies for MF_3 (M = K, Rb, and Cs) continue to be an experimental and theoretical challenge. For the time being, the application of even higher-level theoretical methods will be difficult. New experiments are strongly encouraged.

CONCLUSIONS

This dissertation focuses on the applications of high-level quantum chemistry methods to several small molecular systems containing metal elements. Throughout this research, highly accurate coupled cluster and multireference methods have been employed.

In Chapter 2, we provided an extensive and predictive study of alkaline-earth metallacyclopentadienes and the recently synthesized magnesium complex $MgC_4[Si(CH_3)_3]_2[CH_3]_2$·TMEDA using density functional and coupled-cluster methods. Our results lead to the following conclusions. The ground-state global minimum of the bare MC_4H_4 rings are predicted to possess C_{2v} symmetry. The MC_4H_4 molecules are predicted to be antiaromatic based on the bond length alternation, $NICS(1)_{zz}$ indices, and resonance energies. The distinct viability of these MC_4H_4 compounds is justified by QTAIM, NBO, MO analyses, and ring strain. The VPT2 anharmonic vibrational frequencies are computed for the BeC_4H_4 and MgC_4H_4. Those group IIA metallacyclopentadienes are generally expected to be confirmed by future synthetic work.

In Chapter 3, we reported a high-level theoretical study of the $Al + CO_2 \rightarrow AlO + CO$ reaction. These new theoretical results are compared with the recent crossed-beam experimental studies by Honma and Hirata who have directly challenged the results of earlier theoretical studies of this system. It can be noticed that the previous theoretical prediction of a substantial barrier height for this reaction was incorrect, which is consistent with Honma-Hirata experimental conclusions. However, for the structures of the possible intermediates, we find striking disagreement with their experimental conclusion that the O-C-O moiety is nearly linear.

In Chapter 4, we systematically studied the alkali metal trihalides MX_3 (M = Li, Na,

K, Rb, Cs; and X = Cl, Br, I) system using density functional and coupled-cluster methods. An isomer search using the B3LYP functional confirms a planar asymmetric T-shaped structure as the global minimum for all MX_3 species. The CCSD(T) computations suggest a strong distortion of the X_3^- anions by the alkali metal countercations M^+. Our results suggest that the MX_3 system might be alternatively described as an MX-X_2 complex, rather than the $M^+X_3^-$ ion pair proposed in previous studies. This new conclusion is supported by the equilibrium geometries with a strong distortion of the X_3^- anions by the countercations M^+, vibrational spectra involving localized and mutually-perturbed X-X and M-X stretches, NBO and QTAIM bonding analyses, and thermochemistry of different fragmentation pathways. Such conclusion is likely applicable only to the MX_3 systems in the gas phase, in inert matrices, or in non-polar solvents if possible, as no strong solvation would be expected. The two perspectives on MX_3 molecules, strong complexation of trihalide anions by metal cations, and strong interaction of polar MX molecules with X_2, are complementary to each other, each with its own advantages and consequences. We think the chemistry of these remarkable molecules will benefit from keeping both pictures of the bonding in them in view.

In Chapter 5, we investigated the challenging alkali metal trifluorides MF_3 (M = Li, Na, K, Rb, and Cs) molecular systems using very high level coupled-cluster [CCSD(T), CCSDT, and CCSDT(Q)] and multireference (CASPT2, CASPT3, and MRCISD+Q) methods. The most important challenges include determination of the genuine MF_3 minima and the global minima, the problematic existence of the light alkali metal trifluorides MF_3 (M = Li and Na), and the assignment of the F-F-F symmetric stretch frequencies for the heavy alkali metal trifluorides MF_3 (M = K, Rb, and Cs). For the most

important result, the F-F-F symmetric stretch frequencies (ν_s) of MF_3 (M = K, Rb, and Cs), striking differences were found between the CCSD(T) and MRCISD+Q results. The coupled-cluster [CCSDT and CCSDT(Q)] results agree with the recent reassignment [389 cm^{-1}, *RSC Adv.* **2015**, *5*, 106568] of ν_s for CsF_3, while the multireference (CASPT2, CASPT3, and MRCISD+Q) results support the original assignment of ν_s [461 cm^{-1}, *J. Am. Chem. Soc.* **1976**, *98*, 1591; *Inorg. Chem.* **1977**, *16*, 2024]. The F-F-F symmetric stretch frequencies for MF_3 (M = K, Rb, and Cs) continue to be an experimental and theoretical challenge.

REFERENCES

(1) Schrödinger, E. *Phys. Rev.* **1926**, *28*, 1049-1070.

(2) Born, M.; Oppenheimer, R. *Ann. Phys.* **1927**, *389*, 457-484.

(3) Slater, J. C. *Phys. Rev.* **1928**, *31*, 333-343.

(4) Slater, J. C. *Phys. Rev.* **1929**, *34*, 1293-1322.

(5) Roothaan, C. C. J. *Rev. Mod. Phys.* **1951**, *23*, 69-89.

(6) Roothaan, C. C. J. *Rev. Mod. Phys.* **1960**, *32*, 179-185.

(7) Møller, C.; Plesset, M. S. *Phys. Rev.* **1934**, *46*, 618-622.

(8) Pople, J. A.; Head‐Gordon, M.; Raghavachari, K. *J. Chem. Phys.* **1987**, *87*, 5968-5975.

(9) Crawford, T. D.; Schaefer, H. F., in *Reviews in Computational Chemistry, Vol 14*, edited by K. B. Lipkowitz, and D. B. Boyd (Wiley-VCH, Inc, New York, **2000**), pp. 33-136.

(10) Raghavachari, K.; Trucks, G. W.; Pople, J. A.; Head-Gordon, M. *Chem. Phys. Lett.* **1989**, *157*, 479-483.

(11) Bartlett, R. J.; Watts, J. D.; Kucharski, S. A.; Noga, J. *Chem. Phys. Lett.* **1990**, *165*, 513-522.

(12) Stanton, J. F. *Chem. Phys. Lett.* **1997**, *281*, 130-134.

(13) Shavitt, I.; Bartlett, R. J., *Many-Body Methods in Chemistry and Physics: MBPT and Coupled-Cluster Theory* (Cambridge University Press, Cambridge, UK, **2009**).

(14) Roos, B. O.; Taylor, P. R.; Siegbahn, P. E. M. *Chem. Phys.* **1980**, *48*, 157-173.

(15) Malmqvist, P. A.; Rendell, A.; Roos, B. O. *J. Phys. Chem.* **1990**, *94*, 5477-5482.

(16) Knowles, P. J.; Werner, H.-J. *Chem. Phys. Lett.* **1988**, *145*, 514-522.

(17) Werner, H. J.; Knowles, P. J. *J. Chem. Phys.* **1988**, *89*, 5803-5814.

(18) Hohenberg, P.; Kohn, W. *Phys. Rev.* **1964**, *136*, B864-B871.

(19) Kohn, W.; Sham, L. J. *Phys. Rev.* **1965**, *140*, A1133-A1138.

(20) Nielsen, H. H. *Rev. Mod. Phys.* **1951**, *23*, 90-136.

(21) Strickler, J. R.; Bruck, M. A.; Wigley, D. E. *J. Am. Chem. Soc.* **1990**, *112*, 2814-2816.

(22) Negishi, E.; Takahashi, T. *Acc. Chem. Res.* **1994**, *27*, 124-130.

(23) Fang, H. Y.; Li, G. T.; Mao, G. L.; Xi, Z. F. *Chem. Eur. J* **2004**, *10*, 3444-3450.

(24) Saito, M.; Yoshioka, M. *Coord. Chem. Rev.* **2005**, *249*, 765-780.

(25) Saito, M.; Sakaguchi, M.; Tajima, T.; Ishimura, K.; Nagase, S.; Hada, M. *Science* **2010**, *328*, 339-342.

(26) Steffen, A.; Ward, R. M.; Jones, W. D.; Marder, T. B. *Coord. Chem. Rev.* **2010**, *254*, 1950-1976.

(27) Agou, T.; Wasano, T.; Jin, P.; Nagase, S.; Tokitoh, N. *Angew. Chem. Int. Ed.* **2013**, *52*, 10031-10034.

(28) Armstrong, D. R.; Garden, J. A.; Kennedy, A. R.; Mulvey, R. E.; Robertson, S. D. *Angew. Chem. Int. Ed.* **2013**, *52*, 7190-7193.

(29) Komagawa, S.; Wang, C.; Morokuma, K.; Saito, S.; Uchiyama, M. *J. Am. Chem. Soc.* **2013**, *135*, 14508-14511.

(30) Fang, B.; Hou, G. H.; Zi, G. F.; Fang, D. C.; Walter, M. D. *Dalton Trans.* **2015**, *44*, 7927-7934.

(31) Wakatsuki, Y.; Kuramitsu, T.; Yamazaki, H. *Tetrahedron Lett.* **1974**, *15*, 4549-4552.

(32) Smith, D. P.; Strickler, J. R.; Gray, S. D.; Bruck, M. A.; Holmes, R. S.; Wigley, D. E. *Organometallics* **1992**, *11*, 1275-1288.

(33) Guerin, F.; McConville, D. H.; Vittal, J. J. *Organometallics* **1997**, *16*, 1491-1496.

(34) Xu, L.; Wang, Y.-C.; Wei, J.; Wang, Y.; Wang, Z.; Zhang, W.-X.; Xi, Z. *Chem. Eur. J* **2015**, *21*, 6686-6689.

(35) Xu, L.; Wei, J.; Zhang , W.-X.; Xi, Z. *Chem. Eur. J* **2015**, *21*, 15860-15866.

(36) Fujita, K.; Ohnuma, Y.; Yasuda, H.; Tani, H. *J. Organomet. Chem.* **1976**, *113*, 201-213.

(37) Yasuda, H.; Nakano, Y.; Natsukawa, K.; Tani, H. *Macromolecules* **1978**, *11*, 586-592.

(38) Yasushi, K.; Nobuko, K.; Kunio, M.; Nobutami, K.; Kazushi, M.; Hajime, Y.; Akira, N. *Chem. Lett.* **1982**, *11*, 1277-1280.

(39) Mashima, K.; Sugiyama, H.; Kanehisa, N.; Kai, Y.; Yasuda, H.; Nakamura, A. *J. Am. Chem. Soc.* **1994**, *116*, 6977-6978.

(40) Gardiner, M. G.; Raston, C. L.; Cloke, F. G. N.; Hitchcock, P. B. *Organometallics* **1995**, *14*, 1339-1353.

(41) Mashima, K.; Matsuo, Y.; Fukumoto, H.; Tani, K.; Yasuda, H.; Nakamura, A. *J. Organomet. Chem.* **1997**, *545*, 549-552.

(42) Michel, O.; Kaneko, H.; Tsurugi, H.; Yamamoto, K.; Törnroos, K. W.; Anwander, R.; Mashima, K. *Eur. J. Inorg. Chem.* **2012**, 998-1003.

(43) Sultanov, R. M.; Vasil'ev, V. V.; Dzhemilev, U. M. *Russ. J. Org. Chem.* **2010**, *46*, 355-362.

(44) Bews, J. R.; Glidewell, C. *J. Organomet. Chem.* **1981**, *219*, 279-293.

(45) Jemmis, E. D.; Schleyer, P. v. R. *J. Am. Chem. Soc.* **1982**, *104*, 4781-4788.

(46) Xu, R.; Winget, P.; Clark, T. *Eur. J. Inorg. Chem.* **2008**, 2874-2883.

(47) Mazurek, A.; Dobrowolski, J. C. *J. Org. Chem.* **2012**, *77*, 2608-2618.

(48) Xie, Y.; Schaefer, H. F.; Jemmis, E. D. *Chem. Phys. Lett.* **2005**, *402*, 414-421.

(49) Wei, J. N.; Liu, L.; Zhan, M.; Xu, L.; Zhang, W. X.; Xi, Z. F. *Angew. Chem. Int. Ed.* **2014**, *53*, 5634-5638.

(50) Li, H.; Feng, H.; Sun, W.; Zhang, Y.; Fan, Q.; Peterson, K. A.; Xie, Y.; Schaefer, H. F. *Mol. Phys.* **2013**, *111*, 2292-2298.

(51) Lim, I. S.; Stoll, H.; Schwerdtfeger, P. *J. Chem. Phys.* **2006**, *124*, 034107.

(52) Dunning, T. H. *J. Chem. Phys.* **1989**, *90*, 1007-1023.

(53) Koput, J.; Peterson, K. A. *J. Phys. Chem. A* **2002**, *106*, 9595-9599.

(54) Prascher, B. P.; Woon, D. E.; Peterson, K. A.; Dunning, T. H.; Wilson, A. K. *Theor. Chem. Acc.* **2010**, *128*, 69-82.

(55) Clabo, D. A.; Allen, W. D.; Remington, R. B.; Yamaguchi, Y.; Schaefer, H. F. *Chem. Phys.* **1988**, *123*, 187-239.

(56) Nielsen, H. H. *Phys. Rev.* **1945**, *68*, 181-191.

(57) CFOUR, a quantum chemical program package written by J.F. Stanton, J. Gauss, M.E. Harding, P.G. Szalay with contributions from A.A. Auer, R.J. Bartlett, U. Benedikt, C. Berger, D.E. Bernholdt, Y.J. Bomble, L. Cheng, O. Christiansen, M. Heckert, O. Heun, C. Huber, T.-C. Jagau, D. Jonsson, J. Jusélius, K. Klein, W.J. Lauderdale, D.A. Matthews, T. Metzroth, L.A. Mück, D.P. O'Neill, D.R. Price, E. Prochnow, C. Puzzarini, K. Ruud, F. Schiffmann, W. Schwalbach, C. Simmons, S. Stopkowicz, A. Tajti, J. Vázquez, F. Wang, J.D. Watts and the integral packages MOLECULE (J. Almlöf and

P.R. Taylor), PROPS (P.R. Taylor), ABACUS (T. Helgaker, H.J. Aa. Jensen, P. Jørgensen, and J. Olsen), and ECP routines by A. V. Mitin and C. van Wüllen. For the current version, see http://www.cfour.de.

(58) Lee, C. T.; Yang, W. T.; Parr, R. G. *Phys. Rev. B* **1988**, *37*, 785-789.

(59) Becke, A. D. *J. Chem. Phys.* **1993**, *98*, 5648-5652.

(60) Perdew, J. P. *Phys. Rev. B* **1986**, *33*, 8822-8824.

(61) Becke, A. D. *Phys. Rev. A* **1988**, *38*, 3098-3100.

(62) Zhao, Y.; Truhlar, D. G. *Theor. Chem. Acc.* **2008**, *120*, 215-241.

(63) Neese, F. *WIREs Comput. Mol. Sci.* **2012**, *2*, 73-78.

(64) Werner, H.-J.; Knowles, P. J.; Knizia, G.; Manby, F. R.; Schütz, M. *WIREs Comput. Mol. Sci.* **2012**, *2*, 242-253.

(65) Werner, H.-J.; Knowles, P. J.; Knizia, G.; Manby, F. R.; Schütz, M.; Celani, P.; Györffy, W.; Kats, D.; Korona, T.; Lindh, R. *et al.*, MOLPRO, version 2010.1, a package of *ab initio* programs, **2010**, see http://www.molpro.net.

(66) Fallah-Bagher-Shaidaei, H.; Wannere, C. S.; Corminboeuf, C.; Puchta, R.; Schleyer, P. v. R. *Org. Lett.* **2006**, *8*, 863-866.

(67) Cheeseman, J. R.; Trucks, G. W.; Keith, T. A.; Frisch, M. J. *J. Chem. Phys.* **1996**, *104*, 5497-5509.

(68) Chen, Z. F.; Wannere, C. S.; Corminboeuf, C.; Puchta, R.; Schleyer, P. v. R. *Chem. Rev.* **2005**, *105*, 3842-3888.

(69) Castro, A. C.; Osorio, E.; Jiménez-Halla, J. O. C.; Matito, E.; Tiznado, W.; Merino, G. *J. Chem. Theory Comput.* **2010**, *6*, 2701-2705.

(70) Islas, R.; Poater, J.; Solà, M. *Organometallics* **2014**, *33*, 1762-1773.

(71) T. A. Keith, AIMAll (Version 16.01.09), TK Gristmill Software, Overland Park KS, USA, **2016** (aim.tkgristmill.com).

(72) NBO 6.0. E. D. Glendening, J. K. Badenhoop, A. E. Reed, J. E. Carpenter, J. A. Bohmann, C. M. Morales, C. R. Landis, F. Weinhold, Theoretical Chemistry Institute, University of Wisconsin, Madison (**2013**).

(73) Pauling, L.; Wheland, G. W. *J. Chem. Phys.* **1933**, *1*, 362-374.

(74) Wheland, G. W., *The Theory of Resonance* (Wiley, New York, **1944**).

(75) Wheland, G. W., *Resonance in Organic Chemistry* (Wiley, New York, **1955**).

(76) Mo, Y.; Peyerimhoff, S. D. *J. Chem. Phys.* **1998**, *109*, 1687-1697.

(77) Mo, Y. *J. Chem. Phys.* **2003**, *119*, 1300-1306.

(78) Mo, Y.; Schleyer, P. v. R. *Chem. Eur. J* **2006**, *12*, 2009-2020.

(79) Mo, Y.; Song, L.; Lin, Y. *J. Phys. Chem. A* **2007**, *111*, 8291-8301.

(80) Mulliken, R. S.; Parr, R. G. *J. Chem. Phys.* **1951**, *19*, 1271-1278.

(81) Mo, Y.; Wu, W.; Zhang, Q. *J. Phys. Chem.* **1994**, *98*, 10048-10053.

(82) Kollmar, H. *J. Am. Chem. Soc.* **1979**, *101*, 4832-4840.

(83) Breslow, R.; Mohacsi, E. *J. Am. Chem. Soc.* **1963**, *85*, 431-434.

(84) Dewar, M. J. S.; De Llano, C. *J. Am. Chem. Soc.* **1969**, *91*, 789-795.

(85) Schaad, L. J.; Hess, B. A. *Chem. Rev.* **2001**, *101*, 1465-1476.

(86) Mo, Y. R.; Hiberty, P. C.; Schleyer, P. v. R. *Theor. Chem. Acc.* **2010**, *127*, 27-38.

(87) Hariharan, P. C.; Pople, J. A. *Theor. Chim. Acta* **1973**, *28*, 213-222.

(88) Stevens, W. J.; Krauss, M.; Basch, H.; Jasien, P. G. *Can. J. Chem.* **1992**, *70*, 612-630.

(89) Mo, Y. R.; Bao, P.; Gao, J. L. *Phys. Chem. Chem. Phys.* **2011**, *13*, 6760-6775.

(90) Because the ECP integrals in GAMESS are limited to *s*, *p*, *d*, *f*, and *g* core potentials, the highest angular momentum *h* function in the ECP46MDF pseudopotential for Ba atoms is not supported. Therefore, BLW results for BaC_4H_4 are not reported at the cc-pVTZ level.

(91) Schmidt, M. W.; Baldridge, K. K.; Boatz, J. A.; Elbert, S. T.; Gordon, M. S.; Jensen, J. H.; Koseki, S.; Matsunaga, N.; Nguyen, K. A.; Su, S. *et al. J. Comput. Chem.* **1993**, *14*, 1347-1363.

(92) Balci, M.; McKee, M. L.; Schleyer, P. V. *J. Phys. Chem. A* **2000**, *104*, 1246-1255.

(93) Evangelista, F. A.; Allen, W. D.; Schaefer, H. F. *J. Chem. Phys.* **2007**, *127*, 024102.

(94) Karadakov, P. B. *J. Phys. Chem. A* **2008**, *112*, 7303-7309.

(95) Wheeler, S. E.; Houk, K. N.; Schleyer, P. v. R.; Allen, W. D. *J. Am. Chem. Soc.* **2009**, *131*, 2547-2560.

(96) Raghavendra, B.; Arunan, E. *J. Phys. Chem. A* **2007**, *111*, 9699-9706.

(97) Amezaga, N. J. M.; Pamies, S. C.; Peruchena, N. M.; Sosa, G. L. *J. Phys. Chem. A* **2010**, *114*, 552-562.

(98) Shahi, A.; Arunan, E. *Phys. Chem. Chem. Phys.* **2014**, *16*, 22935-22952.

(99) Honma, K.; Hirata, D. *J. Chem. Phys.* **2017**, *147*, 013903.

(100) Sakai, S. *J. Phys. Chem.* **1992**, *96*, 131-135.

(101) Panek, J.; Latajka, Z. *J. Phys. Chem. A* **1999**, *103*, 6845-6850.

(102) Fontijn, A.; Felder, W. *J. Chem. Phys.* **1977**, *67*, 1561-1569.

(103) Costes, M.; Naulin, C.; Dorthe, G.; Vaucamps, C.; Nouchi, G. *Faraday Discuss. Chem. Soc.* **1987**, *84*, 75-86.

(104) Parnis, J. M.; Mitchell, S. A.; Hackett, P. A. *Chem. Phys. Lett.* **1988**, *151*, 485-488.

(105) Garland, N. L.; Douglass, C. H.; Nelson, H. H. *J. Phys. Chem.* **1992**, *96*, 8390-8394.

(106) Le Quere, A. M.; Xu, C.; Manceron, L. *J. Phys. Chem.* **1991**, *95*, 3031-3037.

(107) Howard, J. A.; Mccague, C.; Sutcliffe, R.; Tse, J. S.; Joly, H. A. *J. Chem. Soc. Faraday Trans.* **1995**, *91*, 799-804.

(108) Brock, L. R.; Duncan, M. A. *J. Phys. Chem.* **1995**, *99*, 16571-16575.

(109) Thomas, B. J.; Harruff-Miller, B. A.; Bunker, C. E.; Lewis, W. K. *J. Chem. Phys.* **2015**, *142*, 174310.

(110) Marshall, P.; Oconnor, P. B.; Chan, W. T.; Kristof, P. V.; Goddard, J. D. *Abstracts of Papers Am. Chem. Soc.* **1991**, *202*, 90.

(111) Selmani, A.; Ouhlal, A. *Chem. Phys. Lett.* **1992**, *191*, 213-218.

(112) Woon, D. E.; Dunning, T. H. *J. Chem. Phys.* **1993**, *98*, 1358-1371.

(113) Dunning, T. H.; Peterson, K. A.; Wilson, A. K. *J. Chem. Phys.* **2001**, *114*, 9244-9253.

(114) Gordon, M. S.; Schmidt, M. W., in *Theory and Applications of Computational Chemistry*, edited by G. Frenking, K. S. Kim, and G. E. Scuseria (Elsevier, Amsterdam, **2005**), pp. 1167-1189.

(115) Chase Jr., M. W. *NIST-JANAF Themochemical Tables, Fourth Edition, J. Phys. Chem. Ref. Data, Monograph 9* **1998**, 1-1951.

(116) Ault, B. S.; Andrews, L. *J. Am. Chem. Soc.* **1975**, *97*, 3824-3826.

(117) Andrews, L. *J. Am. Chem. Soc.* **1976**, *98*, 2147-2152.

(118) Ault, B. S.; Andrews, L. *J. Chem. Phys.* **1976**, *64*, 4853-4859.

(119) Andrews, L.; Prochaska, E. S.; Loewenschuss, A. *Inorg. Chem.* **1980**, *19*, 463-465.

(120) Thanthiriwatte, K. S.; Spruell, J. M.; Dixon, D. A.; Christe, K. O.; Jenkins, H. D. B. *Inorg. Chem.* **2014**, *53*, 8136-8146.

(121) Gabes, W.; Gerding, H. *J. Mol. Struct.* **1972**, *14*, 267-279.

(122) Gabes, W.; Elst, R. *J. Mol. Struct.* **1974**, *21*, 1-5.

(123) Jacox, M. E. *J. Mol. Spectrosc.* **1985**, *113*, 286-301.

(124) Do, K.; Klein, T. P.; Pommerening, C. A.; Sunderlin, L. S. *J. Am. Soc. Mass. Spectrom.* **1997**, *8*, 688-696.

(125) Nizzi, K. E.; Pommerening, C. A.; Sunderlin, L. S. *J. Phys. Chem. A* **1998**, *102*, 7674-7679.

(126) Person, W. B.; Anderson, G. R.; Fordemwalt, J. N.; Stammreich, H.; Forneris, R. *J. Chem. Phys.* **1961**, *35*, 908-914.

(127) Nelson, I. V.; Iwamoto, R. T. *J. Electroanal. Chem. (1959)* **1964**, *7*, 218-221.

(128) Robertson, K. N.; Cameron, T. S.; Knop, O. *Can. J. Chem.* **1996**, *74*, 1572-1591.

(129) Robertson, K. N.; Bakshi, P. K.; Cameron, T. S.; Knop, O. *Z. Anorg. Allg. Chem.* **1997**, *623*, 104-114.

(130) Evans, J. C.; Lo, G. Y. S. *J. Chem. Phys.* **1966**, *44*, 3638-3639

(131) Burns, G. R.; Renner, R. M. *Spectrochim. Acta, Pt. A: Mol. Spectrosc.* **1991**, *47*, 991-999.

(132) Hunt, R. D.; Thompson, C.; Hassanzadeh, P.; Andrews, L. *Inorg. Chem.* **1994**, *33*, 388-391.

(133) Tuinman, A. A.; Gakh, A. A.; Hinde, R. J.; Compton, R. N. *J. Am. Chem. Soc.* **1999**, *121*, 8397-8398.

(134) Artau, A.; Nizzi, K. E.; Hill, B. T.; Sunderlin, L. S.; Wenthold, P. G. *J. Am. Chem. Soc.* **2000**, *122*, 10667-10670.

(135) Landrum, G. A.; Goldberg, N.; Hoffmann, R. *J. Chem. Soc.-Dalton Trans.* **1997**, 3605-3613.

(136) Munzarova, M. L.; Hoffmann, R. *J. Am. Chem. Soc.* **2002**, *124*, 4787-4795.

(137) Braida, B.; Hiberty, P. C. *J. Am. Chem. Soc.* **2004**, *126*, 14890-14898.

(138) Braida, B.; Hiberty, P. C. *J. Phys. Chem. A* **2008**, *112*, 13045-13052.

(139) Ciancaleoni, G.; Arca, M.; Caramori, G. F.; Frenking, G.; Schneider, F. S. S.; Lippolis, V. *Eur. J. Inorg. Chem.* **2016**, *2016*, 3804-3812.

(140) Hach, R. J.; Rundle, R. E. *J. Am. Chem. Soc.* **1951**, *73*, 4321-4324.

(141) Pimentel, G. C. *J. Chem. Phys.* **1951**, *19*, 446-448.

(142) Heard, G. L.; Marsden, C. J.; Scuseria, G. E. *J. Phys. Chem.* **1992**, *96*, 4359-4366.

(143) Mota, F.; Novoa, J. J. *J. Chem. Phys.* **1996**, *105*, 8777-8784.

(144) Tozer, D. J.; Carlos P, S. *Mol. Phys.* **1997**, *90*, 515-524.

(145) Getmanskii, I. V.; Koval, V. V.; Minyaev, R. M.; Minkin, V. I. *Mendeleev Commun.* **2015**, *25*, 417-419.

(146) Vent-Schmidt, T.; Brosi, F.; Metzger, J.; Schlöder, T.; Wang, X.; Andrews, L.; Müller, C.; Beckers, H.; Riedel, S. *Angew. Chem. Int. Ed.* **2015**, *54*, 8279-8283.

(147) Ault, B. S.; Andrews, L. *J. Am. Chem. Soc.* **1976**, *98*, 1591-1593.

(148) Ault, B. S.; Andrews, L. *Inorg. Chem.* **1977**, *16*, 2024-2028.

(149) Vosko, S. H.; Wilk, L.; Nusair, M. *Can. J. Phys.* **1980**, *58*, 1200-1211.

(150) Becke, A. D. *Phys. Rev. A* **1988**, *38*, 3098-3100.

(151) Prascher, B. P.; Woon, D. E.; Peterson, K. A.; Dunning, T. H.; Wilson, A. K. *Theor. Chem. Acc.* **2011**, *128*, 69-82.

(152) Hill, J. G.; Peterson, K. A. *J. Chem. Phys.* **2017**, *147*, 244106.

(153) Peterson, K. A.; Figgen, D.; Goll, E.; Stoll, H.; Dolg, M. *J. Chem. Phys.* **2003**, *119*, 11113-11123.

(154) Peterson, K. A.; Dunning, T. H. *J. Chem. Phys.* **2002**, *117*, 10548-10560.

(155) Peterson, K. A.; Shepler, B. C.; Figgen, D.; Stoll, H. *J. Phys. Chem. A* **2006**, *110*, 13877-13883.

(156) Peterson, K. A.; Yousaf, K. E. *J. Chem. Phys.* **2010**, *133*, 174116.

(157) Lim, I. S.; Schwerdtfeger, P.; Metz, B.; Stoll, H. *J. Chem. Phys.* **2005**, *122*, 104103.

(158) Blaudeau, J. P.; Brozell, S. R.; Matsika, S.; Zhang, Z.; Pitzer, R. M. *Int. J. Quantum Chem* **2000**, *77*, 516-520.

(159) Christiansen, P. A. *J. Chem. Phys.* **2000**, *112*, 10070-10074.

(160) Peterson, K. A. *J. Chem. Phys.* **2003**, *119*, 11099-11112.

(161) Glendening, E. D.; Landis, C. R.; Weinhold, F. *Wiley Interdiscip. Rev. Comput. Mol. Sci.* **2012**, *2*, 1-42.

(162) Matta, C. F.; Boyd, R. J., in *The Quantum Theory of Atoms in Molecules* (Wiley-VCH Verlag GmbH & Co. KGaA, **2007**), pp. 1-34.

(163) Glendening, E. D.; Badenhoop, J. K.; Weinhold, F. *J. Comput. Chem.* **1998**, *19*, 628-646.

(164) Glendening, E. D.; Weinhold, F. *J. Comput. Chem.* **1998**, *19*, 593-609.

(165) Glendening, E. D.; Weinhold, F. *J. Comput. Chem.* **1998**, *19*, 610-627.

(166) Linstrom P. J.; Mallard W. G., Eds., NIST Chemistry WebBook, NIST Standard Reference Database Number 69, National Institute of Standards and Technology, Gaithersburg MD, 20899.

(167) Brückner, R.; Haller, H.; Ellwanger, M.; Riedel, S. *Chem. Eur. J.* **2012**, *18*, 5741-5747.

(168) Pichierri, F. *Chem. Phys. Lett.* **2011**, *515*, 116-121.

(169) Groom, C. R.; Bruno, I. J.; Lightfoot, M. P.; Ward, S. C. *Acta Crystallogr. Sect. B: Struct. Sci.* **2016**, *72*, 171-179.

(170) Svensson, P. H.; Kloo, L. *Chem. Rev.* **2003**, *103*, 1649-1684.

(171) Patel, N. N.; Verma, A. K.; Mishra, A. K.; Sunder, M.; Sharma, S. M. *Phys. Chem. Chem. Phys.* **2017**, *19*, 7996-8007.

(172) Breneman, G. L.; Willett, R. D. *Acta Crystallogr. Sec. B* **1969**, *25*, 1073-1076.

(173) Tebbe, K. F.; Georgy, U. *Acta Crystallogr. Sect. C-Cryst. Struct. Commun.* **1986**, *42*, 1675-1678.

(174) Tasman, H. A. *Acta Crystallogr.* **1955**, *8*, 857-857.

(175) Tasman, H. A.; Boswijk, K. H. *Acta Crystallogr.* **1955**, *8*, 59-60.

(176) Rogachev, A. Y.; Hoffmann, R. *Inorg. Chem.* **2013**, *52*, 7161-7171.

(177) Runsink, J.; Swen-Walstra, S.; Migchelsen, T. *Acta Crystallogr. Sec. B* **1972**, *28*, 1331-1335.

(178) Wei, S.; Wang, J.; Deng, S.; Zhang, S.; Li, Q. *Sci. Rep.* **2015**, *5*, 14393.

(179) Havinga, E. E.; Boswijk, K. H.; Wiebenga, E. H. *Acta Crystallogr.* **1954**, *7*, 487-490.

(180) Toman, K.; Honzl, J.; Jecny, J. *Acta Crystallogr.* **1965**, *18*, 673-677.

(181) Thomas, R.; Moore, F. H. *Acta Crystallogr. Sec. B* **1980**, *36*, 2869-2873.

(182) Zhang, W.; Oganov, A. R.; Goncharov, A. F.; Zhu, Q.; Boulfelfel, S. E.; Lyakhov, A. O.; Stavrou, E.; Somayazulu, M.; Prakapenka, V. B.; Konôpková, Z. *Science* **2013**, *342*, 1502-1505.

(183) Jacox, M. E. *Chem. Soc. Rev.* **2002**, *31*, 108-115.

(184) Vincent, H.; Monteil, Y.; Berthet, M. P. *J. Inorg. Nucl. Chem.* **1980**, *42*, 5-7.

(185) Maki, A. G.; Forneris, R. *Spectrochim. Acta, Pt. A: Mol. Spectrosc.* **1967**, *23*, 867-880.

(186) F. Weinhold and C. R. Landis, Valency and Bonding: A Natural Bond Orbital Donor-Acceptor Perspective (Cambridge University Press, **2005**).

(187) Bader, R. F. W.; Essén, H. *J. Chem. Phys.* **1984**, *80*, 1943-1960.

(188) Eriksson, S. K.; Josefsson, I.; Ottosson, N.; Öhrwall, G.; Björneholm, O.; Siegbahn, H.; Hagfeldt, A.; Odelius, M.; Rensmo, H. *J. Phys. Chem. B* **2014**, *118*, 3164-3174.

(189) Jena, N. K.; Josefsson, I.; Eriksson, S. K.; Hagfeldt, A.; Siegbahn, H.; Björneholm, O.; Rensmo, H.; Odelius, M. *Chem. Eur. J.* **2015**, *21*, 4049-4055.

(190) Malcolm, N. O. J.; McDouall, J. J. W. *J. Phys. Chem.* **1996**, *100*, 10131-10134.

(191) Riedel, S.; Köchner, T.; Wang, X.; Andrews, L. *Inorg. Chem.* **2010**, *49*, 7156-7164.

(192) Gutsev, G. L.; Belay, K. G.; Weatherford, C. A.; Ramachandran, B. R.; Gutsev, L. G.; Jena, P. *J. Phys. Chem. A* **2015**, *119*, 6483-6492.

(193) Redeker, F. A.; Beckers, H.; Riedel, S. *RSC Adv.* **2015**, *5*, 106568-106573.

(194) Sun, Z.; Moore, K. B.; Hill, J. G.; Peterson, K. A.; Schaefer, H. F.; Hoffmann, R. *J. Phys. Chem. B* **2018**, *122*, 3339–3353.

(195) Rogachev, A. Y.; Miao, M. S.; Merino, G.; Hoffmann, R. *Angew. Chem. Int. Ed.* **2015**, *54*, 8275-8278.

(196) Werner, H. J.; Knowles, P. J. *J. Chem. Phys.* **1988**, *89*, 5803-5814.

(197) Langhoff, S. R.; Davidson, E. R. *Int. J. Quantum Chem* **1974**, *8*, 61-72.

(198) Werner, H.-J. *Mol. Phys.* **1996**, *89*, 645-661.

(199) Celani, P.; Werner, H.-J. *J. Chem. Phys.* **2000**, *112*, 5546-5557.

(200) Huber, K. P.; Herzberg, G., *Molecular Spectra and Molecular Structure IV. Constants of Diatomic Molecules* (Van Nostrand Reinhold, New York, **1979**).